DYNAMIC MODELLING OF INTERSTITIAL LASER PHOTOCOAGULATION IN SOFT TISSUES

By

WILLIAM M. WHELAN, B.SC., M.SC.

A Thesis
Submitted to the School of Graduate Studies
in Partial Fulfilment of the Requirements
for the Degree
Doctor of Philosophy

McMaster University

© Copyright by William M. Whelan, September 1996

INTERSTITIAL LASER PHOTOCOAGULATION

DOCTOR OF PHILOSOPHY (1996) McMaster University
(Physics) Hamilton, Ontario

TITLE: Dynamic Modelling of Interstitial Laser Photocoagulation in Soft Tissues.

AUTHOR: William M. Whelan, B.Sc. (University of Prince Edward Island), M.Sc.

(McMaster University)

SUPERVISOR: Douglas R. Wyman, Ph.D., F.C.C.P.M.

NUMBER OF PAGES: xiv, 198

ABSTRACT

Interstitial Laser Photocoagulation (ILP) is a minimally invasive cancer treatment technique whereby optical energy from an implanted optical fiber is used to destroy small, solid tumours. In this work, an optical diffusion approximation and heat transfer equations were used to develop dynamic models of interstitial laser heating. Modifications in the thermophysical and optical properties due to tissue coagulation ($T \geq 60°C$) and vaporization of tissue water ($T \geq 100°C$) were incorporated into the physical description. In addition, the effect of different blood perfusion approximations on temperature distributions for an *in vivo* liver model was explored. The calculational results presented indicate the necessity to include dynamic modifications in the tissue biophysical and blood perfusion properties in future parametric investigations of the potential of ILP in various tissues. A quasi-linear model of tissue charring during single fiber ILP was derived. The increase in optical absorption at the fiber tip due to the browning/charring process was modelled as a linear continuous shift in energy deposition from a point optical source to a point heat source. The tissue charring temperature was estimated by placing experimentally measured charring dimensions on calculated temperature profiles. The potential for combining on-line thermometry with dynamic thermal modelling to reconstruct complete tissue temperature distributions during ILP was also investigated. Features of an on-line temperature reconstruction system have been identified and the physical and technical limitations explored.

ACKNOWLEDGEMENTS

I am sincerely grateful to my supervisor and mentor, Dr. Douglas Wyman, for his support and guidance during my graduate studies at McMaster University. He is an exceptional person and an asset to the University community. Thanks Doug.

Special thanks to my friends and colleagues in the Physics Departments at McMaster University and the Hamilton Regional Cancer Centre. Specifically, I acknowledge Ms. Wendy Malarek, Ms. Donna Laking, Ms. Ruth Alexander, Ms. Karen Dougherty, Mr. John Blenkey and Mr. Alan Hazelhurst for their technical support, and Dr. Mike Patterson, Dr. Tom Farrell, Dr. David Chettle, Dr. Brian Pogue and Dr. Alex Vitkin for their enlightening scientific discussions.

I would also like to acknowledge the financial support from McMaster University and the Ontario Laser and Lightwave Research Centre.

Most importantly, I thank my wife Michelle for her love and support, which gave me strength during the difficult years. Finally, my daughter Hayley deserves a BIG KISS. While writing this dissertation, I was a stay-at-home dad, playing with Hayley by day and typing by night. From age 6 months to 2 years, she accompanied me to colloquia, meetings and international conferences and was a proper little lady. Thanks munchkin!

TABLE OF CONTENTS

Chapter 4. Results

LIST OF FIGURES

TABLES

page

NOMENCLATURE

A	Frequency factor (s^{-1}).
c	Heat capacity of tissue (J/g/°C).
c_b	Volumetric heat capacity of blood (J/cm^3/°C).
c_v	Volumetric heat capacity of tissue (J/cm^3/°C).
D	Optical diffusion coefficient (cm).
ΔE	Reaction activation energy (J/mole).
F	Objective functional (°C^2).
k	Thermal conductivity of tissue (W/cm/°C).
k_{eff}	Effective thermal conductivity of tissue (W/cm/°C).
L_{opt}	Optical diffusion length (cm).
L_{th}	Thermal diffusion length (cm).
m_f	Mass fraction of fat in tissue.
m_p	Mass fraction of protein in tissue.
m_w	Mass fraction of water in tissue.
M	Number of sensors.
N	Number of unknown tissue parameters.
$\mathbf{P}$	Tissue parameter vector.
Q_S	Volumetric heat generation (W/cm^3).
Δr_{err}	Sensor position error (mm).
R	Universal gas constant (J/mole/°K).

$R_{coag}(t)$	Tissue coagulation radius (mm).
$R_{vapor}(t)$	Tissue water vaporization radius (mm).
$R_{th}(t)$	Thermal damage radius (mm).
S	Number of sensor samples.
t	Time (s).
Δt_{rec}	Reconstruction time interval (s).
T_{char}	Tissue charring temperature (°C).
T_{err}	Reconstruction temperature error (°C).
T_{meas}	Measured tissue temperature (°C).
T_{pred}	Predicted tissue temperature (°C).
J	Jacobian matrix.
Z	Number of spatial parameter zones.
ϕ_{point}	Total power from a point optical source (W).
ϕ_{line}	Total power from a line optical source (W).
ϕ	Optical irradiance (W/cm^2).
μ_a	Absorption coefficient (cm^{-1}).
μ_s'	Reduced scattering coefficient (cm^{-1}).
μ_{tr}	Total transport coefficient (cm^{-1}).
μ',β	Optical interaction coefficients (cm^{-1}).
λ	Regularization parameter.
ρ	Density of tissue (g/cm^3).
α	Linear interpolation function.
ω	Weighting function.

CHAPTER 1. Introduction

1.1 Interstitial Laser Heating

Small unresectable tumors can be destroyed thermally using interstitial laser heating. This minimally invasive technique, first described by Bown (1983), involves coupling continuous-wave laser energy to optical fibers implanted in a tumor volume. The distribution of optical energy is governed by the scattering and absorption properties of the tissue. Once absorbed, it is converted into heat which propagates through the tissue as determined by the thermophysical properties and blood perfusion patterns. A schematic depiction of the treatment features is shown in Fig. 1.1 and will be discussed later.

As with most cancer therapy techniques, the goal of interstitial laser heating is to destroy a targeted tumor volume while sparing surrounding normal tissues. Temperatures may be monitored (typically by implanted microthermocouples) or thermal lesions imaged (ultrasound for example) during therapy. The tumor temperature may be raised to a hyperthermic level of ~ 41-45°C (Daikuzono et al. 1988, Castren-Persons et al. 1992) or, more commonly, to above 60°C, the threshold for protein denaturation (Jacques et al. 1992, Dachman et al. 1990, Matsumoto et al. 1992). The latter results in thermal coagulative

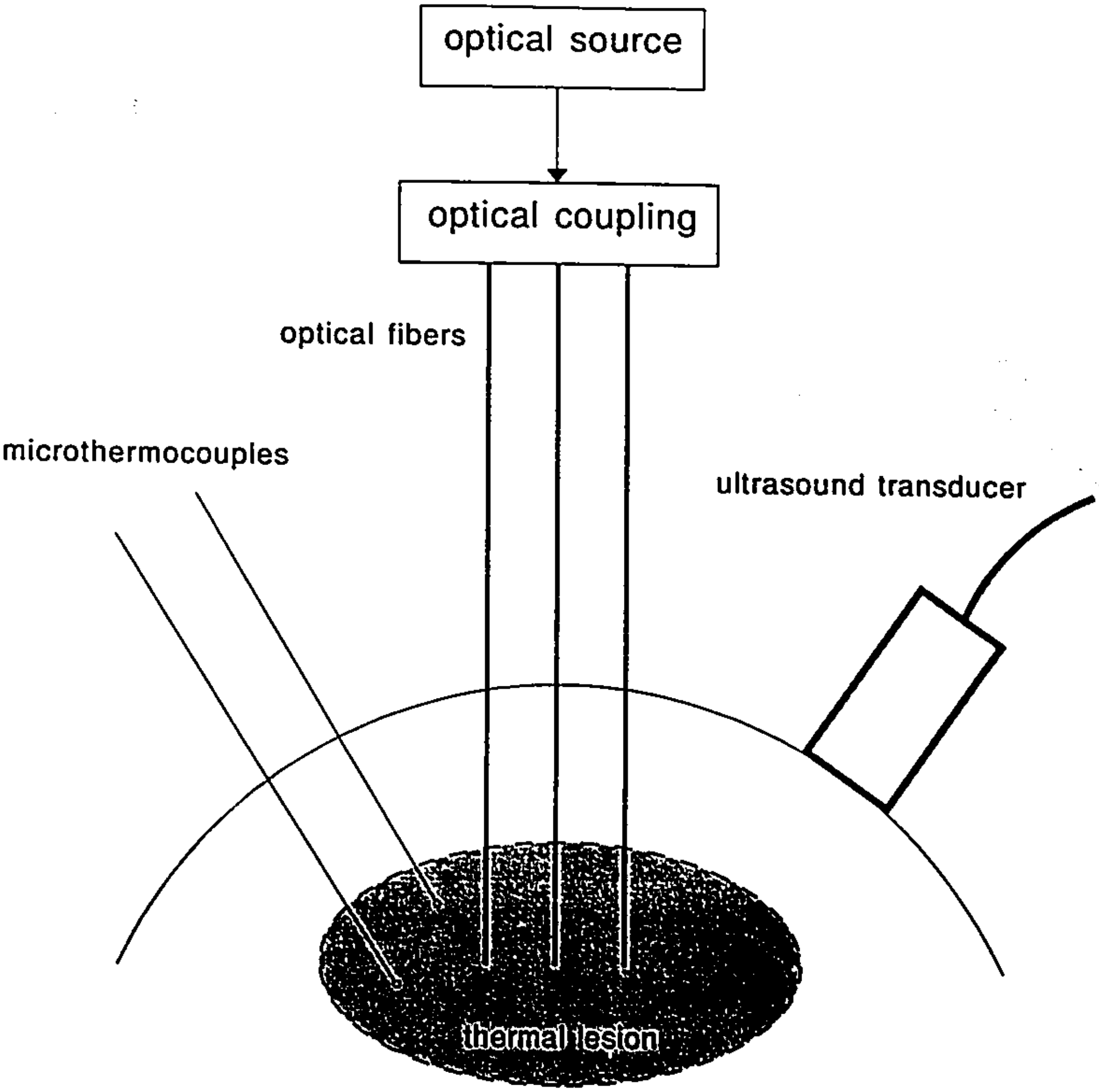

Figure 1.1. Schematic depiction of the treatment features of interstitial laser photocoagulation.

necrosis (Thomsen 1991) and has been become known as interstitial laser photocoagulation (ILP) (Wyman et al. 1992, Amin et al. 1993a).

When plane-cut optical fiber tips are used, ILP is performed typically by delivering from each fiber a power of 1.5-2.5 W for 500-1000 s from a continuous Nd:YAG laser operating at 1064 nm or from laser diodes emitting near 800 nm. After irradiation, the small volume of damaged tissue is absorbed or isolated by the body. Clinically, ILP has been used to destroy small unresectable tumors in brain (Roux et al. 1992), head and neck (Castro et al. 1992, Ohyama et al. 1988), liver (Amin et al. 1993a, Steger et al. 1989, Hahl et al. 1990, Dowlatshahi et al. 1992a) and breast (Harries et al. 1994).

Over the past decade investigation into the potential of ILP has been substantial. Research has proceeded on four major fronts: 1) understanding the pathologic effect of laser-tissue thermal interactions, 2) correlation between irradiation parameters and induced lesion dimensions in various mammalian tissues, 3) development of physical and thermal models for dosimetry and 4) development of on-line temperature and image monitoring systems. These will be discussed in order.

1.2 Photothermal Injury

Photobiological effects of laser-tissue interactions are divided into three mechanistic categories: photomechanical, photochemical and photothermal (Boulnois 1986). During fast-pulsed laser irradiation, production of plasma generates a shockwave which disrupt cells, a photomechanical effect. During photodynamic therapy (PDT), production of toxic reactive species from light initiated chemical reactions is a photochemical effect. During interstitial laser heating, the conversion of optical energy to heat produces photothermal effects.

The investigation into the cellular, subcellular and physiological mechanisms by which heat elicits a biological response is an area of active research. The extent of the thermal injury has been shown to depend on the temperature-time history as specified by the Arrhenius damage integral and quantified by thermal rate kinetics (Henriques 1947, Birngruber 1979, McKenzie 1990). A detailed discussion follows in section 2.3. A cross section of a typical thermal lesion is shown in Fig. 1.2. The lesion is characterized by a central area of charred tissue (zone 1) surrounded by zones of desiccated tissue (zone 2) and coagulated tissue (zone 3) extending from the optical fiber (center of lesion). Beyond the coagulation region there is an area of lesser temperature thermal injury (zone 4).

In zone 4 tissue temperatures are in the 43°C to approximately 60°C range where thermal injury may or may not be visible to the naked eye immediately after irradiation depending on the tissue type, but is observed a few hours later as tissue edema brought about by damage to the vascular and cellular membranes (Thomsen 1991). In liver, zone 4 is hemorrhage, which is clearly visible immediately (Malone et al. 1994b). At temperatures greater than approximately 60°C (zone 3) the thermal injury is due to denaturation of proteins and possible

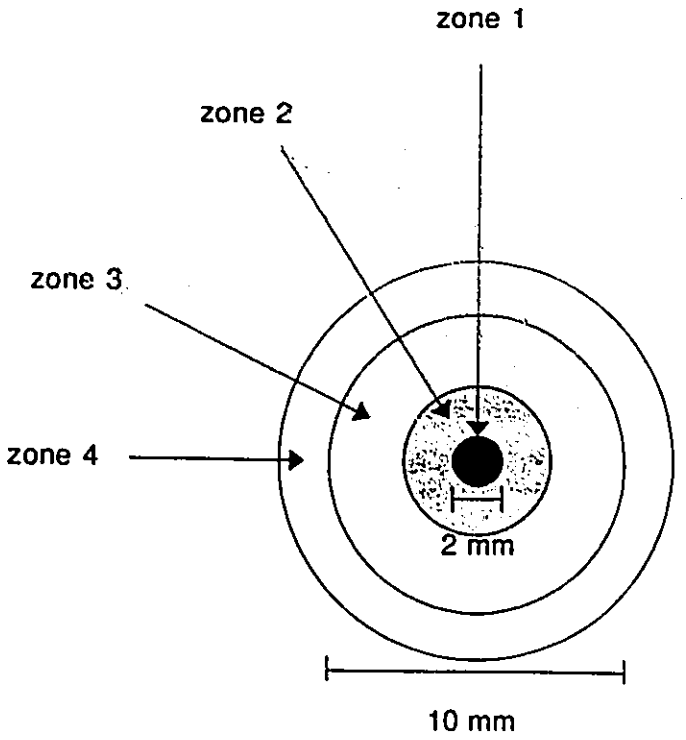

Figure 1.2. Diagrammatic representation of a typical thermal lesion in cross-section, perpendicular to the fiber axis.

membrane rupture and is observed immediately as coagulation or "whitening" of the tissue. Observed histopathological changes include cell shrinkage, hyperchromasia, partial or complete loss of birefringence in muscle and collagen (Thomsen 1991) and cells with pyknotic nuclei (Judy et al. 1993).

Wyman et al. (1994) observed that a coagulation lesion continues to grow long after thermal equilibrium has been established, indicating that some coagulative necrosis is not immediate but determined by temperature-time history. Therefore the temperature at the boundary between zones 3 and 4 may be substantially less than 60°C for protracted exposures. Using thermal kinetic constants for basal epidermis of porcine skin from Henriques (1947), McKenzie (1990) determined that, for a constant temperature exposure, increasing the exposure duration from 100 s to 1000 s decreased the threshold temperature for coagulative necrosis by 5°C. This suggests that the temperature required to produce coagulative necrosis depends only weakly on time.

At temperatures above 100°C (zone 2), cell water vaporizes and the tissue appears desiccated. Histopathological examination reveals that this region has a sponge-like appearance (vacuolation) due to the formation of steam (Mihashi et al. 1976, van Hillegersberg et al. 1994). It is generally accepted that carmelization and carbonization (production of opaque char) (zone 1) follows quickly after vaporization and is concomitant with smoke production (includes CO and CO_2) (Thomsen 1991). However, exact temperatures of onset of carmelization and carbonization are still unclear. It has been suggested that they are intermediates in thermal ablation, occurring at temperatures greater than 100°C (McKenzie 1986) or between 300°C and 1000°C (Thomsen 1991). Histopathological examination reveals that, when the center of the thermal lesion is a vaporized core, charring and/or carmelization typically are found at the periphery of the core (Judy et al. 1993).

1.3 Controlling the Extent of Photothermal Injury

1.3.1 Practical Considerations

Confining the lethal thermal effects to a tumor volume requires spatiotemporal control of the therapeutic temperature elevation. The tumor temperature distribution and resulting thermal lesion depend on irradiation and biophysical parameters. The former include wavelength (typically 800 nm - 1320 nm), delivered power (typically, 1.0 W - 2.5 W of continuous-wave optical energy), optical fiber tip construction (plane-cut, spherical diffuser, cylindrical diffuser) and geometry (single fiber, multiple fiber), and exposure duration (typically 500 s - 1000 s).

When destroying tumors using ILP, the target is generally much larger than the penetration of optical energy, so that optimal lesion formation relies on thermal conduction. This contrasts, for example, with the treatment of portwine stains where the target is a microvessel in the skin. In that case, pulsed optical energy is required with pulse durations sufficiently short (0.3 μs) so that negligible thermal conduction takes place during irradiation (Parrish et al. 1983).

Investigations into the potential of ILP often aim to optimize the irradiation parameters, given the tissue's known and/or estimated biophysical parameters, namely the thermophysical and optical properties, and blood perfusion patterns, in order to obtain the desired thermal lesion. The problem is made difficult due to insufficient data on blood perfusion patterns and *in vivo* optical properties of tumors.

1.3.2 Optimization of Irradiation Parameters

Optimization of the irradiation parameters has been assessed in various *ex vivo* and *in vivo* animal models (Wyman et al. 1994, van Hillegersberg et al. 1994, Amin et al. 1993b, Judy et al. 1993). These studies are predominantly parametric investigations into the dependence of coagulation lesion dimensions on the irradiation parameters, with no emphasis placed on temperatures. A review of ILP at 1064 nm in mammalian tissues by van Hillegersberg et al. (1994) demonstrates that coagulation lesion dimensions are strongly dependent on the choice of irradiation parameters. Generally, for a given tissue type and wavelength, lesion size increases with increasing power and exposure duration. It has been suggested that to be clinically useful, an ILP technique must be able to create thermal lesions at least 8 mm in diameter (Wyman et al. 1994).

The optimal wavelength for ILP has attracted much attention recently. The Nd:YAG laser operating at 1064 nm has generally been preferred for ILP because of the maximal penetration of optical energy at near infrared wavelengths

(Svaasand 1989). It was assumed that maximizing the optical penetration would maximize volumes of coagulative necrosis.

However, Wyman et al. (1992) reported that point optical sources produce smaller thermal lesions than point heat sources of the same power, suggesting that maximal optical penetration may not be advantageous. In fact, less penetrating wavelengths, such as those near 800 nm produced by laser diodes (Amin et al. 1993b, Jacques et al. 1992) make larger thermal lesions than 1064 nm because they invariably produce charring at the fiber tip. The formation of opaque char effectively transforms the point optical source into a point heat source for the remainder of the exposure. Wyman and Whelan (1994) later established a theoretical basis for ILP which showed that a thermal diffusion temperature profile (point heat source) is flattened and reduced when optical diffusion is added.

Charring appears to have the advantage of producing larger lesions but at the expense of smoke production. Intravascular gas microbubbles have been observed under ultrasound imaging during hepatic ILP (Malone et al. 1994a). Although the significance of intravascular gas production remains unclear, it is generally accepted that it should be avoided, because of the potential for air emboli in the circulatory system. Attempts to minimize the potential for charring have been made by air cooling the bare fiber (Dowlatshahi et al. 1992b) and by utilizing spherical or cylindrical diffusing fiber tips (van Hillegersberg et al. 1994, Bettag et al. 1991) which reduce optical power densities. Cooling the tissue surface using fluid irrigation has also been shown to prevent or delay tissue charring (Anvari et al. 1994a).

If multiple fibers are positioned such that the thermal lesions produced by each fiber overlap, substantially larger volumes of tissue can be destroyed than with a single fiber (Davies et al. 1989, Steger et al. 1992, Wyman 1993). Steger et al. (1988) coupled 1.5 W of 1064 nm optical energy to each of four fibers placed at the corners of a square (15 mm side) in normal canine liver. A 500 s exposure induced a 35 mm by 30 mm coagulation lesion in cross-section. For single, bare-tip fiber irradiations, maximum coagulation lesions in liver are approximately 15 mm in diameter. Distributing optical power to multiple fibers may also reduced the potential for charring.

1.3.3 Thermal Modelling

Thermal and physical models of heat transfer have been developed to investigate the potential of interstitial laser heating in various soft tissues (Davies et al. 1989, Dowden et al. 1987, Svaasand et al. 1985, Anvari et al. 1994b). The prediction of steady-state temperature distributions may be sufficient in some instances, but not in others. Temperatures have been used as an index for tissue damage based upon thermal rate kinetics (Prapavat et al. 1996, Beacco et al. 1994, Davies et al. 1989).

By performing pretreatment calculations ("treatment planning"), the clinician can test a variety of irradiation parameters in an attempt to optimize the protocol. Accurate prediction of the complete temperature field requires an accurate description of the optical and thermal processes involved, characterized principally by the thermophysical and optical properties, and blood flow patterns of the tissue.

The thermophysical properties of various normal and diseased mammalian tissues are not well known *in vivo*. Comprehensive compilations of the thermophysical properties of *ex vivo* tissues have been published by Bowman et al. (1975) and Duck (1990). The optical properties of mammalian tissues *ex vivo* have been measured and are published in a review by Cheong et al. (1990). However, the optical properties of *in vivo* tissues are not well determined. Blood perfusion in tissues is highly variable and can range over an order of magnitude within a tumor volume (Feldmann et al. 1992), making *a priori* prediction of the thermal field difficult. Modelling the detailed vasculature has thus far proved mathematically intractable. However, approximating blood flow as a non-directional heat sink (Pennes 1948) or as an enhanced tissue conductivity (Weinbaum and Jiji, 1985) have proven more amenable to solution.

During ILP the exact onset of coagulation is difficult to predict and coagulation has been shown to cause significant increases in optical scattering (Derbyshire et al. 1990, Pickering et al. 1994, Rastegar et al. 1992). Accurate models of light distribution in tissues would include optical property changes during heating, but most current models of ILP do not. The onset of vaporization and resulting decrease in thermal conductivity is also difficult to predict and quantify. The effect of these phase changes on temperature distributions is not well determined. Therefore the full potential of *a priori* prediction of the induced thermal field has yet to be realized.

Recently, there has been interest in quantifying the temperatures required to induce certain histologic changes in tissue so that these changes could be used to indicate the tissue temperature reached (Thomsen 1991). Such histologic temperature markers would prove useful in evaluating mathematical models of ILP.

1.3.4 On-Line Temperature Monitoring

On-line temperature monitoring (thermometry) provides a direct means of controlling temperature elevations in tissue. Temperature-based control systems generally rely on measured temperatures at a few locations using temperature sensors, usually microthermocouples, implanted percutaneously. The number of implant sites, typically 2 to 5, is limited by patient discomfort and tumor location. Strategically placed sensors can, in principle, provide both minimum tumor temperatures and temperatures at nearby critical structures. However, the majority of the tissue temperature is unknown, making it difficult to assess the efficacy of the treatment. Maximizing temperature information while minimizing invasiveness can be achieved using linear sensor arrays comprised of 5 to 10 microthermocouples (Gerig et al. 1992, Anhalt and Hynynen 1992).

Theoretical bases for controlling minimum or maximum tumor temperatures have been developed using temperature feedback to adjust power deposition patterns (Doss 1985, Babbs et al. 1990). Wyman et al. (1991) developed an adaptive control method, using multiple fiber/sensor arrangements. The first computer controlled temperature feedback system was designed by Daikuzono et al. (1988), in which a single probe coupled to an Nd:YAG laser and a single thermocouple were placed in contact with the skin surface.

During ILP, temperature measurements from implanted microthermocouples generally contain errors arising from thermal conduction smearing (Samulski et al. 1985), averaging over the finite sensor volume, and uncertainty in sensor location (typically ± 1 mm). Near the source, large temperature gradients (typically 100-500°C/mm) potentiate all 3 types of error. Temperature measurements can thus be highly inaccurate.

With the growing potential of magnetic resonance imaging (MRI), it was realized that some of the physical variables accessible to MRI are sensitive to temperature changes. This noninvasive form of *in vivo* thermometry exploits the temperature sensitivity of the T1 relaxation time (Parker 1984, Dickinson et al. 1986) or the molecular diffusion coefficient (LeBihan et al. 1989, Clegg et al. 1995) The former parameter exhibits minimal temperature sensitivity and large sensitivity to artifacts related to field inhomogeneities (Delannoy et al. 1990) thereby limiting its potential. The latter parameter exhibits greater temperature sensitivity and is virtually insensitive to field inhomogeneities. However, diffusion weighted imaging requires very fast acquisition and cannot be performed in tissues with a short T2, such as liver, since signal intensity is too low to identify temperature induced signal changes (Gewiese et al. 1994).

1.3.5 On-Line Lesion Imaging

Due to the problems with temperature measurement described above, there has been strong interest in image-based control systems, which bypass temperature measurement. These *in vivo* control systems monitor the growing extent of coagulative necrosis using on-line radiological imaging modalities such as ultrasound in liver (Amin et al. 1993c, Malone et al. 1994b) and MRI in brain (Tracz et al. 1992, El-Ouahabi et al. 1993).

Ultrasound images of thermal lesions appear to rely on the difference in acoustic impedance between surrounding normal tissue and gas (presumably microbubbles) produced during charring (Malone et al. 1994a). Therefore, images are generated reliably only in cases when charring is observed on the fiber tip post-illumination (Malone et al. 1994b, Lofberg et al. 1994). It has been observed during ILP in porcine liver that the necrosis diameter measured with ultrasound is a slight overestimation of the true diameter from histopathology (Malone et al. 1994b). Preliminary results indicate that ultrasound monitoring may be a useful tool for monitoring hepatic ILP.

Magnetic resonance images generally rely on temperature induced contrast between coagulated and viable tissues. T1-weighted dual-echo images of rat brain (El-Ouahabi et al. 1993) and T2-weighted spin-echo images of cat brain (Tracz et al. 1992) during ILP exhibit signal loss around the fiber tip corresponding approximately to regions of coagulative necrosis. The signal loss is likely a result of vaporization and altered mobility of tissue water. Acquisition times for spin-echo techniques are long (5-20 minutes) which enhances the potential for motion artifacts when imaging moving organs. Faster techniques such as rapid acquisition with relaxation enhancement (RARE) (Matsumoto et al. 1992) and T1-weighted turbo fast low-angle shot (FLASH) (~ 5 s) (Gewiese et al. 1994) sequences are currently being evaluated for on-line monitoring of ILP.

1.3.6 Temperature Reconstruction by Parameter Estimation

The discrete nature of on-line thermometry makes it difficult to determine accurately the temperature distribution in the entire target volume. Because of this difficulty, numerical techniques have been applied to infer complete temperature distributions from a set of measured temperatures.

The heated tissue system is represented by a bioheat transfer model. Typically, measured temperatures are used to direct an iterative parameter estimation algorithm that varies one or more unknown biophysical parameters until measured and model-predicted temperatures at sensor locations agree. Tissue inhomogeneity can be modelled by dividing the tissue spatially into zones. This parameter estimation is an inverse problem which is inherently ill-conditioned given, the limited spatial temperature information available (see section 1.3.4).

The potential for combining thermometry with thermal modelling was investigated for simulated hyperthermia treatments by estimating the blood perfusion pattern, assumed to be the only unknown biophysical parameter (Kleinman and Roemer 1983, Clegg and Roemer 1985a, Clegg and Roemer 1985b, Liauh et al. 1991, Liauh and Roemer 1993). Divrik et al. (1984) modelled six perfusion zones in 50 mm of canine muscle. Reconstructed and experimentally measured one-dimensional steady-state temperature profiles showed reasonable agreement when a microthermocouple was placed at the center of each modelled perfusion zone. It was also reported that complete three dimensional temperature fields could be accurately reconstructed (error < 1°C) from noisy measurements provided that a sensor was placed in each of seven perfusion zones and sensor sampling was optimized (Liauh et al. 1991). However, optimal sampling was shown to depend on the perfusion pattern and magnitude.

Presently, only final temperature distributions have been reconstructed for a post-treatment evaluation of the completed therapy. The potential for combining on-line thermometry with thermal modelling to reconstruct transient temperature distributions has yet to be investigated. The problem is particularly difficult for ILP treatments due to the large temperature gradients induced and tissue phase transitions which occur during treatment.

1.4 Scope of the Thesis

Most current thermal models of ILP assume temporally invariant optical and thermal properties. This assumption is poor, because the thermally-induced phase transitions during ILP are substantial. Coagulative necrosis has been shown to increase optical scattering (Pickering et al. 1994, Splinter et al. 1991, Jaywant et al. 1993) while vaporization of tissue water decreases thermal conductivity (Thomsen 1991). Tissue browning has been shown to increase optical absorption and char is opaque. These effects need to be considered when using models to help determine treatment protocols.

The general goal of this thesis is to determine how thermally-induced phase transitions affect tissue temperatures during ILP and to incorporate these effects into thermal models of ILP. To this end, three related investigations are undertaken.

Part 1: This is a theoretical investigation of ILP at 1064 nm in liver. The influence on temperature distributions of blood perfusion and increased scattering due to tissue coagulation is assessed. Irradiation parameters are chosen to keep the maximum tissue temperature below 100°C, which avoids vaporization, charring and smoke production. Lesion formation is assessed based on the time-temperature history of tissues.

Part 2: The dynamics of tissue charring are assessed. Charring at the fiber tip is centrally important to ILP because it influences both lesion size and image characteristics. Yet the time of onset and temperature of charring, T_{char}, have not been investigated. T_{char} cannot be measured directly during ILP because steep temperature gradients always exist near the fiber tip. A determination of T_{char}

based on both measurement and modelling of transient temperature distributions for Nd:YAG (1064 nm) and diode (800 nm) laser irradiations with a plane-cut fiber tip is undertaken.

Part 3: A feasibility study of on-line temperature reconstruction during ILP is undertaken for the case where the thermophysical and optical properties and blood perfusion patterns of tissue are unknown and may change temporally. A parameter estimation algorithm is developed to obtain estimates of the biophysical properties and thereby reconstruct complete temperature profiles at discrete intervals during treatment. Simulated temperature measurements for Nd:YAG (1064 nm) laser irradiations are used as input data. The performance of the reconstruction algorithm is evaluated by comparing the estimated parameters and reconstructed temperature profiles with those used to simulate the input temperature measurements. The parameter estimation algorithm is also tested *ex vivo* in lean bovine muscle.

CHAPTER 2. Background Theory

2.1 Optical Propagation in Tissue

Optical propagation in random or turbid media is characterized by the absorption and scattering of light. In soft tissues, the absorption of light in the visible (300 nm to 700 nm) and near-infrared (700 nm to 1100 nm) is influenced principally by the presence of water and endogenous chromophores (pigments) such as melanin and hemoglobin (Svaasand et al. 1985, Boulnois 1986). At optical wavelengths, experimental evidence shows that soft tissues are highly scattering with a strong forward scattering component. Multiple scattering diffuses the optical energy through the tissue and is influenced by various morphological features such as changes in the refractive index at cell boundaries and the presence of intracellular organelles. The size of these structures relative to the wavelength of the incident light determines the scattering angle.

Microscopic tissue inhomogeneities make the problem of solving the angular scattering distribution mathematically intractable. Scattering is considered to be due to refraction from objects of size equal to or greater than the wavelength of the incident light and can be approximately modelled using Mie theory (Kerker 1969).

The propagation of light in tissues can be described in terms of the transport of neutral particles which are absorbed and scattered (without energy loss). The radiative transport equation used to describe optical distributions in highly scattering tissues is the one-speed approximation to the linearized Boltzmann Transfer Equation, derived by balancing the various mechanisms by which particles are gained or lost from an arbitrary volume (Weinberg and Wigner 1958). For continuous-wave optical energy the time-independent equation is

$$\Omega \cdot \nabla I(r,\Omega) = -\left(\mu_a(r) + \mu_s(r)\right) I(r,\Omega) + \int_{4\pi} d\Omega' \frac{d\mu_s(r,\Omega' \rightarrow \Omega)}{d\Omega'} I(r,\Omega') + S(r,\Omega) \quad (2.1)$$

where $I(r,\Omega)$ (W/cm^2-steradian) is the radiance, defined as the optical power per unit area per unit solid angle, r is the spatial coordinate, Ω is the unit direction vector ($d\Omega$ is a solid angle), μ_a (cm^{-1}) is the linear absorption coefficient defined as the probability per infinitesimal pathlength that a photon will be absorbed, μ_s (cm^{-1}) is the linear scattering coefficient defined as the probability per infinitesimal pathlength that a photon will be scattered and S (W/cm^3) is a source term. The left side of (2.1) represents the net leakage per steradian of photons into or out of a small volume. The first term on the right side of (2.1) represents the loss of photons travelling in the direction, Ω, due to absorption or scattering in the volume. The second term represents photons scattering into, Ω, from direction, Ω'. The last term represents source photons generated with direction, Ω.

In the above description of photon transport, $d\mu_s(r,\Omega'\rightarrow\Omega)/d\Omega'$ is the differential scattering cross-section, defined as the probability per infinitesimal pathlength that a photon at r initially moving in the direction, Ω', will be scattered into a new direction, Ω. Dividing the differential scattering cross-section by the linear scattering coefficient yields a normalized quantity known as the phase function (a probability density function), defined as the angular distribution of light per scattering event. In random media, the phase function depends only on the cosine of the angle between the incident and scattered radiation. The mean cosine, g, of this scatter angle is often used as a single, lumped index of the forwardness of scatter. Scattering is predominantly backward when $g<0$ and forward when $g>0$. For isotropic scattering, $g=0$. Experimental evidence shows that scattering in soft tissues in the visible range is anisotropic with a strong forward component, characterized by g values of 0.70 to 0.98 (Cheong et al. 1990). The effects of anisotropic scattering can be incorporated approximately into the radiative transport equation by multiplying the scattering coefficient by (1-g) (Arnfield et al. 1988). The scattering coefficient is then replaced by this reduced scattering coefficient, $\mu_s' = (1-g)\mu_s$, with the phase function taken as isotropic.

The sum of the absorption and reduced scattering coefficients is defined as the total transport coefficient, μ_{tr}, given by

$$\mu_{tr} = \mu_a + (1-g)\mu_s \tag{2.2}$$

The ability of the optical energy to penetrate tissue is determined by the inverse of μ_{tr}, which is the optical mean free path. ILP is generally performed using optical energy in the near infrared (700 nm to 1100 nm) because of maximal tissue penetration at these wavelengths. Above 1300 nm optical penetration is greatly reduced due to increased absorption by water. Below 700 nm, tissue chromophores limit optical penetration, as indicated by the absorption spectrum in Fig. 2.1.

In the near infrared, the absorption and scattering coefficients for soft tissues range from approximately 0.02 - 5 cm^{-1} and 10 - 200 cm^{-1}, respectively. Heavily pigmented tissues such as liver or highly scattering tissues such as brain will, by definition, have low optical penetration. The optical penetration depth of 1064 nm light in soft tissues ranges from 3 to 8 mm (Svaasand et al. 1985).

Exact solutions to (2.1) are difficult to obtain due to the integro-differential nature of the equation. However, for many medical applications, solving for the radiance is not essential. Given that the absorption of light is independent of the direction of propagation, a more important quantity in dosimetry is the integral of the radiance over 4π solid angle, known as the irradiance (W/cm^2)

$$\phi(r) = \int_{4\pi} I(r,\Omega)\,d\Omega \qquad (2.3)$$

The irradiance describes the optical power passing through an infinitesimal sphere per cross-sectional area of that sphere.

For simplified geometries, such as an isotropic point optical source of

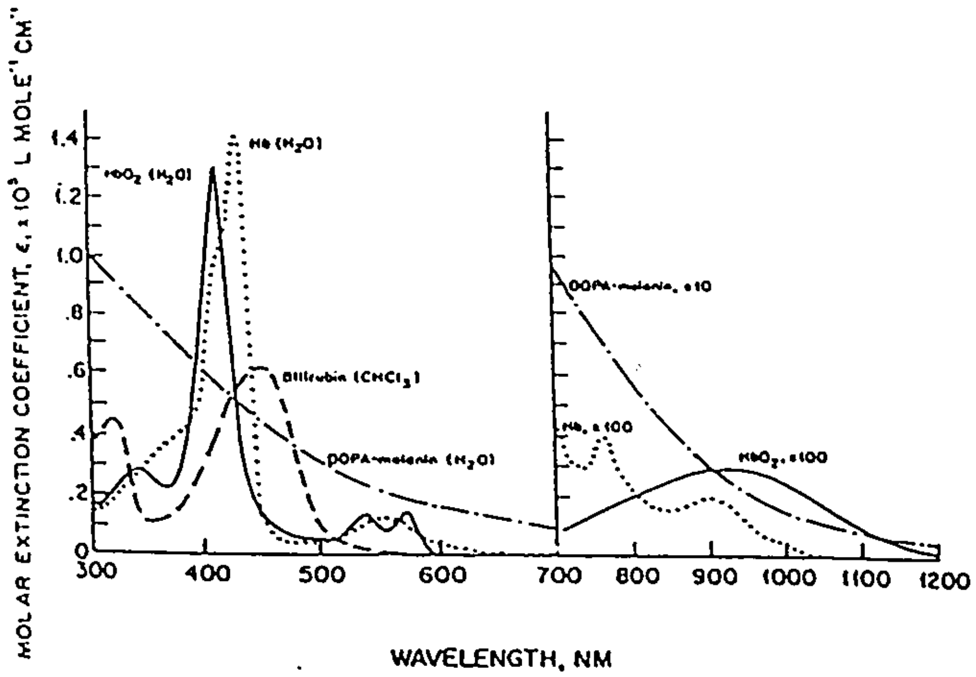

Figure 2.1. The absorption spectrum for various biological substances expressed as a molar extinction coefficient (from Anderson 1991). The discontinuity at 700 nm is a result of a shift in the magnitude of the coefficient values labelled on the y-axis, with magnitude reductions labelled on each plot (i.e. HbO_2 = 100, refers to the y-axis labels being reduced by 2 orders of magnitude).

power ϕ_{point} in an infinite homogeneous tissue medium with anisotropic scattering, an exact solution to (2.1) is given by (Weinberg and Wigner 1958)

$$\phi(r) = \frac{\phi_{point}}{4\pi}\left[\frac{e^{-\mu' r}}{r^2} + \frac{\beta e^{-r/L_{opt}}}{Dr}\right] \tag{2.4}$$

where the optical diffusion length, L_{opt} (cm), the diffusion coefficient, D (cm) and the attenuation parameters β and μ' (cm^{-1}) as modified by Arnfield et al. (1988) for anisotropic scattering are given by

$$L_{opt} \approx \frac{1}{\sqrt{3\mu_a\mu_{tr}}}\left[1 + \frac{0.4\mu_a}{\mu_{tr}}\right], \quad D = \mu_a L_{opt}^2$$

$$\beta = \frac{2\mu_a}{\mu_s'}\left[\frac{(\mu_{tr}^{\ 2}-L_{opt}^{-2})}{(L_{opt}^{-2}-\mu_a\mu_{tr})}\right], \quad \mu' = \frac{5\mu_{tr}}{4} \tag{2.5}$$

The first term in (2.4) describes the uncollided component of the irradiance which decays exponentially and with inverse square of distance from the source. The second term describes the scattered or diffuse component of the irradiance.

More commonly, it is assumed that the radiance is only weakly dependent on direction. This gives rise to an approximation of (2.1) known as the steady-state diffusion equation (Duderstadt and Hamilton 1976)

$$-\nabla \cdot D\nabla\phi(r) + \mu_a\phi(r) = S(r) \tag{2.6}$$

This equation is more amenable to solution and is most valid in scatter dominated media ($\mu_a << \mu_s$) such as soft tissues in the visible and near infrared. However, the underlying assumption limits the accuracy of the solution within a few mean free paths, $1/\mu_{tr}$, from sources and boundaries where the radiance certainly depends on direction. Diffusion theory has been used extensively to solve for optical distributions in soft tissues with applications in optical imaging and spectroscopy (Paulsen and Jiang 1995, Pogue et al. 1995, Arridge et al. 1993) and therapeutic laser heating (Dowden et al. 1987, Davies et al. 1989, Anvari et al. 1994b).

2.2 Heat Transfer in Tissue

The conversion of optical energy into thermal energy involves the absorption of a photon by a target molecule (i.e water, hemoglobin, melanin). The target molecule, now promoted to a vibrational-rotational excited state, transfers energy to nearby molecules via inelastic scattering (Boulnois 1986, Welch 1984). The process is efficient in soft tissues due to the large number of vibrational states in biomolecules and large collision cross-sections. As photons are absorbed in tissue the optical energy is converted into a distributed heat source.

The propagation of heat is determined by the mechanisms of thermal storage, conduction and convection. Thermal storage and conduction properties of soft tissues depend principally on tissue composition (Duck 1990). Soft tissues are composed primarily of water, protein and fat, with water representing 75-85% of the tissue.

The processes by which tissue accommodates energy inputs in the form of heat are governed by the laws of thermodynamics. The application of heat transfer theory to living tissues necessarily involves the description of heat exchange between tissue and blood. Generally, heat transferred to blood is removed by blood flow. Quantifying this cooling effect requires knowledge of the vascular architecture and blood flow rates. A comprehensive review of modelling heat transfer in blood perfused tissues is given by Arkin et al. (1994).

Heat exchange can be separated into large vessel (diameter > 1 mm) cooling, which is localized and should be modelled as a distinct cooling term (Lagendijk 1982, Whelan et al. 1995, Kolios et al. 1995) and cooling from a continuum of small vessels. Accurate prediction of the latter effect poses a difficult problem because modelling the complex microvascular architecture has thus far proved mathematically intractable. Approximate models have been developed and can be divided into single equation and 3 equation descriptions.

The first of the single equation descriptions was proposed by Pennes (1948) and is called the Bio-Heat Transfer Equation (BHTE)

$$\rho c \frac{\partial T}{\partial t} = \nabla \cdot k \nabla T + Q_M + Q_S + w_b c_b (T_a - T) \tag{2.7}$$

where ρ (g/cm^3) is the tissue density, c (J/g/°C) is the tissue heat capacity, k (W/cm/°C) is the tissue thermal conductivity, w_b (g/cm^3/s) is the average volumetric blood perfusion rate, defined as the mass of blood perfusing through a unit volume of tissue per unit time, c_b is the blood heat capacity and T_a is the arterial temperature.

The first two terms in (2.7) comprise the ordinary transient heat conduction equation and represent the rate of change of stored thermal energy in the volume and heat conducted into and out of the volume, respectively. Q_M (W/cm^3) represents the thermal energy generated from metabolic processes and Q_S (W/cm^3) represents the total energy absorbed in the volume from a source. The last term represents the net thermal energy transported out of the volume by blood in the microvasculature. Pennes assumed that heat exchange between blood and tissue occurs only in the walls of capillaries (diameter < 2 μm) where blood velocity is low. The Pennes model proposed that arterial blood enters the capillary bed and equilibrates with the surrounding tissue, thus entering the venous circulation at tissue temperature, T. The thermal energy carried away by the venous blood could then be modelled as a volumetric isotropic heat sink. Thus, convective cooling from a continuum of small vessels is implicit in the BHTE.

The Pennes model was generally accepted until the late 1960's when renewed interest in therapeutic hyperthermia spawned the need for a better understanding of blood cooling. Wulff (1974) criticized Pennes' scalar treatment of the convective heat transport by blood in (2.7). However, any attempt to specify a blood velocity vector at the microscopic level was marred by the complex nature of the vascular system.

It appears that Chen and Holmes (1980) were the first to predict theoretically the thermal equilibration lengths of blood vessels. Defined as the length of blood vessel for which the temperature difference between blood and heated tissue is reduced to 1/e of the initial value, the thermal equilibration length, l_e, is a measure of the heat exchange efficiency between blood and tissue. If $l_e < l$, the true vessel length, the blood in the vessel will heat to thermal equilibrium with the surrounding tissue, thereby carrying away thermal energy. Chen and Holmes (1980) reported that thermal equilibrium occurs not in the capillaries, as assumed by Pennes, but in vessels that were greater than 50 μm in diameter (arterioles and venules). Based on these findings, a single equation description known as the Chen/Holmes (CH) model was developed with two additional heat exchange terms incorporated into (2.7). However the CH model requires knowledge of vessel diameter and orientation making its application more difficult than the Pennes model.

Later it was recognized that, in tissues, arterial and venous vessels are frequently in close proximity to each other, with blood flowing in opposite directions. Jiji, Weinbaum and Lemons (1984) proposed a three equation model (WJL model) which coupled the countercurrent heat transfer that occurs between paired arterial and venous blood flows with that of tissue. The WJL model also required knowledge of the vessel diameters and orientation. The WJL model predicted that significant countercurrent heat exchange occurred in the vessels in the 50 μm to 300 μm diameter range. A recent investigation by Zhu and Weinbaum (1995) indicated that the critical diameter range is 80 μm to 200 μm.

The difficulty of applying the three coupled equation model to practical vascular architectures led Weinbaum and Jiji (WJ) to develop the simplified and easily solvable WJ model (Weinbaum and Jiji 1985). The derivation of the WJ model was based on the microvascular architecture in skeletal muscle where most vessels with diameters greater than 50 µm ("thermally significant") occur in countercurrent pairs. It was assumed that all heat conducted out of the arterial wall is conducted through the venous wall such that the increase in tissue temperature between vessels is negligible. It is further assumed that the tissue temperature can be approximated by the average temperature of the closely spaced countercurrent pair. These assumptions facilitated simplifications to the original WJL model producing a single equation description known as the Effective Thermal Conductivity Equation (ETCE)

$$\rho c \frac{\partial T}{\partial t} = \nabla \cdot k_{eff} \nabla T + Q_M + Q_S \tag{2.8}$$

where k_{eff}, the effective thermal conductivity (W/cm/°C), describes the enhancement in thermal conductivity due to incomplete countercurrent heat exchange between paired vessels and the local blood perfusion, and is given in scalar form by

$$k_{eff} = k\left(1 + \frac{\pi^2}{4\sigma k^2} n r_a^2 k_b^2 Pe^2\right) \tag{2.9}$$

where k_b is the thermal conductivity of blood, σ is a shape factor related to the cross-sectional vessel geometry, n is the number density of vessel pairs per unit area, r_a is the artery radius and Pe is the dimensionless Peclet number = $2\rho_b c_b r_a v/k_b$ which characterizes the flow of blood of velocity, v. The WJ model predicted that the thermal conductivity was enhanced by factors of 1.05 and 3.5

in muscle with 50 μm and 300μm diameter vessels, respectively.

The applicability of the WJ and Pennes' models depends on the blood vessel diameters modelled (Charney et al. 1990). It has been suggested that the WJ model is applicable in tissues containing blood vessels with diameters < 200 μm and $l_e/l < 0.2$ (Song et al. 1995). Recent studies by Song et al. (1995) and Zhu et al. (1995) indicate that k_{eff}/k differs from unity only for vessel diameters > 100 μm and increases with increasing vessel diameter up to 1.3 and 1.6 for *ex vivo* preparations of rat spinotrapezius and cremaster muscles, respectively. The Pennes model appears to be valid only in tissues with vessel diameters < 300 μm and a $l_e/l < 0.6$ (Xu et al. 1991). The domain of accuracy of these models continues to be investigated.

Despite concerns expressed about the validity of the WJ and Pennes models, they continue to be used extensively to model *in vivo* temperature distributions in various soft tissues including liver (Beacco et al. 1994, Kolios et al. 1995), kidney (Xu et al. 1991) and prostate (Anvari et al. 1994b, Yuan et al. 1995), most likely because of their simplicity.

Thus, the Pennes and WJ models were used to determine the transient temperature calculations presented in this thesis. The corresponding model equations, (2.7) and (2.8), were combined into a single compact expression which will be referred to as the BHTE-ETCE

$$\rho c \frac{\partial T}{\partial t} = \nabla \cdot k_{eff} \nabla T + Q_S + w_b c_b (T_a - T) \qquad (2.10)$$

where, for deposition of optical energy, $Q_S = \mu_a \phi$. Note that Q_S is the term that links the mathematical descriptions of heat transfer (2.10) and optical propagation (2.4-2.6). During therapeutic heating the Q_M term is generally negligible compared to Q_S and is therefore omitted from (2.10).

The penetration of heat in blood-perfused tissues has been characterized by Svaasand et al. (1985) for one-dimensional problems based on the Pennes model at steady-state. If one assumes a point heat source immersed in an infinite blood-perfused medium, the characteristic thermal penetration depth, d_v, is the distance at which the temperature is reduced to 1/e of the maximum value at the source (origin) and is given by

$$d_v = \left(\frac{k}{\rho c w_b^*} \right)^{1/2} \qquad (2.11)$$

where w_b^* (s^{-1}) is defined as the volume of blood flowing through a unit volume of tissue per second. Eq. (2.11) assumes that the density and specific heat of tissue and blood are similar. Estimated thermal penetration depths as a function of perfusion rate for various tissues are shown in Table 2.1.

The thermal conductivity and specific heat for soft tissues range from ~ 0.0030 - 0.0055 W/cm/°C and ~ 3.2 - 4.0 J/g/°C, respectively (Bowman et al. 1975). The density range is ~ 0.99 - 1.2 g/cm^3 (Duck 1990). The ratio of $k/\rho c$ in (2.11) is defined as the thermal diffusivity and depends principally on water

Table 2.1. Thermal penetration depths in various soft tissues (from Svaasand et al. 1985).

Tissue	w_b^* (s^{-1})	d_v (mm)
Kidney	5-10 (× 10^{-2})	1.1-1.5
Brain cortex	7-20 (× 10^{-3})	2.5-4.0
Skin	2-7 (× 10^{-3})	4-7
Muscle	3-20 (× 10^{-4})	7-20
Fat	1-3 (× 10^{-4})	20-35

content. Cooper and Trezek (1971) derived a set of empirical equations for the thermophysical properties of tissues with a 71%-84% water content based on the mass fractions of water (m_w), protein (m_p) and fat (m_f)

$$\begin{aligned} k &= \rho * 10^{-2}\left[0.628 m_w + 0.117 m_p + 0.231 m_f\right] \\ c &= 4.2 m_w + 1.09 m_p + 2.3 m_f \\ \rho &= \left[m_w + m_p/1.54 + m_f/0.815\right]^{-1} \end{aligned} \tag{2.12}$$

Values of m_w, m_p and m_f for various soft tissues have been published in a compilation of tissue properties by Duck (1990).

In soft tissues, the optical penetration is generally much less than the thermal penetration, such that the pattern of absorbed radiation determines the pattern of temperature increases (McKenzie 1990).

2.3 Thermal Damage Prediction

Models predicting the accumulation of thermal damage are based on a seminal paper by Arrhenius (1889) who quantified the effect of heat on the chemical rate kinetics in sugar solutions by the reaction rate constant

$$C = A\exp\left[-\frac{\Delta E}{RT}\right] \tag{2.13}$$

where A (s^{-1}) is a frequency factor, ΔE (J/mole) is the reaction's activation energy, R (J/mole/°K) is the universal gas constant and T(°K) is the temperature.

The extent of thermal damage in tissues has been shown to depend on the time-temperature history (Dewey et al. 1976, Overgaard and Suit 1979) and can be determined by integrating (2.13) over time (Birngruber 1979)

$$\Omega(r,t) = A\int_0^t \exp\left[-\frac{\Delta E}{RT(r,t')}\right]dt' \tag{2.14}$$

Equation (2.14) is known as the Arrhenius damage integral and describes the loss rate of undamaged target molecules.

The values of A and ΔE in (2.14) depend on tissue type and biological endpoint. These reaction coefficients have been measured experimentally for thermal denaturation of skin (Henriques 1947) and liver (Hillenkamp 1979). Beacco et al. (1994) reported good agreement between measured coagulative necrosis and that predicted by (2.14) in rat liver *in vivo*. However, evaluation of (2.14) is computationally intensive given the nonuniform transient temperature fields induced during ILP.

Sapareto and Dewey (1984) reported that published values of A and ΔE for various *in vitro* and *in vivo* tissues exposed to hyperthermic temperatures suggested that the exponential in (2.14) can be well approximated by 0.25 at temperatures below 43°C and by 0.5 at temperatures between 43°C and 50°C. This was used to derive a threshold thermal dose approximation to the integral in (2.14) which converts thermal exposures to the equivalent-time at 43°C. In other words, the time required to produce an isoeffect at temperature T is converted to the time required to produce the same effect at 43°C, t_{43}, given by

$$t_{43} = \sum_{t=t_o}^{t=t_{final}} C_o^{(43 - T_{avg})} \Delta t \quad with \quad C_o = \begin{cases} 0.25, & T < 43°C \\ 0.5, & T \geq 43°C \end{cases} \qquad (2.15)$$

where T_{avg} is the average temperature during the time interval, Δt. During rapid temperature changes, one must increase the frequency of temperature measurements to improve the accuracy of the calculated thermal dose. The threshold value of t_{43}, for thermal damage depends on tissue-type. Experimental evidence for protracted exposures at hyperthermic temperatures indicates that a t_{43} of 1 hr (3600 s) induces necrosis in a variety of tissue-types (Sapareto and Dewey 1984).

Eq. (2.15) may not be a good predictor of thermal damage at high temperatures such as induced during ILP. However, a threshold thermal dose model similar in form to (2.15), in which a 1°C increase in temperature halves the time required to induce necrosis, has been validated *in vivo* in canine bladder up to 60°C (Linke et al. 1972). Furthermore, using (2.15) for a threshold thermal dose of 44°C for 3600 s, Davies et al. (1989) predicted reasonably the dimensions of laser-induced thermal necrosis in canine liver observed by Steger et al. (1988). Eq.(2.15) is therefore used to predict thermal lesion formation in this thesis.

2.4 Parameter Estimation Formalism

Parameter estimation techniques are used to estimate the unknown parameters of a system. The system is represented by a mathematical model with unknown parameters estimated by manipulation until the model agrees with measured data. Problems of this type, fitting models to data, are generally solved using the method of nonlinear least squares (Gill et al. 1993). This method has been employed to estimate tissue properties including blood perfusion (Wei et al. 1995, Liauh et al. 1993) effective permeability (Laible et al. 1994), thermal conductivity and specific heat (Ouyang 1992), optical absorption and scattering (Paulsen and Jiang 1995, Pogue et al. 1995).

A dynamic parameter estimation procedure has been developed to estimate the biological properties of soft tissues during interstitial laser heating. Measured temperatures at discrete locations in the tissue are used to inverse-solve for the biophysical properties (parameters) of the heated tissue system. Parameter estimates are then used to solve the direct forward problem for temperature, thereby reconstructing temperatures in the entire thermal field. The presented estimation formalism allows for transient temperature response data to be used to estimate and update the biophysical properties during heating.

Denote the temperature measured by the mth of M sensors at the sth of S discrete times by $T^{s}_{meas,m}$. The resulting (MS)-vector of temperature measurements is represented by

$$T_{meas} = \left[T_{meas,1} \; T_{meas,2} \cdots T_{meas,m} \cdots T_{meas,M}\right]^{T} \tag{2.16}$$

where

$$T_{meas,m} = \left[T^{1}_{meas,m}\; T^{2}_{meas,m} \cdots T^{s}_{meas,m} \cdots T^{S}_{meas,m}\right] \tag{2.17}$$

and ^{T} refers to the transpose of the matrix.

Let the desired model-predicted temperature function be represented by $T_{pred}(\mathbf{P})$ where $\mathbf{P}$ is the vector of unknown biological properties (parameters) to be estimated. Denote the estimate of the n^th^ of N biological parameters in the z^th^ of Z discretized spatial zones by P_n^z. The total number of unknown parameters to be estimated is represented by the (NZ)-vector

$$P = \left[P_1\; P_2 \cdots P_n \cdots P_N\right]^T \tag{2.18}$$

where

$$P_n = \left[P_n^1\; P_n^2 \cdots P_n^z \cdots P_n^Z\right] \tag{2.19}$$

The least-squares objective function to be minimized is the difference between the measured and model-predicted temperatures at all sensor locations and times

$$F(P) = \frac{1}{2} \sum_{s=1}^{S} \sum_{m=1}^{M} \left(T^{s}_{pred,m}(P) - T^{s}_{meas,m}\right)^2 \tag{2.20}$$

where $T^s_{pred,m}$ are generated from the model-predicted temperature function, $T_{pred}(\mathbf{P})$, and take the same vector form as (2.16) and (2.17). The 1/2 is included in (2.20) to avoid the appearance of a factor of two in the derivatives.

Assume that F(P) is a smooth multivariate function which can be closely approximated by a quadratic function in a small neighbourhood about the current estimate of parameters, $\mathbf{P}_i$. Then a 3-term Taylor-series expansion of F(P) about $\mathbf{P}_i$ can be used as a basis for developing an iterative parameter updating algorithm (Gill et al. 1993)

$$F(P) = F(P_i) + g^T(P_i)\Delta P + \frac{1}{2}\Delta P^T H(P_i)\Delta P \tag{2.21}$$

where $\Delta\mathbf{P}=\mathbf{P}-\mathbf{P}_i$ is a step change in the neighbourhood of $\mathbf{P}_i$ with the local gradient, $\mathbf{g}(\mathbf{P}_i)$, and the local Hessian $\mathbf{H}(\mathbf{P}_i)$, of the least-squares objective function (2.20) given generally by

$$g=\frac{\partial F(P)}{\partial P}=\sum_{m=1}^{M}\sum_{s=1}^{S}\left(T^s_{pred,m}(P) - T^s_{meas,m}\right)\frac{\partial T^s_{pred,m}(P)}{\partial P} \tag{2.22}$$

$$\begin{aligned} H=\frac{\partial^2 F(P)}{\partial P^2}=\sum_{m=1}^{M}\sum_{s=1}^{S}\left(T^s_{pred,m}(P) - T^s_{meas,m}\right)\frac{\partial^2 T^s_{pred,m}(P)}{\partial P^2} + \\ \frac{\partial T^s_{pred,m}(P)}{\partial P}\frac{\partial T^s_{pred,m}(P)}{\partial P} \end{aligned} \tag{2.23}$$

F(P) in (2.20) is then minimized by setting to 0 the partial derivatives, $\partial F/\partial P$ in (2.21), which gives

$$H\Delta P = -g \tag{2.24}$$

Substituting (2.22) and (2.23) into (2.24) produces

$$\left(\sum_{m=1}^{M}\sum_{s=1}^{S}\left(T^s_{pred,m}(P) - T^s_{meas,m}\right)\frac{\partial^2 T^s_{pred,m}(P)}{\partial P^2} + \frac{\partial T^s_{pred,m}(P)}{\partial P}\frac{\partial T^s_{pred,m}(P)}{\partial P}\right)\Delta P = -\sum_{m=1}^{M}\sum_{s=1}^{S}\left(T^s_{pred,m}(P) - T^s_{meas,m}\right)\frac{\partial T^s_{pred,m}(P)}{\partial P} \tag{2.25}$$

The minimizing algorithm given by (2.25) is an application of the multidimensional Newton's Method with **ΔP** being the Newton direction.

Least-squares parameter estimation methods are typically based on the premise that the first-order term will dominate the second-order term in the Hessian of F (see (2.23)). This assumption is valid if the residuals tend to zero as **P** approaches the solution and facilitates an approximation to Newton's Method known as the Gauss-Newton Method (Gill et al. 1993)

$$\left(\sum_{m=1}^{M}\sum_{s=1}^{S}\frac{\partial T^s_{pred,m}(P)}{\partial P}\frac{\partial T^s_{pred,m}(P)}{\partial P}\right)\Delta P = -\sum_{m=1}^{M}\sum_{s=1}^{S}\left(T^s_{pred,m}(P) - T^s_{meas,m}\right)\frac{\partial T^s_{pred,m}(P)}{\partial P} \tag{2.26}$$

Equation (2.26) is expressed in matrix form as

$$J^T J \Delta P = -J^T\left(T_{pred} - T_{meas}\right) \tag{2.27}$$

where **ΔP** is an (NZ)-vector of the same form as **P** in (2.18) and (2.19) and **J** is the Jacobian matrix of $\mathbf{T}_{pred}$ given by the (MS) by (NZ) vector

$$J = \begin{bmatrix} \left[\dfrac{\partial T_{pred,1}}{\partial P_1}\right] & \left[\dfrac{\partial T_{pred,1}}{\partial P_2}\right] & \cdots & \left[\dfrac{\partial T_{pred,1}}{\partial P_N}\right] \\ \left[\dfrac{\partial T_{pred,2}}{\partial P_1}\right] & \ddots & & \vdots \\ \vdots & & \ddots & \vdots \\ \left[\dfrac{\partial T_{pred,M}}{\partial P_1}\right] & \cdots & \cdots & \left[\dfrac{\partial T_{pred,M}}{\partial P_N}\right] \end{bmatrix} \tag{2.28}$$

with submatrices of the form

$$\frac{\partial T_{pred,m}}{\partial P_n} = \begin{bmatrix} \dfrac{\partial T^1_{pred,m}}{\partial P^1_n} & \dfrac{\partial T^1_{pred,m}}{\partial P^2_n} & \cdots & \dfrac{\partial T^1_{pred,m}}{\partial P^Z_n} \\ \dfrac{\partial T^2_{pred,m}}{\partial P^1_n} & \ddots & & \vdots \\ \vdots & & \ddots & \vdots \\ \dfrac{\partial T^S_{pred,m}}{\partial P^1_n} & \cdots & \cdots & \dfrac{\partial T^S_{pred,m}}{\partial P^Z_n} \end{bmatrix} \tag{2.29}$$

The error matrix, $(\mathbf{T}_{pred} - \mathbf{T}_{meas})$, is given by

$$\left(T_{pred} - T_{meas}\right) = \begin{bmatrix} (T^1_{pred,1} - T^1_{meas,1}) \\ (T^2_{pred,1} - T^2_{meas,1}) \\ \vdots \\ (T^S_{pred,1} - T^S_{meas,1}) \\ \vdots \\ (T^1_{pred,M} - T^1_{meas,M}) \\ (T^2_{pred,M} - T^2_{meas,M}) \\ \vdots \\ (T^S_{pred,M} - T^S_{meas,M}) \end{bmatrix} \tag{2.30}$$

Solving for $\Delta\mathbf{P}$

$$\Delta P = -(J^T J)^{-1} J^T (T_{pred} - T_{meas}) \tag{2.31}$$

The quantity$(J^T J)^{-1} J^T$ is called the pseudo-inverse of J when J is rectangular. In parameter estimation problems, J is generally referred to as the "sensitivity" matrix. For this case, $\partial T^s_{pred,m} / \partial P^z_n$ represents the change in the model-predicted temperature at the m^th sensor location and s^th time due to an elemental change of the n^th parameter in the z^th zone.

Solutions to (2.31) can be unstable for ill-conditioned problems, when small changes in the measured temperature data effect large changes in the converged solutions. Ill-conditioning is a common feature of nonlinear least-squares problems. Previous investigators of temperature reconstruction by parameter estimation (Liauh et al. 1991, Liauh and Roemer 1993) compensated for ill-conditioning using Tikhonov regularization (Tikhonov 1963). This method recognizes that the diagonal elements in the inverted matrix, $(J^T J)^{-1}$, set the scale for the incremental parameter changes. By adding a scalar, λ, to the diagonal terms one can control or stabilize the scale of the increment. Liauh et al. (1991) reported that temperature distributions could be accurately reconstructed provided the proper choice for the regularization parameter was made. However, the optimal regularization parameter depended on the perfusion pattern and magnitude, factors which are generally unknown *a priori*.

Therefore a different approach, the Levenberg-Marquardt method (Bevington 1969), is employed here. This iterative technique automatically selects the optimal value for the regularization parameter. Thus, the updated parameter vector at the ξ+1th iteration, based on (2.31) with Levenberg-Marquardt regularization, is expressed as

$$P^{\xi+1} = P^{\xi} + \left[\left(J^T J + \lambda I \right)^{-1} J^T \left(T_{pred} - T_{meas} \right) \right]^{\xi} \tag{2.32}$$

Within each ξ interation, the internal Levenberg-Marquardt loop optimizes λ based on the reduction of the objective function (2.20). If λ is large the iterative parameter change, ΔP, is scaled down. Solving (2.32) for the new estimate of the parameter vector, $P^{\xi+1}$, requires knowledge of **J** evaluated at the present estimate of the parameter vector, P^{ξ}. The elements of the Jacobian matrix, the sensitivity coefficients, were estimated numerically using the influence coefficient method (Liauh et al. 1993). This method involves perturbing the latest estimate of a parameter by a factor ε and then solving for the new temperature using the forward finite difference

$$\begin{aligned} \frac{\partial T^k_{pred,m}}{\partial P^{\xi}_n} = & \left[T^k_{pred,m} \left(P_1, P_2, \ldots \left[P^1_n, P^2_n, \ldots (1+\varepsilon) P^{\xi}_n, \ldots P^{Z}_n \right], \ldots P_N \right) - \right. \\ & \left. T^k_{pred,m} \left(P_1, P_2, \ldots \left[P^1_n, P^2_n, \ldots \varepsilon P^{\xi}_n, \ldots P^{Z}_n \right], \ldots P_N \right) \right] / \varepsilon P^{\xi}_n \end{aligned} \tag{2.33}$$

ε was chosen to be 0.001. The iterative parameter estimation procedure given by (2.32) forms the basis of the temperature reconstruction algorithm presented in the next chapter.

CHAPTER 3. Materials and Methods

3.1 *Ex vivo* Bovine Muscle Heating Experiments

Interstitial laser photocoagulation was performed *ex vivo* in lean bovine muscle using the experimental system shown in Fig. 3.1. The energy source was either an Nd:YAG laser, maximum power of 20 W (Model C100 C.V.I. Laser Corporation, Albuquerque, NM, USA), or a diode laser, maximum power of 2 W (Laser Diode Inc., New Brunswick, NJ, USA), emitting continuous wave optical energies at 1064 nm or 800 nm, respectively.

For Nd:YAG irradiations, the emergent 2 mm diameter 1064 nm multimode beam, with 3.0 mrad beam divergence, was deflected 90° by a reflecting mirror towards a focusing lens which produced a narrow 200 µm diameter beam for coupling to the polished end of a plane-cut 400 µm optical fiber (Model 4410 Laser Therapeutics Inc., Buellton, CA, USA). The optical fiber rested in a fiber chuck held by an x,y,z translator. All components of the light delivery system were fixed to the top of an optical bench.

Coupling efficiency was optimized using an infrared sensor card (Model Q-42-R, Quantex, Rockville, MD, USA) for gross positioning of the fiber and then by adjusting the translator screws until the power, measured by a laser power

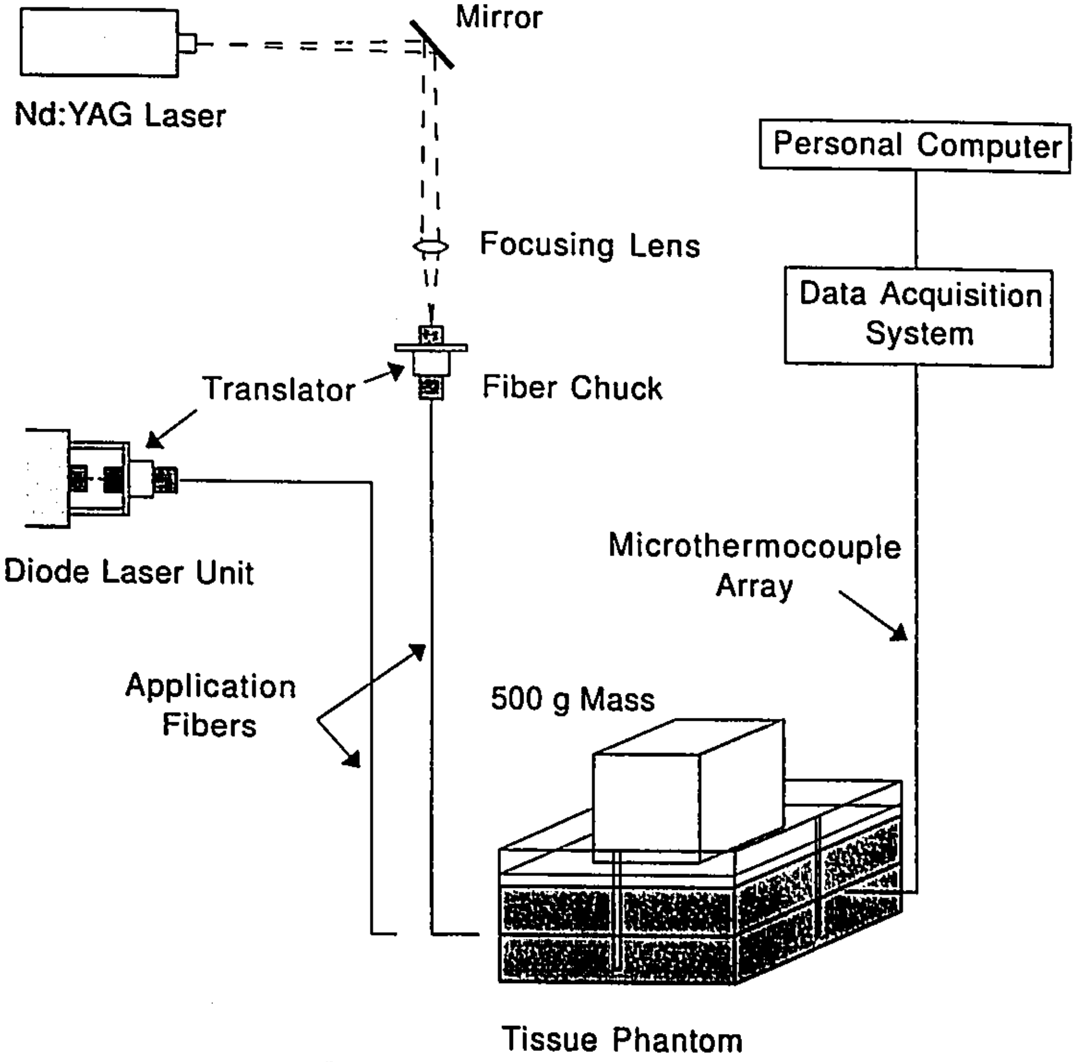

Figure 3.1 Apparatus for *ex vivo* heating experiments in bovine muscle.

meter (Ophir Model DG, Optikon, Waterloo, ONT, Canada) at the output end of the fiber, was maximal. The maximum coupling efficiency was approximately 80%.

For diode irradiations, a four channel diode laser treatment unit designed and built at the Hamilton Regional Cancer Centre was used. In each channel a maximum of 2 W of optical energy at 800 nm emerged from a diode fiber coupled to the laser diode by the manufacturer. The diode fiber rested in a fiber chuck, fixed to the front plate of the unit. A small portion of the diode fiber extended out from the front plate for coupling to the polished end of a plane-cut 400 µm applications optical fiber (Model 4410 Laser Therapeutics Inc., Buellton, CA, USA).

The applications fiber rested in a fiber chuck held by an x,y,z translator also fixed to the front plate of the unit. The diode and applications fiber were coupled by adjusting the screws of the translator until the two fibers were ~ 1 mm apart (visually). Fine horizontal and vertical adjustment continued until the power, measured by a Ophir laser power meter at the output end of the fiber, was maximal. A blow brush was used to remove dust from the face of the two fibers to prevent local absorption and then the two fibers were butted together using only axial adjustment. The maximum coupling efficiency was approximately 70 %.

The thermometry system was comprised of 0.009" diameter teflon coated copper/constantan (type T) microthermocouples (Model IT-18 Sensortek Inc., Clifton, NJ, USA). Linear 5-channel and 6-channel microthermocouple arrays were built by aligning axially microthermocouples spaced 2 mm apart, then securing them in position with 5-0 silk sutures (Model 1022-21, Cyanamid, Montreal, PQ, Canada). The microthermocouples were connected to a data acquisition and control system (Labmate series 7000, Sciemetric Instruments Inc. Nepean, ONT, Canada) which housed 16 channels for analog input. The Labmate was interfaced to an AST 286-16 MHz personal computer. Temperatures were calculated using least-squares curve fitting software (Level1-QB LL v. 3.0) based on the American National Standards Institute (ANSI) tables of thermoelectric voltage as a function of temperature.

A cubic lucite box of side length 10 cm was built to house tissue samples. Channels 1 mm thick were machined down the sides of the box to provide sites for positioning the optical fiber and microthermocouple array. A ~ 15 mm thick tissue section was placed onto the bottom of the box. The plane-cut end of the applications fiber was placed on the surface and near the center of the tissue. A linear array of microthermocouples was placed 1 mm from the fiber tip as shown in Fig. 3.2. A second tissue section of equal thichness was placed on top of the devices followed by a top plate and a 500 g mass to ensure good contact between the two tissue sections.

Fiber and microthermocouple array positioning were measured before and after each experiment and remained consistent within 0.5 mm. Laser power measurements were performed before and after each experiment.

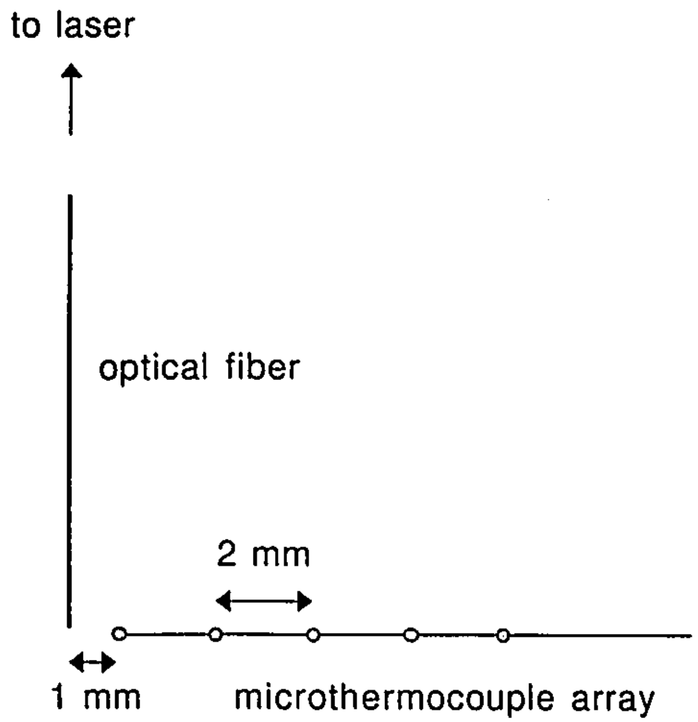

Figure 3.2 Optical fiber and microthermocouple array geometry for *ex vivo* heating experiments in bovine muscle.

3.2 Solutions to Heat Transfer and Optical Propagation Equations

3.2.1 1-D Homogeneous Tissues (Quasi-Analytical Solution)

In highly scattering tissues a plane-cut optical fiber is accurately modelled as being an isotropic point source. Therefore, for homogeneous tissues we consider an analytical solution to the Boltzmann radiative transfer equation for which the irradiance, $\phi(r)$, from an isotropic point source in an infinite homogeneous tissue medium with anisotropic scattering is given by (2.4).

Our application of the 1-D homogeneous description requires a solution to (2.10) for $w_b=0$, the WJ model, expressed in spherical coordinates as

$$\rho c \frac{\partial T(r,t)}{\partial t} = \frac{k_{eff}}{r^2}\frac{\partial}{\partial r}\left[r^2\frac{\partial T(r,t)}{\partial r}\right] + \mu_a\phi(r) \qquad (3.1)$$

Solutions to (3.1) can be obtained using standard Green's function methods, as employed by Vyas and Rustgi (1992). For a steady power source of unit power (1 W) at r', the solution to (3.1) is the Green's function (Carslaw and Jaegar, 1958)

$$T_G(r-r',t) = \frac{1}{4\pi k_{eff}|r-r'|}\, erfc\left[\frac{|r-r'|}{L_{th}(t)}\right] \qquad (3.2)$$

where $r = |\mathbf{r}|$ is the radial distance from the source, erfc() is the complementary error function and L_{th} is the thermal diffusion length given by $(4k_{eff}t/\rho c)^{1/2}$. The temperature increase at time t is a convolution of the steady optical source and T_G given in spherical coordinates by

$$T(r,t) = \int_0^{\infty}\int_0^{\pi}\int_0^{2\pi} \mu_a \phi(r')\ T_G(|r-r'|,t) r'^2 \sin\theta' d\phi' d\theta' dr' \tag{3.3}$$

Substituting (2.4) into (3.3) and evaluating the integrals gives

$$\begin{aligned} T(r,t) = \frac{\mu_a \phi_{point} L_{th}(t)}{8\pi k_{eff} r} \int_0^{\infty} \left(\frac{e^{-\mu' r'}}{r'^2} + \frac{\beta e^{-r'/L_{tr}}}{r' D} \right) & \left[\frac{e^{-\left(\frac{r-r'}{L_{th}(t)}\right)^2} - e^{-\left(\frac{r+r'}{L_{th}(t)}\right)^2}}{\pi^{1/2}} \right. \\ & \left. - \left(\frac{|r-r'|}{L_{th}(t)} \right) erfc\left(\frac{|r-r'|}{L_{th}(t)} \right) + \left(\frac{r+r'}{L_{th}(t)} \right) erfc\left(\frac{r+r'}{L_{th}(t)} \right) \right] r' dr' \end{aligned} \tag{3.4}$$

Equation (3.4) was evaluated numerically using a 21-point Gauss-Kronrod rule (Stroud and Secrest 1963).

3.2.2 1-D Inhomogeneous Tissues (Finite Difference Solution)

For 1-D inhomogeneous tissues we consider finite difference solutions to the two coupled equations, (2.6) and (2.10), for an interstitially implanted optical fiber delivering a steady power ϕ_{point} (W) from its plane-cut tip into highly scattering inhomogeneous tissue. Eqs. (2.6) and (2.10) are expressed in spherical coordinates with radially dependent coefficients

$$-\frac{1}{r^2}\frac{\partial}{\partial r}\left[r^2 D(r) \frac{\partial \phi(r)}{\partial r} \right] + \mu_a(r)\phi(r) = \phi_{point}\delta(r) \tag{3.5}$$

$$\rho(r)c(r)\frac{\partial T(r,t)}{\partial t} = \frac{1}{r^2}\frac{\partial}{\partial r}\left[r^2 k_{eff}(r)\frac{\partial T(r,t)}{\partial r}\right] + \mu_a(r)\phi(r) + w_b(r)c_b(r)\left(T_a - T(r,t)\right) \tag{3.6}$$

where δ(r) is the 3-dimensional Dirac delta (cm^{-3}).

Finite differencing was used to solve the two coupled equations, (3.5) and (3.6), for irradiance, $\phi(r)$, and temperature, T(r,t), respectively. Spatial derivatives were approximated using the energy balance formulation (Becker 1986). The spatial finite differencing scheme is shown in Fig. 3.3. The temporal derivative was forward differenced, and the temperature specification was otherwise implicit with respect to time.

For spherical geometry, energy balance is maintained, by multiplying (3.5) and (3.6) by $4\pi r^2$ and integrating from $r_{n-1/2}$ to $r_{n+1/2}$, with the assumption that tissue properties are constant over the interval n

$$-4\pi\int_{r_{n-1/2}}^{r_{n+1/2}} r^2\frac{1}{r^2}\frac{\partial}{\partial r}\left[r^2 D(r)\frac{\partial\phi(r)}{\partial r}\right]dr + 4\pi\int_{r_{n-1/2}}^{r_{n+1/2}} r^2\mu_a(r)\phi(r)dr = 4\pi\int_{r_{n-1/2}}^{r_{n+1/2}} r^2\phi_{point}\delta(r)\,dr \tag{3.7}$$

$$4\pi\int_{r_{n-1/2}}^{r_{n+1/2}} r^2\rho(r)c(r)\frac{\partial T(r,t)}{\partial t}\,dr = 4\pi\int_{r_{n-1/2}}^{r_{n+1/2}} r^2\frac{1}{r^2}\frac{\partial}{\partial r}\left[r^2 k_{eff}(r)\frac{\partial T(r,t)}{\partial r}\right]dr + 4\pi\int_{r_{n-1/2}}^{r_{n+1/2}} r^2\mu_a(r)\phi(r)\,dr + 4\pi\int_{r_{n-1/2}}^{r_{n+1/2}} r^2 w_b(r)c_b(r)\left(T_a - T(r,t)\right)dr \tag{3.8}$$

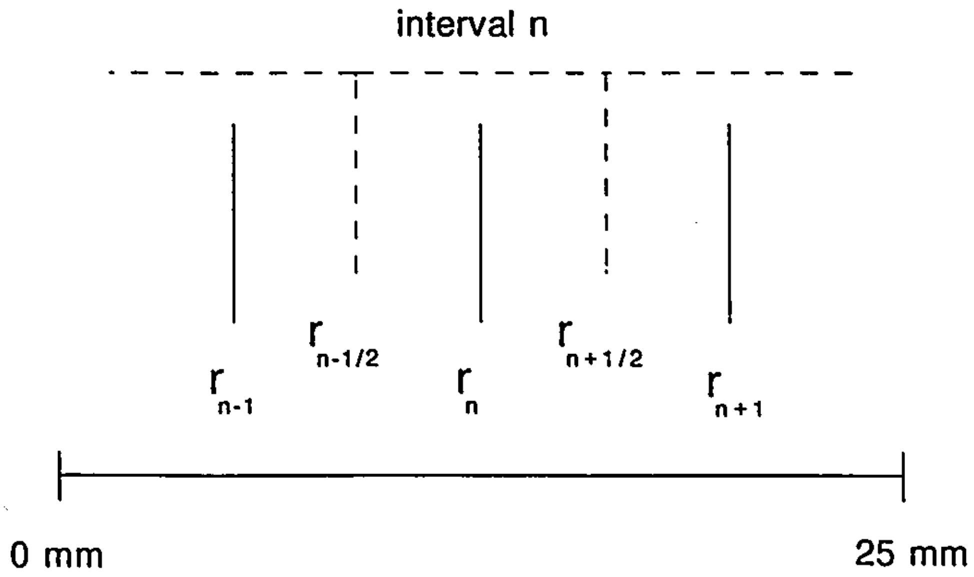

$$\frac{\partial T}{\partial r} = \frac{T(r+\Delta r,t) - T(r-\Delta r,t)}{2\Delta r} = \frac{T^s_{n+1} - T^s_{n-1}}{2\Delta r}$$

$$\frac{\partial^2 T}{\partial r^2} = \frac{T(r+\Delta r,t) - 2T(r,t) + T(r-\Delta r,t)}{\Delta r^2} = \frac{T^s_{n+1} - 2T^s_n + T^s_{n-1}}{\Delta r^2}$$

Figure 3.3 Finite differencing scheme.

where $r_{n\pm1/2} = 1/2(r_n + r_{n\pm1})$. Each time step in this transient problem involves solution of a static problem given that properties and sources are constant over the time interval. Time integration is handled by evaluating spatial derivatives at the beginning of a time interval which is valid if small time intervals (1-5 s) are used. The time derivative in (3.8) was approximated using the forward finite difference, $(T(t+\Delta t)-T(t))/\Delta t = (T_n^{s+1} - T_n^s)/\Delta t$. Larger time intervals may require averaging over the time step, as described by the Crank-Nicholson method (Becker 1986).

Solving the integrals in (3.7) and (3.8) results in difference expressions of the form

$$-\left[A_{n-1}\right]\phi_{n-1} + \left[A_{n+1} + A_{n-1} + \frac{\mu_{a_n}}{3}\left(r^3_{n+1/2} - r^3_{n-1/2}\right)\right]\phi_n - \left[A_{n+1}\right]\phi_{n+1} = S_n \tag{3.9}$$

$$\begin{aligned}\left[B_{n-1}\right] T^{s+1}_{n-1} - \left[B_{n+1} + B_{n-1} + \frac{1}{3}\left(\frac{\rho_n c_n}{\Delta t} + w_{b_n} c_{b_n}\right)\left(r^3_{n+1/2} - r^3_{n-1/2}\right)\right] T^{s+1}_n + \\ \left[B_{n+1}\right] T^{s+1}_{n+1} = -\frac{1}{3}\left(\mu_{a_n}\phi_n + w_{b_n} c_{b_n} T_a + \frac{\rho_n c_n T^s_n}{\Delta t}\right)\left(r^3_{n+1/2} - r^3_{n-1/2}\right)\end{aligned} \tag{3.10}$$

where the coefficients $A_{n\pm1}$ and $B_{n\pm1}$ are given by

$$A_{n\pm1} = \frac{2r^2_{n\pm1/2}}{\Delta r}\left[\frac{D_n D_{n\pm1}}{D_n + D_{n\pm1}}\right] \tag{3.11}$$

$$B_{n\pm1} = \frac{2r^2_{n\pm1/2}}{\Delta r}\left[\frac{k_{eff_n} k_{eff_{n\pm1}}}{k_{eff_n} + k_{eff_{n\pm1}}}\right] \tag{3.12}$$

In (3.9), $S_n = \phi_{point}/4\pi$ at $r = 0$ and $S_n = 0$ at $r > 0$. When $n = 0$, the tissue properties defined at "n-1" are set to zero. Thus the original differential equations are replaced by sets of simultaneous difference equations. The sets are tridiagonal which allows for easy solution even if the number of unknowns is large. At each time interval (3.9) and (3.10) are solved for ϕ_n and T_n^{s+1}, respectively, using Gaussian elimination with backward substitution.

3.2.3 2-D Inhomogeneous Tissues (Finite Element Solution)

The finite element method (FEM) is based on the concept of mathematically discretizing a region of a function into elements and using a simple interpolation procedure to generate a solution function. A comprehensive review of finite element analysis is given by Zienkiewicz and Taylor (1987). There is an advantage to using finite element formulations over finite differences when modelling inhomogeneous tissues. For clinically based applications, anatomical complexities characterized by irregular external and internal boundaries are accounted for in a general way in the basic finite element algorithm. However the algorithm is of greater complexity with potentially large matrix storage requirements.

In this section we develop a finite element model for solving the two coupled equations, (2.6) and (2.10), for a point optical source in an infinite 2-D inhomogeneous tissue medium. This 2-D application is equivalent to an infinite line optical source in an infinite 3-D medium. For a steady power, ϕ_{line} (W/cm), (2.6) and (2.10) are expressed in Cartesian coordinates

$$- \frac{\partial}{\partial x} D(x,y) \frac{\partial \phi(x,y)}{\partial x} - \frac{\partial}{\partial y} D(x,y) \frac{\partial \phi(x,y)}{\partial y} \\ + \mu_a(x,y)\phi(x,y) = \phi_{line}\, \delta(x,y) \tag{3.13}$$

$$\rho(x,y)c(x,y)\frac{\partial T(x,y,t)}{\partial t} = \frac{\partial}{\partial x} k_{eff}(x,y) \frac{\partial T(x,y,t)}{\partial x} + \frac{\partial}{\partial y} k_{eff}(x,y) \frac{\partial T(x,y,t)}{\partial y} + \\ w_b(x,y)c_b(x,y)\left(T_a - T(x,y,t)\right) + \mu_a(x,y)\phi(x,y) \tag{3.14}$$

where δ(x,y) is the 2-D Dirac delta (cm^{-2}).

The two most common procedures for generating finite element solutions are variational methods (Rayleigh-Ritz) and weighted-residual methods. We employ the weighted residuals method which has been used extensively to solve both optical propagation and thermal propagation models. An approximate solution to (3.14) is generated by minimizing the integral over the domain, A, of the assumed solution in the differential equation (minimization of the residual). This is expressed mathematically as

$$\int_A \omega(x,y) \left[\left(\frac{\partial}{\partial x} k_{eff} \frac{\partial}{\partial x} + \frac{\partial}{\partial y} k_{eff} \frac{\partial}{\partial y} - w_b c_b - \rho c \frac{\partial}{\partial t} \right) T(x,y,t) + \\ \mu_a(x,y)\phi(x,y) + w_b c_b T_a \right] dA = 0 \tag{3.15}$$

where ω (x,y) is a suitable vector of weighting functions which satisfy the same boundary conditions as T.

For 2-D problems the simplest form of discretizing the tissue is triangulation (see figure 3.4). The temperature, T(x,y,t), in (3.15) is defined as an expansion in terms of spatially varying basis functions and nodal temperature values. We assume that the temperature within each triangular element (e) is well represented by the piece-wise linear interpolation function

$$T^{(e)}(x,y,t) = \sum_{i=1}^{3} \alpha_i^{(e)}(x,y)T_i^{(e)}(t) \tag{3.16}$$

where $T_i^{(e)}(t)$ and $\alpha_i^{(e)}(x,y)$ are the temperature and linear interpolation ("shape") function at node i in element (e)

$$\alpha_i^{(e)}(x,y) = a_i + b_i x + c_i y \tag{3.17}$$

with the coefficients a_i, b_i and c_i being nondimensional functions of the nodal coordinates of element (e). The shape functions given by (3.17) are zero at all points in A except those of element (e) and have a value of 1 at node i and values of 0 at nodes $j \neq i$. The accuracy of the assumed solution given by (3.16) and (3.17) depends on the behaviour of the solution of the differential equation in element (e).

An accurate form of the weight residuals method is Galerkin's method where the weight function, $\omega_i(x,y)$, is of the same form as the interpolation function, $\alpha_i(x,y)$. Substituting the temperature expansion, (3.16), into (3.15) for all NN nodes in the spatially discretized domain A yields

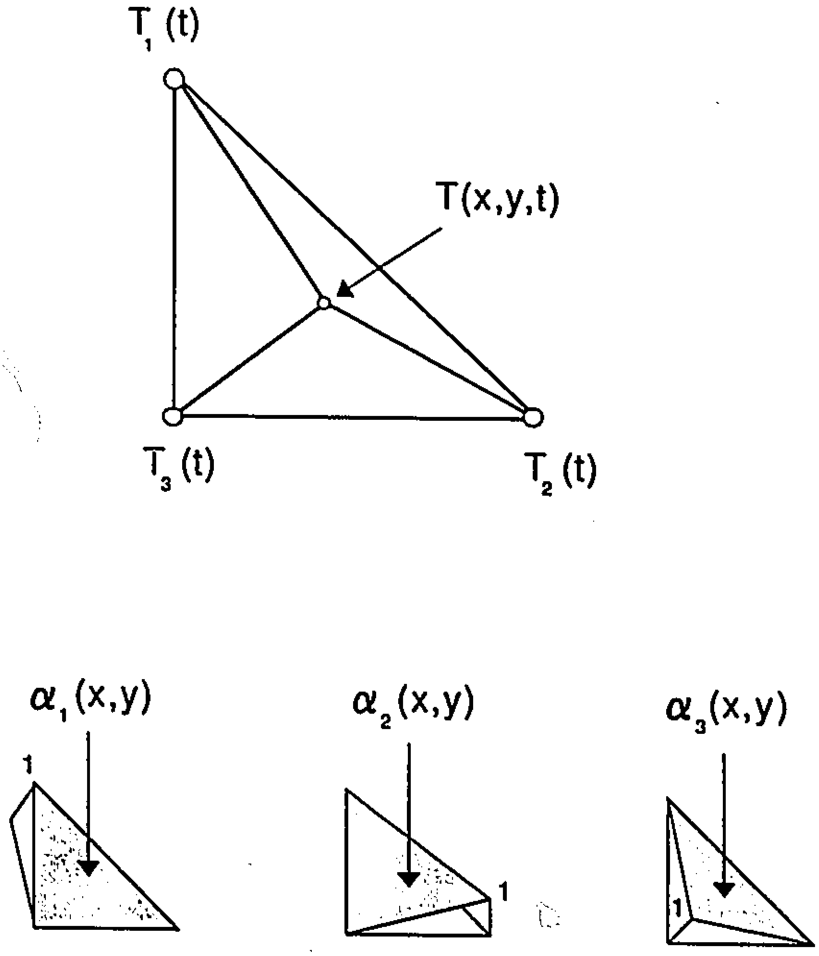

Figure 3.4. Triangular element, (e), with nodal temperatures and associated shape functions.

$$\int_A \alpha_j(x,y)\left[\left(\frac{\partial}{\partial x}k_{eff}\frac{\partial}{\partial x} + \frac{\partial}{\partial y}k_{eff}\frac{\partial}{\partial y} - w_b c_b - \rho c\frac{\partial}{\partial t}\right)\sum_{i=1}^{NN}\alpha_i(x,y)T_i + \mu_a\phi(x,y) + w_b c_b T_a\right] dA = 0 \qquad for\ j = 1\ to\ NN \tag{3.18}$$

For constant k_{eff} within an element the second derivatives in (3.18) are zero. This problem is avoided by integrating the second order terms in (3.18) by parts and employing Green's Theorem (Arfken 1985). The resulting finite element formulation is known as the weak formulation of the problem and is expressed in matrix form as

$$[K + W]T + C\frac{\partial T}{\partial t} = Q + \Gamma \tag{3.19}$$

where

$$T = \left[T_1(t), T_2(t), ..., T_{NN}(t)\right]^T \tag{3.20}$$

$$K_{i,j} = \int_A k_{eff}\left[\frac{\partial\alpha_j(x,y)}{\partial x}\frac{\partial\alpha_i(x,y)}{\partial x} + \frac{\partial\alpha_j(x,y)}{\partial y}\frac{\partial\alpha_i(x,y)}{\partial y}\right] dA \tag{3.21}$$

$$W_{i,j} = \int_A \alpha_j(x,y)\alpha_i(x,y) w_b c_b dA \tag{3.22}$$

$$C_{i,j} = \int_A \alpha_j(x,y)\alpha_i(x,y)\rho c dA \tag{3.23}$$

$$Q_i = \int_A \alpha_i(x,y) \left[\mu_a(x,y)\phi(x,y) + w_b c_b T_a\right] dA \tag{3.24}$$

$$\Gamma_i = \oint_{\partial A} \alpha_i(x,y) k_{eff} \left(\frac{\partial T(x',y',t)}{\partial x} n_x + \frac{\partial T(x',y',t)}{\partial y} n_y \right) d(\partial A) \tag{3.25}$$

where n_x and n_y are unit vectors on the boundary ∂A. The line integral, Γ_i, describes the boundary conditions and will be nonzero only for points (x',y') on ∂A.

The standard method for handling the temporal variation is to use a finite difference scheme to integrate (3.19) over a time interval s → s+1

$$[K + W]\int_{t_s}^{t_{s+1}} T dt + C\int_{t_s}^{t_{s+1}} \frac{\partial T}{\partial t} dt = \int_{t_s}^{t_{s+1}} [Q + \Gamma] dt \tag{3.26}$$

The time differential is approximated by a forward finite difference at s and a backward finite difference at s+1

$$\frac{\partial T^s}{\partial t} = \frac{\partial T^{s+1}}{\partial t} = \frac{T^{s+1} - T^s}{\Delta t} \tag{3.27}$$

Each time step in this transient problem involves solution of a static problem given that properties and sources are assumed to be constant over the time interval. Assuming a weighted trapezoidal integration rule for (3.26) we obtain (Zienkiewicz and Taylor 1987)

$$\left[\theta K + \theta W + \frac{1}{\Delta t}C\right]\Gamma^{s+1} + \left[(1-\theta)K + (1-\theta)W - \frac{1}{\Delta t}C\right]\Gamma^{s} = \theta\left(Q^{s+1} + \Gamma^{s+1}\right) + (1-\theta)\left(Q^{s} + \Gamma^{s}\right) \tag{3.28}$$

where the time weighting parameter, θ, controls the finite difference approximation of the time interval. Values of θ can range from 0 (explicit scheme) to 1.0 (implicit scheme) with an intermediate value 0.5 known as the Crank-Nicholson scheme. Values of θ = 0.5 - 1.0 result in unconditionally stable algorithms.

The same finite element formalism was used to generate an approximate solution to the time-independent diffusion equation, (3.13), for an isotropic point source at (x',y'). The resulting finite element " weak" formulation is expressed in matrix form as

$$[D + U]\phi = S + \Gamma' \tag{3.29}$$

where

$$\phi = \left[\phi_1, \phi_2, \ldots, \phi_{NN}\right]^T \tag{3.30}$$

$$D_{i,j} = \int_A D\left[\frac{\partial\alpha_j(x,y)}{\partial x}\frac{\partial\alpha_i(x,y)}{\partial x} + \frac{\partial\alpha_j(x,y)}{\partial y}\frac{\partial\alpha_i(x,y)}{\partial y}\right]dA \tag{3.31}$$

$$U_{i,j} = \int_A \alpha_j(x,y)\alpha_i(x,y)\mu_a dA \tag{3.32}$$

$$S_j = \int_A \alpha_j(x,y)\ \phi_{line}\delta(x-x',y-y')dA \tag{3.33}$$

$$\Gamma_i' = \oint_{\partial A} \alpha_i(x,y) D \left(\frac{\partial \phi(x',y')}{\partial x} n_x + \frac{\partial \phi(x',y')}{\partial y} n_y \right) d(\partial A) \qquad (3.34)$$

The set of 3 by 3 element matrices $\mathbf{K}^{(e)}$, $\mathbf{W}^{(e)}$, $\mathbf{C}^{(e)}$, $\mathbf{D}^{(e)}$ and $\mathbf{U}^{(e)}$ is generated for each element by carrying out the integrations in (3.21)-(3.25) and (3.31)-(3.34) over the elemental area, $A^{(e)}$. The thermophysical and optical properties values are assigned to each element and are, therefore, incorporated as coefficients in the element matrices. The element matrices are assembled into global matrices of order NN by NN. The global matrices are sparse and have nonzero entries only when α_i and α_j are nodes of the same element. The global matrices are symmetric and diagonally banded of width WD. The node numbers are ordered so as to minimize WD. The original global matrices can then be replaced with WD by NN matrices, reducing storage requirements.

The set of 1 by 3 element matrices $\mathbf{Q}^{(e)}$ and $\mathbf{S}^{(e)}$ are assembled into global matrices of order 1 by NN. Generally, S_j is nonzero only when j is a node of the element containing the source. In our application, the source is at the origin, (x=0,y=0), which corresponds to a node common to four surrounding elements. Evaluation of (3.33) yields $S_j=\alpha_j(0,0)\phi_{line}$. Therefore, in generating the matrices, $\mathbf{S}^{(e)}$, for the four elements surrounding the origin, 1/4 of the total optical line power is used for the origin node in each of the four element matrix evaluations.

We assume the Dirichlet condition at the boundary ∂A, $T(\partial A,t)=0$ and $\phi(\partial A)=0$, which implies that Γ and Γ' in (3.19) and (3.29), respectively, are zero.

This is achieved by adding a large factor (10^3 was used) to the diagonal elements of **K**, **W**, **C**, **D** and **U** for the boundary nodes, a technique known as the Paynes-Iron method (Zienkiewicz and Taylor 1987).

A 2-D square mesh of equally sized triangular elements was generated. A high resolution mesh, corresponding to a node spacing of 1 mm, is shown in Fig. 3.5. Eqs. (3.28) and (3.29) are solved for $\mathbf{T}^{s+1}$ and ϕ, respectively, using Gaussian elimination, with forward and back substitution, for bandwidth reduced matrices. All nodes in the mesh are fixed (inelastic tissue medium).

3.3 Modelling of Phase Changes during Interstitial Laser Photocoagulation

To model ILP accurately, important optical and thermal events should be considered in the physical description of tissue heating. As tissues are heated to beyond approximately 60°C, they appear "whitish" due to protein denaturation (coagulation). Splinter et al. (1991) reported that *ex vivo* coagulated canine myocardium had a reduced scattering coefficient two to three times greater than normal canine myocardium at 1064 nm, whereas the absorption coefficient was unaffected by coagulation. Pickering et al. (1994) reported a twofold increase in the reduced scattering coefficient of *ex vivo* rat liver, at 1064 nm, heated from 23°C to 60°C. Jaywant et al. (1993) reported a sixfold increase in the reduced scattering coefficient of *ex vivo* bovine muscle, at 810 nm, heated from 30°C to 70°C, whereas the absorption coefficient decreased only slightly. In our description of ILP, tissue coagulation is modelled as a step increase in the reduced scattering coefficient in

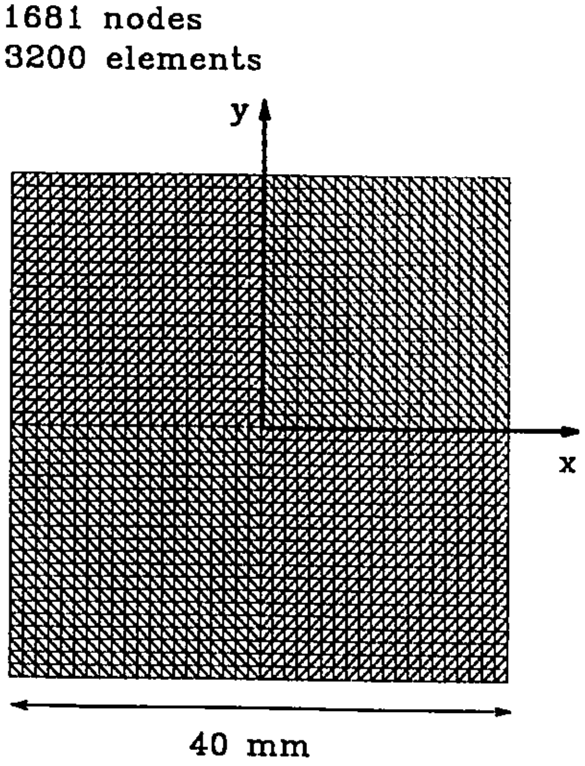

Figure 3.5 2-D square grid mesh used to generate finite element solutions to (3.29) and (3.28).

tissues where the predicted temperature exceeds a 60°C threshold. Empirical data suggest that tissues elevated to 60°C coagulate within a few seconds (McKenzie 1990). Therefore, it is assumed that coagulation is instantaneous at 60°C.

It has been reported by Duck (1990) that k, c and ρ for soft tissues remain quasi-constant at temperatures below 100°C. Above 100°C, modifications of the thermophysical properties due to vaporization of tissue water are not well determined, although water loss may reduce the thermal conductivity (Thomsen 1991, Spells 1960) and specific heat of tissues (Thomsen 1991). Equation (2.12) suggests that the thermal conductivity and specific heat are directly proportional to the mass fraction of water and would, therefore, decrease as tissue water is vaporized at temperatures above 100°C. The rate of vaporization of tissue water during interstitial laser irradiation is not clearly determined. In our description of ILP, vaporization is modelled as an instantaneous and complete loss of water in tissues where the predicted temperature exceeds a 100°C threshold. The thermal conductivity, specific heat and density in the vaporized zone are approximated using (2.12), assuming that the residual material is composed of 50% fat and 50% protein. Activation energies for these phase transitions (coagulation and vaporization) are discussed in Results (Chapter 4).

3.4 Modelling *In Vivo* ILP in Liver

Transient temperature distributions during *in vivo* ILP in liver were predicted by solving the 1D inhomogeneous finite difference expressions for irradiance and temperature given by (3.9) and (3.10), respectively, for the Pennes description (k_{eff} = k in (2.10) and (3.12)). The influence on temperature distributions of increased blood perfusion and coagulation-induced increases in optical scattering is assessed. Total laser power and irradiation time were chosen to keep the maximum tissue temperature below 100°C, a desirable clinical result, reducing the potential for tissue charring.

Tissue coagulation was modelled as a step increase in μ_s' extending from the source, at $r = 0$, to R_{coag}, the nearest "$r_{n+1/2}$" radial distance corresponding to a model-predicted temperature of 60°C. The values for R_{coag} were updated at each Δt interval during transient temperature calculations. The effect of different step increases in μ_s' on model-predicted temperatures was assessed. The tissue properties, k, c, ρ and μ_a remain at their initial values during transient temperature calculations. The extent of thermal necrosis is approximated using (2.15).

3.5 Modelling Tissue Charring/Browning: Estimating Charring Temperature

During ILP, temperature measurements from implanted sensors such as microthermocouples generally contain errors arising from thermal conduction smearing, averaging over the finite sensor volume, and uncertainty in sensor location (typically ± 1 mm). Near the source, large temperature gradients (typically 100-500°C/mm) potentiate all 3 types of error. Temperature measurements can thus be highly inaccurate.

In this work, the strategy for determining T_{char} involved measuring temperatures during ILP, but avoiding large measurement errors by extracting only the *times* at which temperature-time profiles displayed certain interesting changes (discussed later). These times were used to guide mathematical modelling calculations of temperature. The temperature at the periphery of any char region, presumably T_{char}, was estimated at the time of beam off by placing observed charring dimensions on calculated temperature-distance profiles after illumination.

The ILP was performed *ex vivo* in lean bovine muscle by delivering 1.50 ± 0.05 W of continuous-wave 1064 nm Nd:YAG or 800 nm diode laser energy from a 400 μm core diameter, plane-cut optical fiber. Tissue phantom preparation and microthermocouple array and optical fiber positioning were described in section 3.1. Experiments were repeated at each optical wavelength.

The model for tissue charring presented here differs fundamentally from that of McKenzie (1986), who assumed that charring occurred at 100°C. In highly scattering tissues, such as bovine muscle, a plane-cut fiber tip is accurately approximated as being a point isotropic source. Therefore, optical distributions during *ex vivo* ILP in bovine muscle were determined by solving the 1-D inhomogeneous finite difference expression for irradiance given by (3.9). During ILP, tissue charring increases optical absorption, converting the point optical source into effectively a point heat source for the remainder of the exposure (Wyman et al. 1992). This is modelled as a transient change in the spatial energy deposition, Q_s in (2.10), expressed as a weighted interpolation, $\omega(t)$, between energy deposition from a point optical source, $Q_{optical}(r)$, and a point heat (charring) source, $Q_{heat}(r)$

$$Q_S(r,t) = \omega(t)Q_{optical}(r) + [1-\omega(t)]Q_{heat}(r) \tag{3.35}$$

where

$$Q_{optical}(r) = \mu_a(r)\phi(r), \qquad Q_{heat}(r) = \phi_{point}\delta(r) \tag{3.36}$$

and $\delta(r)$ is the 3-dimensional Dirac delta (cm^{-3}).

Transient temperature distributions were predicted by solving the 1D inhomogeneous finite difference expression for temperature, as derived in section 3.3.2 with modification to the source given by (3.35) and (3.36)

$$\begin{aligned}\left[B_{n-1}\right] T^{s+1}_{n-1} - \left[B_{n+1} + B_{n-1} + \frac{1}{3}\left(\frac{\rho_n c_n}{\Delta t} + w_{b_n} c_{b_n}\right)\left(r^3_{n+1/2} - r^3_{n-1/2}\right)\right] T^{s+1}_n + \\ \left[B_{n+1}\right] T^{s+1}_{n+1} = -\frac{1}{3}\left(\omega(t)\mu_{a_n}\phi_n + w_{b_n} c_{b_n} T_a + \frac{\rho_n c_n T^s_n}{\Delta t}\right)\left(r^3_{n+1/2} - r^3_{n-1/2}\right) - (1 - \omega(t))S_n\end{aligned} \tag{3.37}$$

In this work, two separate descriptions of tissue charring are presented. The first description assumes a sudden onset of opaque char at time t_c, so that

$$\omega(t) = \begin{cases} 1 & , \quad t < t_c \\ 0 & , \quad t_c \le t \end{cases} \tag{3.38}$$

The second description is a continuously progressive and variable "browning" process with browning commencing at time t_b and culminating in opaque char at time t_c. This continuous browning model is consistent with gross observations of carmelization (Thomsen 1991) and temperature changes observed in this study (see Chapter 4, section 4.2). According to this model,

$$\omega(t) = \begin{cases} 1 \quad , \quad t < t_b \\ \dfrac{(t_c - t)}{(t_c - t_b)} \quad , \quad t_b \leq t \leq t_c \\ 0 \quad , \quad t_c < t \end{cases} \tag{3.39}$$

Prior to browning, Q_S is strictly optical. After opaque char is attained, Q_S is a point heat source. In each description of tissue charring, the total power, ϕ_{point}, remains constant. The weighting functions given by (3.38) and (3.39) act to distribute ϕ_{point} between point optical and point heat sources at r=0.

Tissue coagulation was modelled as a twofold step increase in μ_s' extending from the source, at r = 0, to a radial distance R_{coag}, where the model-predicted temperature is 60°C. The effect of different step increases in μ_s' on the model-predicted charring temperature, T_{char}, was also assessed.

Tissue vaporization was modelled as a step decrease in the thermophysical properties extending from the source, at r = 0, to a radial distance R_{vapr}, where the model-predicted temperature is 100°C. Values for R_{coag} and R_{vapr} were set to the nearest "$r_{n+1/2}$" radial distances corresponding to temperatures of 60°C and 100°C, respectively, and were updated at each 1 s interval during transient temperature calculations.

The temperature profiles measured *ex vivo* were used as timers for the onset of browning and/or charring (both descriptions of charring were used). In any profile, sudden nonspurious temperature increases reported by a microthermocouple were taken as indicating t_b or t_c for that profile, to be used in the calculational model. As described above, T_{char} was estimated by placing observed charring dimensions post-illumination on calculated profiles. Uncertainty in T_{char} was estimated from the variation in T_{char} values derived from different experiments and using different descriptions of charring (continuous browning, sudden charring).

3.6 Temperature Reconstruction Algorithm

The parameter estimation formalism in section 2.4 was used to test the feasibility of multiple-parameter estimation in laser heated tissues and gain insight into some of the practical limitations of this inverse problem. Computer simulations of interstitial laser heating were used to generate the input temperature data because they provided a controllable set of known tissue parameters and complete true temperature profiles, difficult to obtain experimentally.

Depending on the spatial distribution of biophysical properties to be modelled, both forward and inverse simulations of ILP were determined using either the quasi-analytical, finite difference or finite element solutions described in section 3.3. In each simulation, measured temperature data were generated using the same thermal and optical models utilized in the parameter estimation algorithm. In all applications the WJ Model (w_b=0 in (3.6) and (3.14)) was used based solely on its reduced number of required tissue parameters compared to the Pennes model. The number of unknowns was further reduced by lumping ρ and c into a volumetric heat capacity, $c_v=\rho c$. Thus, optical and temperature distributions depend on 4 fundamental tissue parameters: k_{eff}, c_v, μ_a and μ_s'.

Equation (2.32) forms the basis of the iterative temperature reconstruction algorithm summarized in Fig. 3.6. The algorithm begins with an initial homogeneous guess parameter vector and a λ of 0.001. The objective functional, F, is evaluated and new parameter estimates determined using (2.32). A negative parameter estimate or failure to reduce F prompts an order of magnitude increase in λ and then re-estimation of parameters (Levenberg-Marquardt regularization loop). If F was reduced the iterative estimates were accepted and the process continued until the following convergence criteria were both met (Gill et al. 1993)

$$\text{C1.}\quad |F^{\xi+1} - F^{\xi}| < \tau\,(1 + |F^{\xi}|) \tag{3.40}$$

$$\text{C2.}\quad \|\mathbf{P}^{\xi+1} - \mathbf{P}^{\xi}\| < \sqrt{\tau}\,(1 + \|\mathbf{P}^{\xi}\|)$$

where τ determines the number of correct digits desired in F ($\tau = 10^{-3}$). For small N, the Euclidean norm is used to evaluated C2. For well-scaled problems, satisfying C1 implies satisfying C2. For ill-conditioned problems, failure to meet C2 indicates some or all of the parameter increments are still relatively large. Once F was minimized, the parameter estimates were then used to solve the direct forward problem for temperatures at all points in the thermal field.

All simulations were performed on a VAX 4400, in double precision,

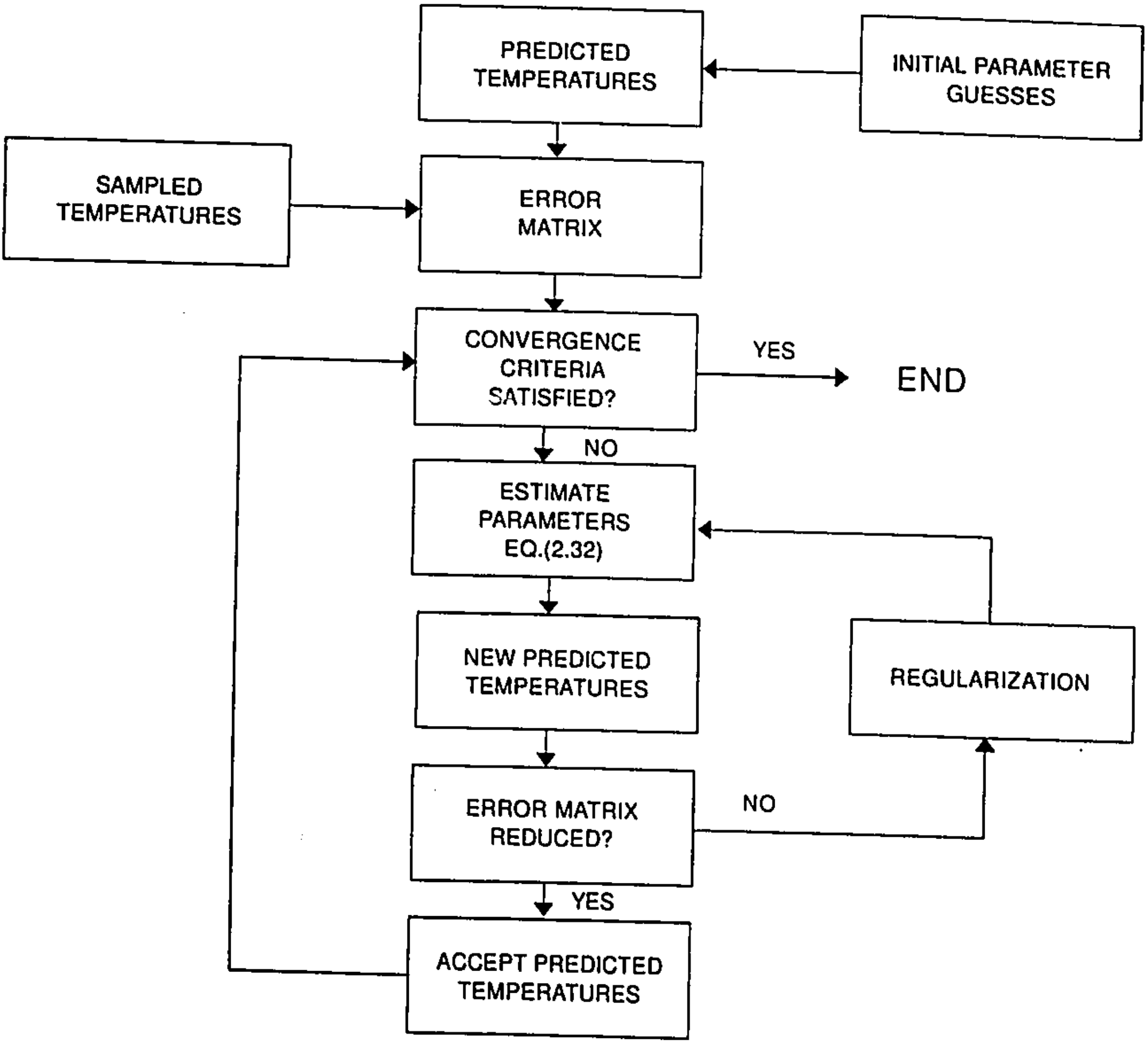

Figure 3.6. Iterative temperature reconstruction algorithm.

utilizing an Internal Mathematical Subroutine Library (IMSL) routine, based on QR factorization (Gill et al. 1993), to solve the inverse $(J^TJ + \lambda I)^{-1}$ from (2.32).

For minimally invasive clinical treatments, maximizing the temperature information may require the use of microthermocouple arrays (Gerig et al. 1992, Anhalt and Hynynen 1992). In all reconstructions simulated temperature sensors were in a linear array. Temperature measurement data depended on array design, characterized by the number of sensors (M) and spacing between sensors, and on array-source distance. S is the number of times a sensor is sampled per reconstruction interval, Δt_{rec}. The biophysical parameters were estimated and complete temperature distributions reconstructed at user defined reconstruction intervals during simulated treatments. The transient temperature reconstruction scheme is shown in Fig. 3.7.

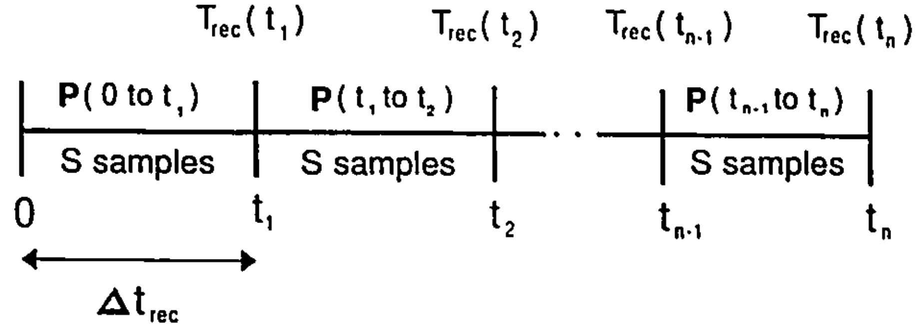

Figure 3.7 Transient temperature reconstruction scheme. Sensors are sampled during the interval, Δt_{rec}, and input into the temperature reconstruction algorithm for estimation of **P** for the interval. $T_{rec}(t)$ represents the reconstructed temperature profile at the end of the interval.

CHAPTER 4. Results

4.1 *In Vivo* ILP Simulations in Liver

Single fiber ILP at 1064 nm in normal liver was simulated. The thermophysical properties and blood perfusion rate of normal human liver, used in the calculational model, are shown in Table 4.1. The optical properties for human liver at 1064 nm are not available in the literature. Optical properties of normal bovine liver at 1064 nm were used, and are shown in Table 4.1. The finite difference solutions for a sphere of radius 30 mm with 0.1 mm node spacing and a 5 s temporal step agreed exactly with the analytical solution for an isotropic point optical source in an infinite homogeneous medium given by (3.4) (see Fig 4.1). This agreement provides the basis for using finite difference solutions for generating optical and temperature distributions in this thesis. The effects of blood perfusion patterns and coagulation-induced increases in the reduced scattering coefficient on temperature profiles were assessed.

Given the range of experimentally measured coagulation-induced increases in scattering reported in the literature, a parametric assessment was undertaken in which the reduced scattering coefficient for coagulated liver, $(\mu_s')_{coag}$, is approximated as either a 2, 4 or 6 fold increase in the reduced scattering coefficient for normal liver, $(\mu_s')_{norm}$.

Table 4.1. Thermophysical and blood perfusion properties (Duck 1990) and optical properties (Cheong et al. 1990) used in the calculational model.

Tissue Thermal Conductivity (human liver)	0.00520 W/cm/°C
Specific Heat of Tissue (human liver)	3.60 J/g/°C
Tissue Density (human liver)	1.06 g/cm^3
Blood Perfusion Rate (human liver)	100 ± 90 ml/100 g/min
Specific Heat of Blood	3.84 J/g/°C
Blood Density	1.06 g/cm^3
Absorption Coefficient (bovine liver)	0.53 cm^{-1}
Reduced Scattering Coefficient (bovine liver)	1.76 cm^{-1}

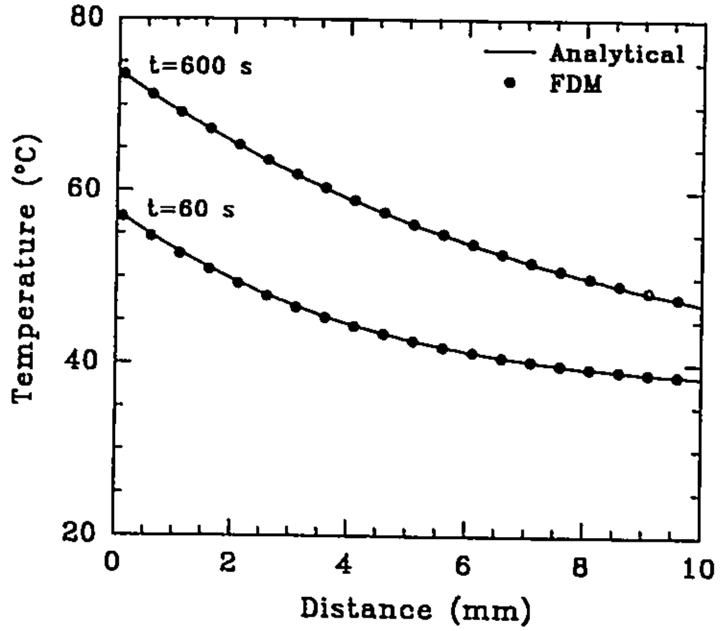

Figure 4.1. Homogeneous sphere of radius 30 mm, with biophysical properties from Table 4.1. Analytical calculations (Eq.(3.4)) and finite difference calculations with Δr=0.1 mm and a time step of 5 s are plotted. Finite difference solutions were constant over the ranges Δr=0.1-0.25 mm and Δt=1-5 s.

The calculated thermal history at a radial distance of 1 mm from the source, for a 600 s irradiation of 3 W, is shown in Fig. 4.2(a). A uniform perfusion rate of 100 ml/100 g/min was used in calculating temperatures. Transient temperature profiles are identical prior to the predicted time of onset of coagulation, ~ 70 s. At t > 70 s, temperatures increase nonlinearly with increasing $(\mu_s')_{coag}$. However, the thermal histories for a constant and a twofold increase in the reduced scattering coefficient are similar. Thermal equilibrium is reached early in the irradiation, ~ 100 s for the homogeneous case $(\mu_s')_{coag}=(\mu_s')_{norm}$, and is delayed with increasing $(\mu_s')_{coag}$.

Radial temperature profiles at the end of the irradiation are shown in Fig. 4.2(b). The maximum tissue temperature increases by ~ 4°C, 17°C and 47°C for $(\mu_s')_{coag}/(\mu_s')_{norm}$ of 2, 4 and 6, respectively. Fig. 4.2(b) shows that increasing $(\mu_s')_{coag}$ affects negligibly temperatures at points beyond ~ 2 mm from the predicted coagulation boundary, 60°C. This suggests that in order to detect the presence of coagulation in highly perfused liver using on-line thermometry, a sensor must be within ~ 2 mm of the coagulation boundary.

The temperature differences observed in Fig. 4.2 are a result of differing energy deposition patterns. The predicted coagulation diameter as a function of time and $(\mu_s')_{coag}$, is shown in Fig. 4.3(a). It should be restated that R_{coag} determines the radial extent of the increase in the reduced scattering coefficient. Prior to the onset of coagulation, R_{coag} is zero. At 70 s the model-predicted temperature at the first radial node, r=0.01 cm, has exceeded 60 °C. For t > 70 s, the time rate of

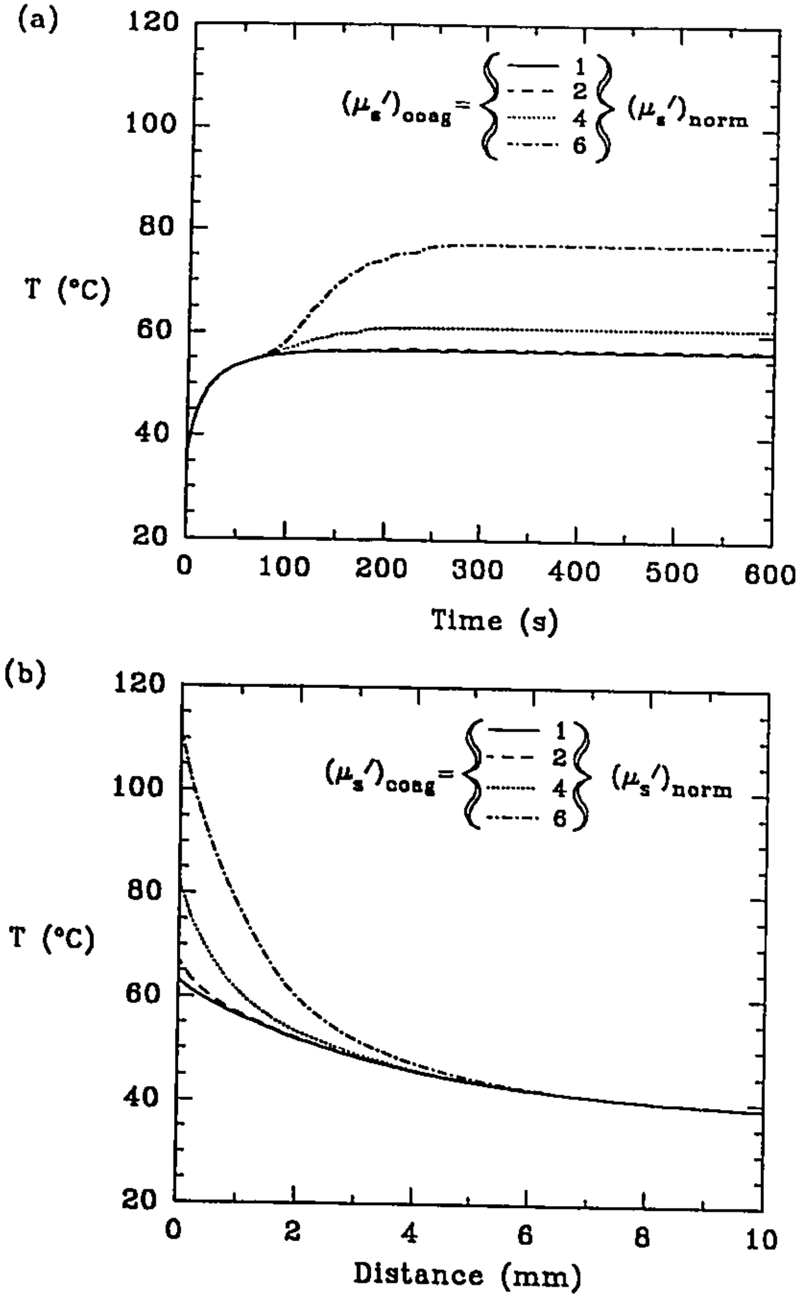

Figure 4.2. Effect of coagulation induced increases in the reduced scattering coefficient on the temperature distributions in liver for a 600 s irradiation at 3 W. (a) Calculated thermal history at 1 mm from the source. (b) Calculated radial temperatures at 600 s. A uniform perfusion rate of 100 ml/100 g/min was used in calculating these results.

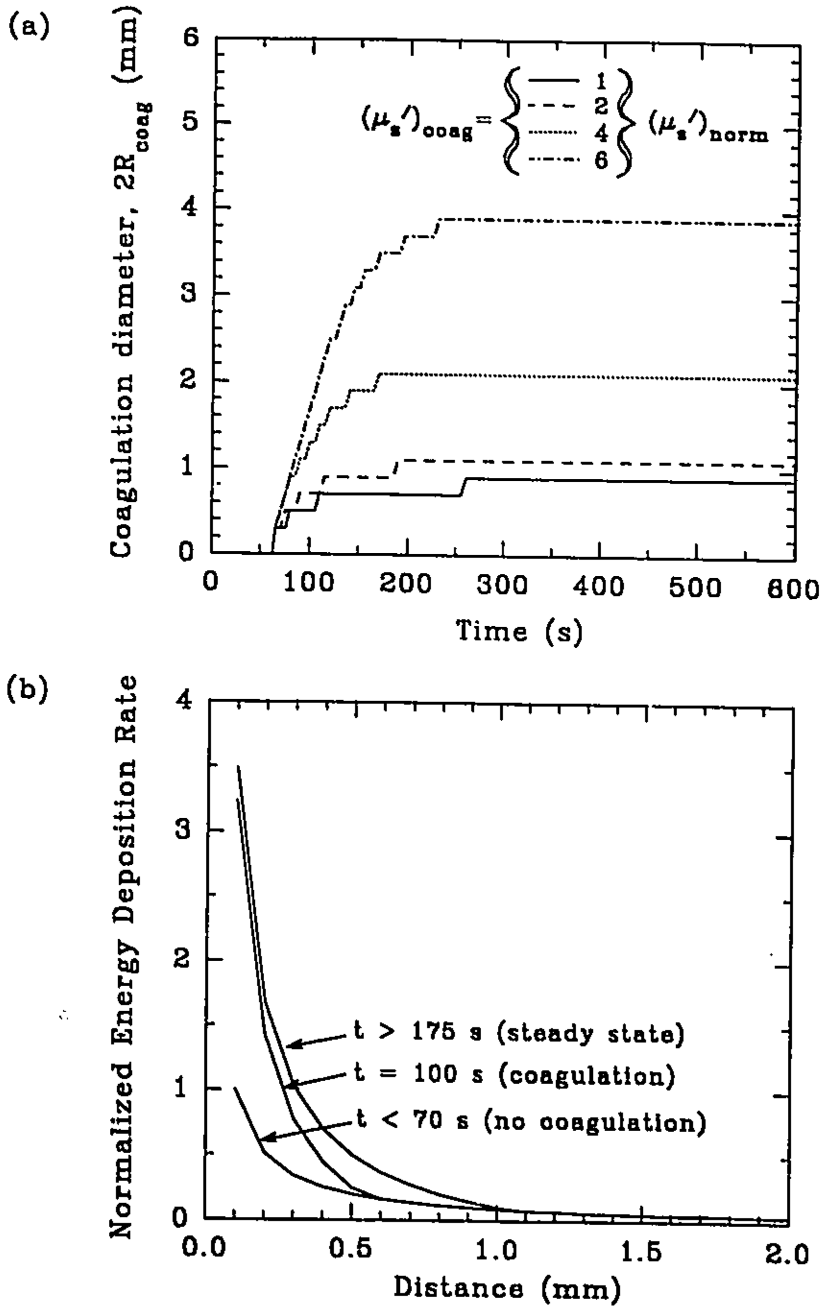

Figure 4.3. (a) Predicted coagulation diameter in liver as a function of $(\mu_s')_{coag}$ for the simulations in Fig. 4.2. (b) Energy deposition rate as a function of irradiation time for the $(\mu_s')_{coag} = 4(\mu_s')_{norm}$ simulation in Fig. 4.2. The energy deposition rate is normalized to the maximum value for the homogeneous case, $(\mu_s')_{coag} = (\mu_s')_{norm}$.

increase in the coagulation diameter depends greatly on the value of $(\mu_s')_{coag}$. At 600 s, the model-predicted coagulation diameter is 0.95 mm, 1.15 mm, 2.15 mm and 3.95 mm for $(\mu_s')_{coag}/(\mu_s')_{norm}$ of 1, 2, 4 and 6, respectively.

Calculated radial energy deposition profiles for $(\mu_s')_{coag} = 4(\mu_s')_{norm}$ as a function of irradiation time are shown in Fig. 4.3(b). Energy deposition is normalized to the maximum value for the homogeneous case $(\mu_s')_{coag} = (\mu_s')_{norm}$, prior to the onset of coagulation, $t < 70$ s. Fig. 4.3(b) shows that coagulation leads to a broadening of the irradiance distribution. For $t > 70$ s, energy deposition inside the expanding coagulation radius increases, inducing higher temperatures, which in turn further increases the coagulation zone, as observed in Fig. 4.3(a). Since all photons emitted by the source are absorbed somewhere, the spatial integral of $\mu_a\phi(r)$ must be equal to ϕ_{point} for all $(\mu_s')_{coag}$ modelled. Therefore an increase in the irradiance near the source is accompanied by a decrease away from the source. This was measured by Matthewson et al. (1987) as a decrease in light transmission in rat liver during single fiber ILP.

Figs. 4.2 and 4.3 indicate that, in the absence of vaporization and charring, coagulation-induced increases in scattering in liver affect temperatures substantially and should be considered when modelling ILP. However if temperatures exceed 100 °C, vaporization and charring are likely to occur and tissue temperatures are no longer influenced by optical scattering.

The effect of blood perfusion on temperature distributions, for a 600 s irradiation at 2.5 W, is shown in Fig. 4.4. It was assumed that the blood perfusion

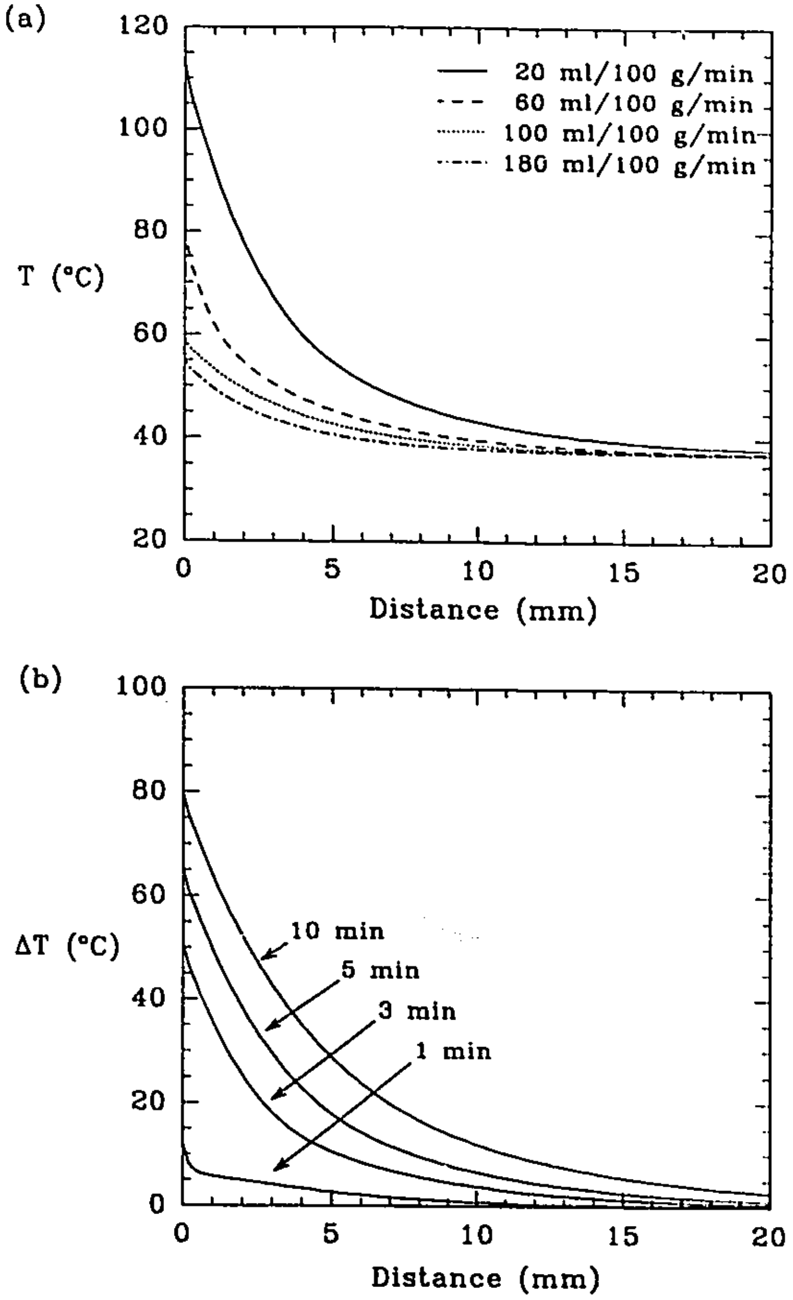

Figure 4.4. Effect of uniform blood perfusion on the temperature distributions in liver for a 600 s irradiation at 2.5 W assuming $(\mu_s')_{coag} = 4(\mu_s')_{normal}$. (a) Calculated radial temperatures at 600 s as a function of perfusion rate. (b) Differences in radial temperatures for no perfusion and for a perfusion rate of 100 ml/100 g/min as a function of irradiation time.

was uniform and $(\mu_s')_{coag} = 4(\mu_s')_{norm}$. It is observed in Fig. 4.4(a) that increased blood perfusion reduces radial temperature profiles. The difference in predicted temperature profiles over the range of uncertainty for the blood perfusion rate suggests that pretreatment calculations may prove useful only in cases when the perfusion rate has been measured. Fig. 4.4(a) also shows that the temperature sensitivity to perfusion, dT/dw_b, decreases with increasing perfusion. For $w_b \geq$ 100 ml/100 g/min, the maximum tissue temperature remains below the threshold for coagulation. Increasing the perfusion rate from 100 ml/100 g/min to 180 ml/100 g/min influences minimally the temperature profile.

The difference in calculated temperatures between perfused (w_b = 100 ml/100 g/min) and non-perfused liver is shown in Fig. 4.4(b) and indicates that the cooling effect of blood perfusion is more pronounced at longer irradiation times. The model predicts that coagulation, with its associated increase in optical scattering, is induced only for the non-perfused case. The curves in Fig. 4.4(b) thus differ in shape from those reported by Anvari et al. (1994b) for homogeneous scattering.

The results presented so far assume uniform perfusion which is an approximation of real tissue behaviour. We consider two additional approximations described in Fig. 4.5. In the tumor perfusion model (Divrik et al. 1984), we consider a idealized spherical tumor of radius, R_{tumor}, characterized by a central non-perfused core, $r \leq R_{core}$, surrounded by a zone of intermediate perfusion, $R_{core} < r \leq R_{int}$, and maximal perfusion at the periphery, $R_{int} < r \leq R_{tumor}$.

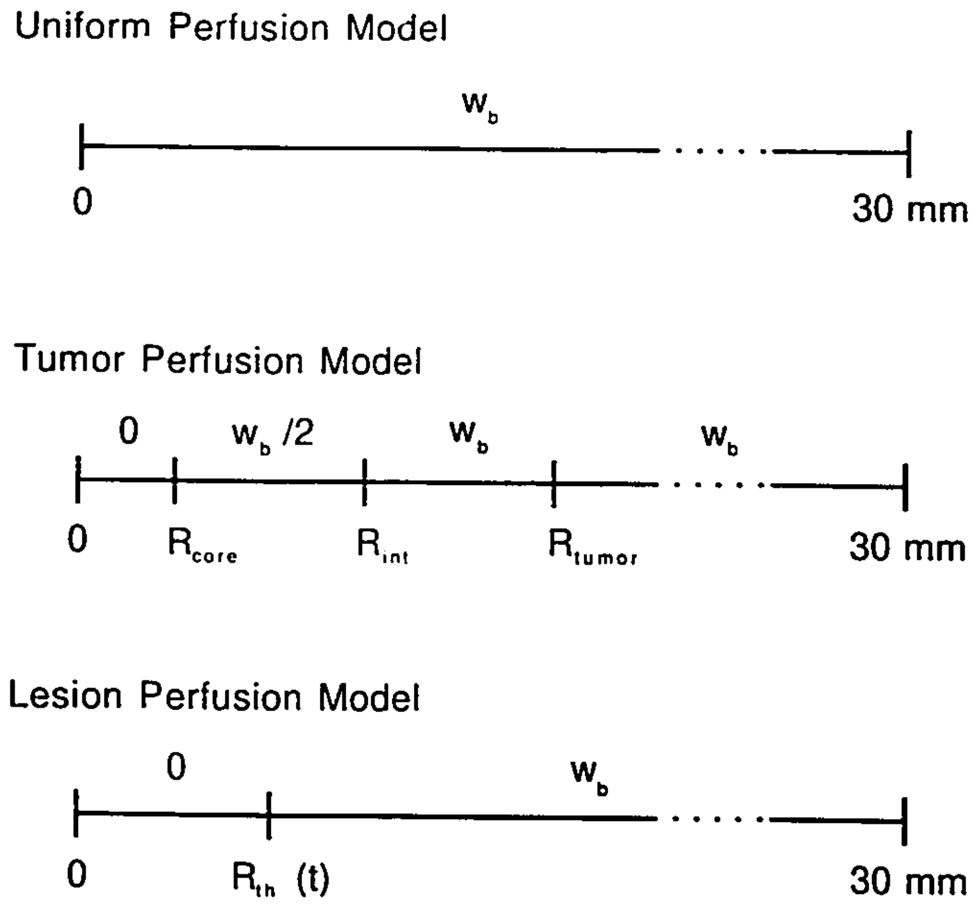

Figure 4.5. Static and dynamic approximations for blood perfusion patterns in tissue during ILP. $R_{th}(t)$, determined by (2.15), increases from an initial value of zero during the irradiation.

In the lesion perfusion model, we consider a radially expanding zone of non-perfused necrotic tissue bounded by $R_{th}(t)$, the thermal lesion radius, defined as the radius of tissue exposed to an equivalent time at 43°C of 3600 s and determined by (2.15).

Consider a 10 mm spherical tumor (R_{tumor} = 5 mm, R_{int} = 3 mm and R_{core} = 1 mm) irradiated for 600 s at a laser power of 2.5 W. The effect of perfusion pattern, for w_b=100 ml/100 g/min, on temperature distributions and thermal damage dimensions is shown in Figs. 4.6 and 4.7, respectively. Calculated radial temperatures at the end of the irradiation for $(\mu_s')_{coag} = (\mu_s')_{norm}$ are shown in Fig. 4.6(a). The uniform perfusion model predicts the lowest temperatures. The temperatures predicted by the lesion perfusion model are greater than those for the tumor perfusion model. However the maximum temperatures predicted by all three perfusion models differ by only 8 °C.

If we assume a scattering increase of $(\mu_s')_{coag} = 4(\mu_s')_{norm}$, the calculated radial temperature profiles at the end of the irradiation, shown in Fig. 4.6(b), are markedly different. The calculated temperatures for the uniform perfusion model in Figs. 4.6(a) and (b) are identical, because the threshold temperature for coagulation is not reached. The maximum tissue temperatures predicted by the lesion and tumor perfusion models in Fig. 4.6(b) differ by 25 °C, compared to 5 °C in Fig. 4.6(a). This suggests that temperatures are more sensitive to coagulation-induced increases in scattering than to differing perfusion patterns.

The predicted diameter of thermal damage for the three perfusion models

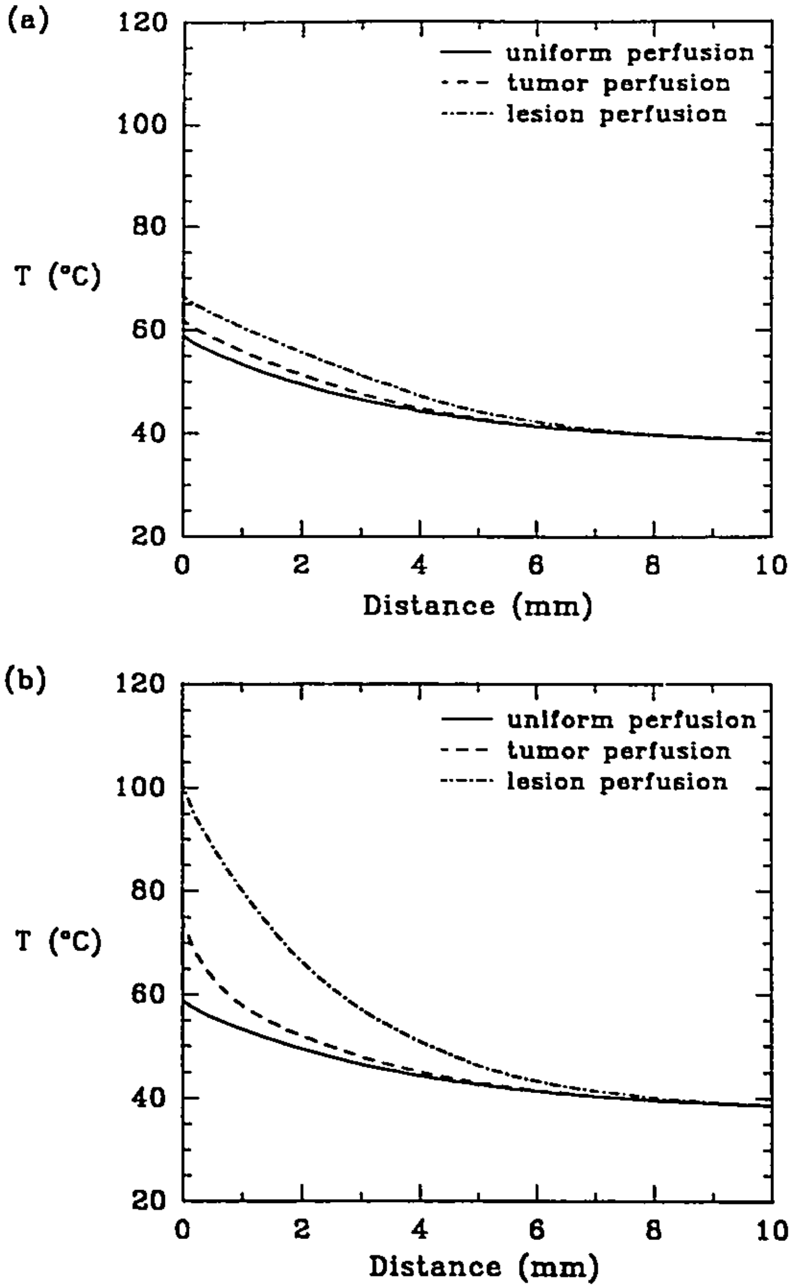

Figure 4.6. Effect of perfusion pattern on temperature distributions in liver for a 600 s irradiation at 2.5 W. (a) Calculated radial temperatures assuming $(\mu_s')_{coag} = (\mu_s')_{norm}$. (b) Calculated radial temperatures assuming $(\mu_s')_{coag} = 4(\mu_s')_{norm}$. Perfusion patterns shown in Fig. 4.5 with w_b = 100 ml/100 g/min are used in calculating these results.

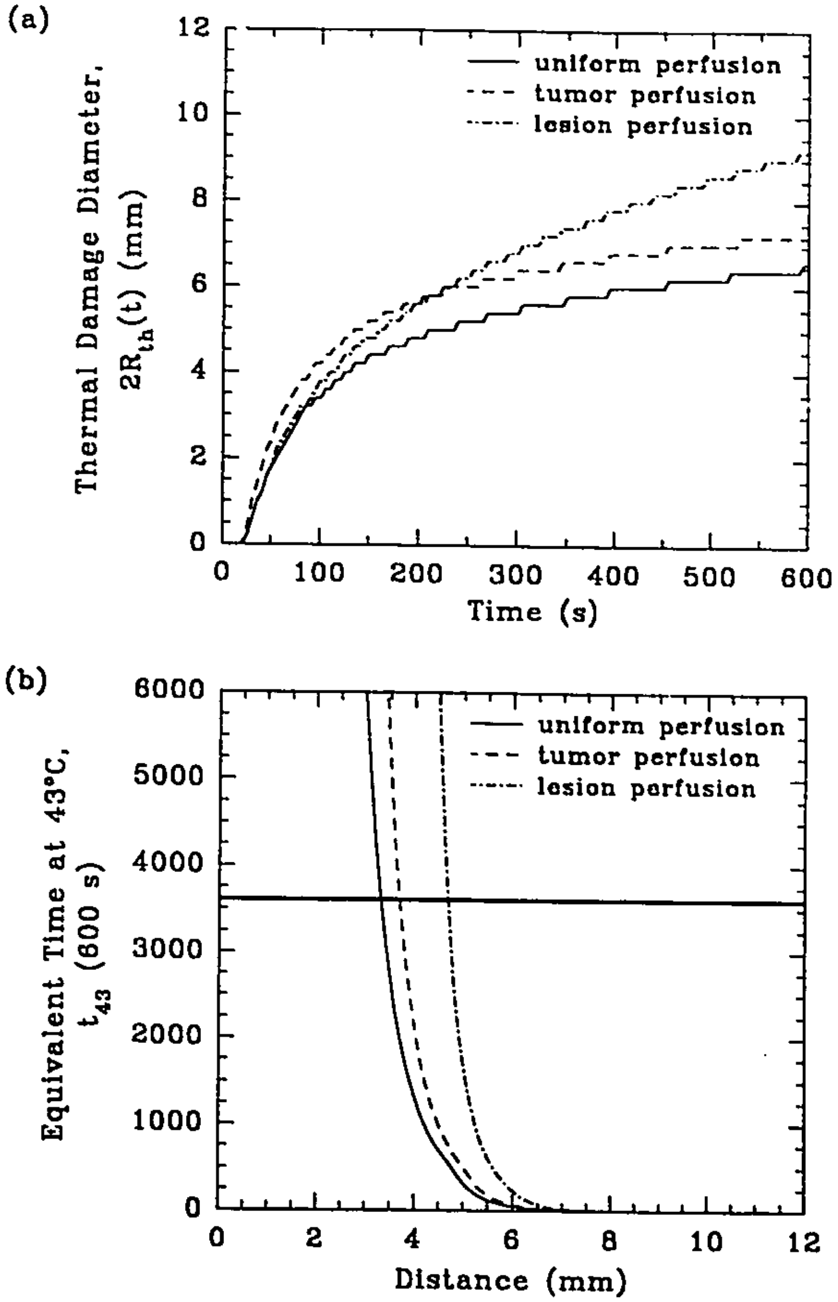

Figure 4.7. (a) Predicted thermal damage diameter in liver for the simulations in Fig. 4.6(b). (b) Radial distribution of equivalent times at 43°C in liver at the end of the irradiation. The solid horizontal bar corresponds to an equivalent time at 43°C of 1 hour (3600s).

for the case of a scattering increase is shown in Fig. 4.7(a). As expected, the thermal damage predicted with tumor perfusion always exceeds that with uniform perfusion. Interestingly, the diameters of thermal damage for the uniform and lesion perfusion approximations are similar up to ~ 90 s, the latter model predicts $w_b = 0$ at $r < 1.5$ mm. Fig. 4.7(a) indicates that the thermal damage based on a lesion perfusion model will continue to expand at longer irradiation times due to the perfusion patterns temperature-time dependence. Therefore thermal equilibrium can only be approximated.

The diameters of thermal damage predicted by the tumor and lesion perfusion approximations cross at 6 mm, corresponding to the static 3 mm intermediate perfusion radius, R_{int}, assumed in the tumor perfusion model. If R_{th} in the lesion perfusion approximation is greater than R_{int} in the tumor perfusion approximation, the former will predict greater thermal damage. This also accounts for the difference between final temperature distributions for the lesion and tumor perfusion models observed in Fig. 4.6(b).

The corresponding equivalent times at 43°C, t_{43}, at the end of the irradiation are shown in Fig. 4.7(b). A t_{43} of 3600 s, as indicated on the figure, was used as an index of thermal damage. Fig. 4.7(b) indicates that the demarcation between damaged (necrotic) and viable tissues is sharp.

Maximum transient temperature profiles, defined as the temperature at 0.1 mm (the first radial node), and thermal damage dimensions based on the lesion perfusion approximation (w_b=100ml/100 g/min) with $(\mu_s')_{coag} = 4(\mu_s')_{norm}$ are shown in Figs. 4.8(a) and (b), respectively, as a function of total laser power. In Fig. 4.8(a) for a power of 2.5 W, coagulation occurs at ~ 125 s, causing a rapid and substantial increase in the maximum tissue temperature. Prior to the onset of coagulation, the maximum tissue temperature increases almost linearly with increasing laser power. For a 3.0 W irradiation tissue temperatures exceed 100°C. Included in Fig. 4.8(a) is the thermal history for the 2.5 W irradiation at r=5 mm, where the effect of coagulation on temperatures is observed to be greatly reduced. This suggests that controlling laser power by temperature feedback at practical sensor locations (i.e r=5 mm) may fall short of preventing the onset of vaporization and carbonization.

The corresponding thermal damage dimensions are shown in Fig. 4.8(b) and indicate that the diameter of thermal damage increases almost linearly with increasing laser power from 1.5 W to 3.0 W. However, for a 3 W irradiation, predicted tissue temperatures, in Fig. 4.8(a), exceed 100°C early in the irradiation. Vaporization of tissue water above 100°C, not accounted for in the model, would result in higher temperatures near the source due to the associated reduction in thermal conductivity. The nonflat asymptote observed in Fig. 4.8(b) is consistent with experimental evidence in liver (Malone et al. 1994b).

Maximizing tissue damage while maintaining temperatures below 100°C, is a laser power and exposure optimization problem. Maximum coagulation and thermal damage in human liver for a 600 s irradiation, based on the lesion perfusion approximation, with $(\mu_s')_{coag} = 4(\mu_s')_{norm}$ is shown in Fig. 4.9. The

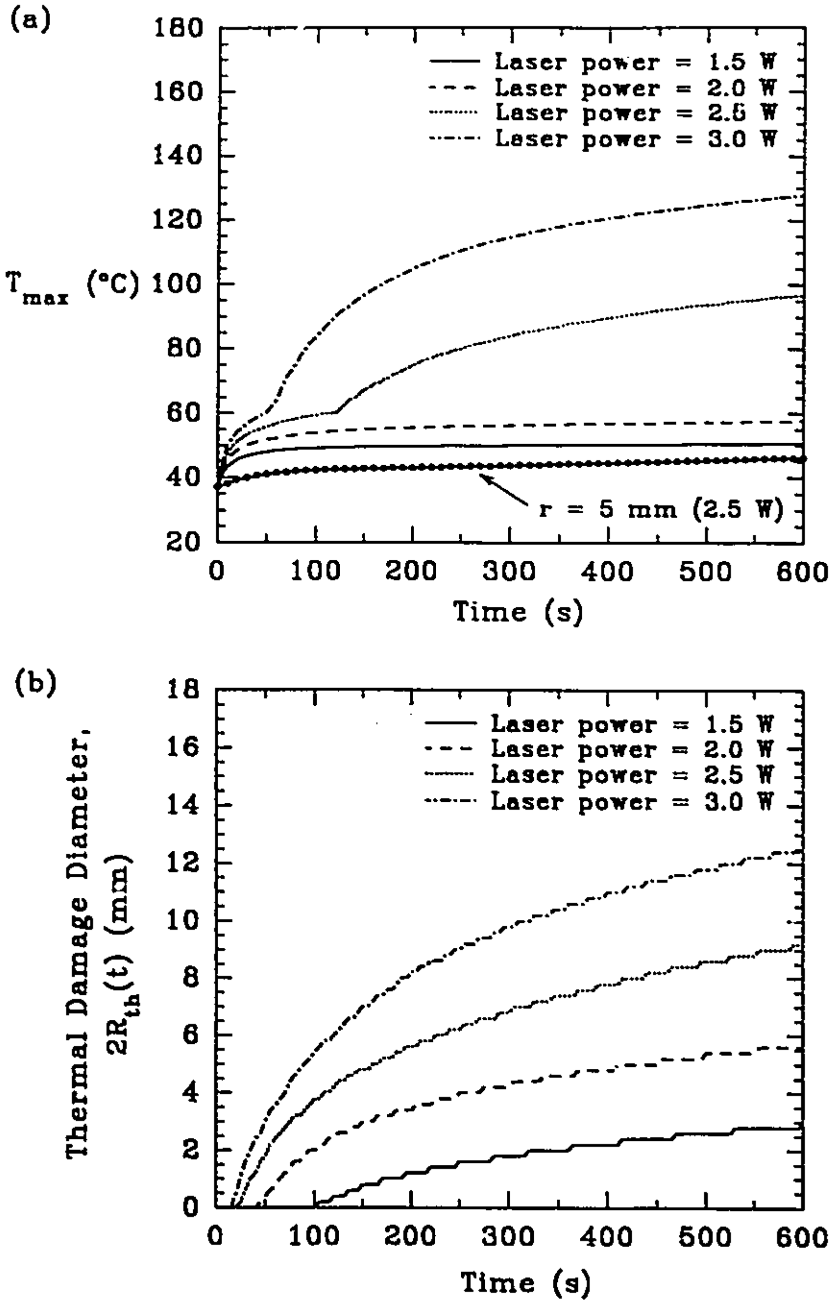

Figure 4.8. (a) Calculated transient temperatures at r=0.1 mm (maximum) in liver as a function of laser power assuming $(\mu_s')_{coag} = 4(\mu_s')_{norm}$. (b) Corresponding thermal damage diameter is shown. The lesion perfusion approximation with w_b = 100 ml/100 g/min was used to calculate temperatures.

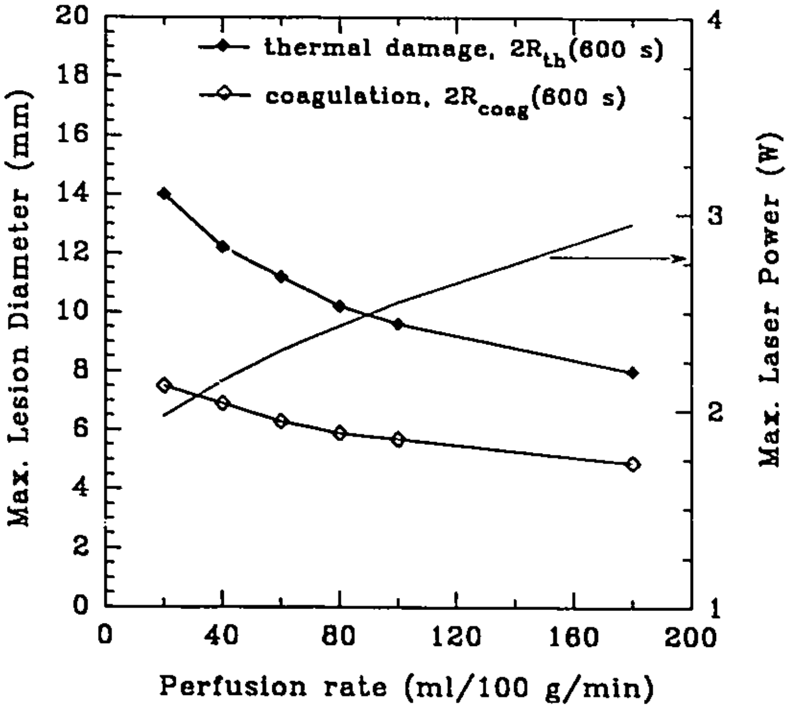

Figure 4.9. Predicted maximum thermal damage and coagulation diameters for a 600 s irradiation in liver as a function of perfusion rate. For each perfusion rate the laser power required to induce a maximum tissue temperature of 100°C ± 0.5°C is plotted (refer to the right vertical axis). The lesion perfusion approximation was used to calculate temperatures.

maximum predicted tissue temperature for all simulations ranged from 100.2°C to 100.5°C.

As expected, the predicted thermal damage diameters are larger than the coagulation diameters, given that the former includes accumulated low temperature damage. The predicted temperature at the boundary of thermal damage ranged from 47.6°C - 47.8°C. As blood perfusion increases the optimal power increases but coagulation and thermal damage are reduced. This is expected given the thermal response to increased perfusion observed in Fig. 4.4(a). Furthermore, the thermal damage diameter exceeds the coagulation diameter by ~ 6.5 mm and 3.0 mm at 20 ml/100g/min and 100 ml/100g/min, respectively. Using a similar coagulation model, Prapavat et al. (1996) reported differences between thermal damage and coagulation diameters of ~ 2 mm for *in vitro* liver simulations for P = 2.0 - 4.6 W at 850 nm.

For a mean blood perfusion rate of 100 ml/100 g/min, Fig. 4.9 indicates that single fiber ILP at an optimal power of 2.55 W for 600 s will produce coagulation and damage diameters of 5.6 mm and 9.6 mm, respectively. This is consistent with *in vivo* liver simulations reported by Prapavat et al. (1996) whereby a 10 mm damage diameter could not be induced for P ≤ 3.0 W. These results suggests that vaporization and possibly carbonization is required to produce *in vivo* lesions greater than ~ 10 mm, consistent with experimental evidence in liver (van Hillegersberg et al. 1994). Precharring of the fiber tip has been shown to produce larger thermal lesions (Wyman et al. 1994, Amin et al.

1993b).

The approximation to the Arrhenius damage integral given by (2.15) is based on average hyperthermic cell killing in various tissue types. However, Davies et al. (1989) demonstrated that (2.15) provided a reasonable estimate of thermal damage formation in canine liver, exposed to temperatures exceeding 100°C. The thermal damage model could be improved using tissue-specific reaction coefficients, A and ΔE, for denaturation. Given that coagulation also depends on the temperature-time history, the 60°C threshold model used in this study may underestimate true coagulation dimensions at steady-state.

Generally laser power remains constant during ILP such that tissue temperatures are maximum at the end of the irradiation. If higher tissue temperatures could be induced earlier in the irradiation, could greater damage be produced? Consider the maximum tissue temperature histories in liver (w_b=100 ml/100 g/min) for a constant optimal power of 2.55 W (from Fig. 4.9) and a transient laser power scheme (see Fig. 4.10) shown in Fig. 4.11(a). A power scheme of 5.0 W for 30 s, 3.0 W for the next 30 s and then 2.5 W for the remainder of the irradiation attempts to maintain maximal heating below the 100°C temperature threshold.

Thermal damage formation for the different power schemes is shown in Fig.4.11(b). Final damage diameters at 600 s differ by only 0.5 mm. However, Fig. 4.11(b) indicates that greater thermal damage can be realized earlier in the irradiation by using a transient power scheme. For example, an 8 mm damage

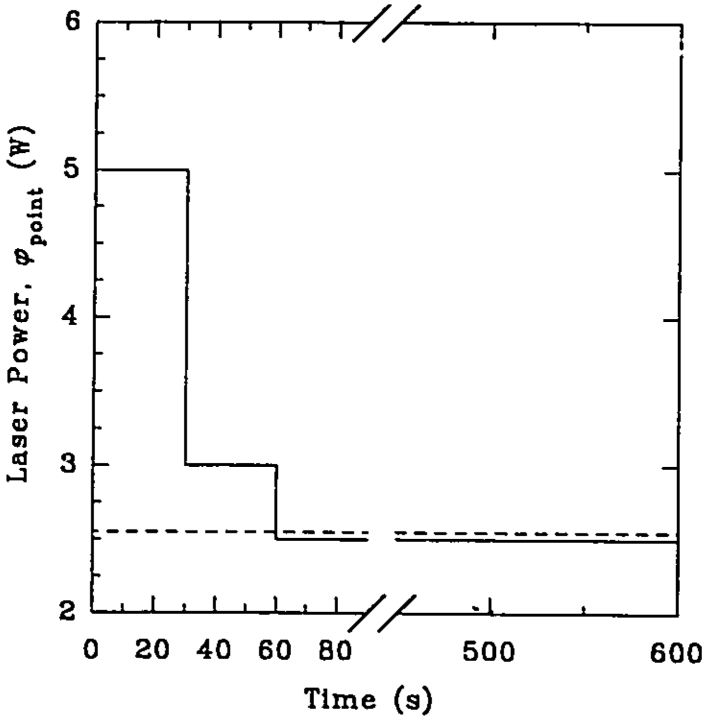

Figure 4.10. Transient and constant power schemes used to maintain maximal heating below a threshold temperature of 100°C in perfused liver (w_b = 100 ml/100 g/min).

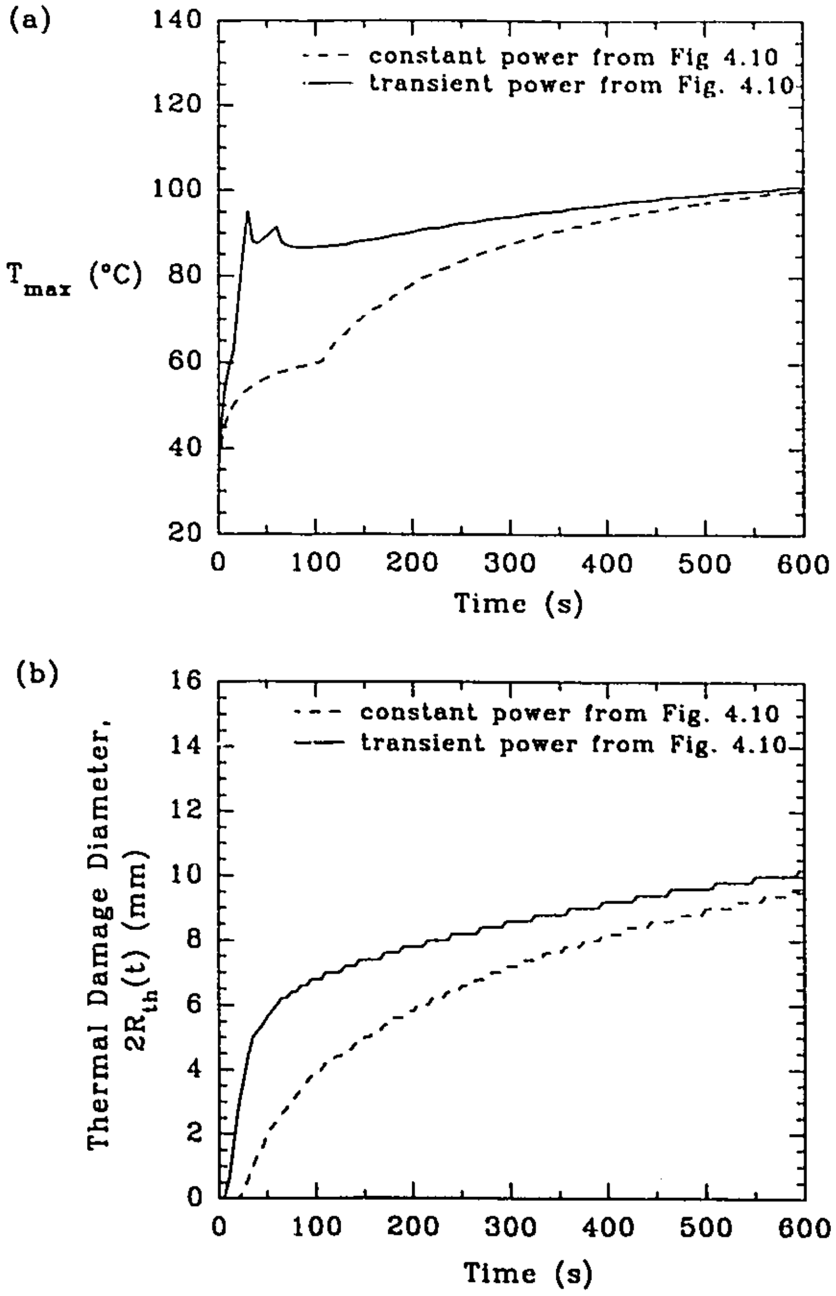

Figure 4.11. (a) Maximum tissue temperature histories in liver for 2.55 W of constant power and the transient power scheme shown in Fig. 4.10. (b) Corresponding thermal damage diameters. The lesion perfusion approximation with w_b = 100 ml/100 g/min was used to calculate temperatures.

diameter is predicted at 200 s for transient power compared to 350 s for constant power. This may be important in clinical settings where there is a potential for optical fibers and temperature sensors to be displaced during treatment.

The results presented do not consider modifications in μ_a due to the presence of blood as indicated by Wilson (1991). Marchesini et al. (1994) observed that the absorption spectrum for human colon *ex vivo* from 300 nm to 800 nm resembled the hemoglobin absorption spectrum, indicating that optical absorption may be dominated by blood. The absorption coefficient for hemoglobin in the near infrared is approximately constant and is well approximated by 2.54 cm^{-1} at 960 nm (Cheong et al. 1990). This is approximately 5 times that of normal bovine liver *ex vivo*. For highly perfused tissues such as liver, it therefore seems reasonable to assume that, at 1064 nm, μ_a may increase by as much as twofold *in vivo*. The effect on thermal damage formation in liver of increased optical absorption due to the presence of blood, for the lesion perfusion approximation (w_b = 100 ml/100 g/min) is shown in Fig. 4.12. We assume that a μ_a increase is limited only to viable perfused liver as determined by $R_{th}(t)$. It is observed in Fig. 4.12 that there is a nonlinear increase in damage diameter with increasing optical absorption. A twofold increase in μ_a increases the predicted damage diameter by 2.8 mm (33%).

The optical properties of *in vivo* tissues are not well determined and, therefore, quantifying the increase in optical absorption has yet to be realized. Furthermore, blood perfusion in tissues is highly variable (Feldmann et al. 1992)

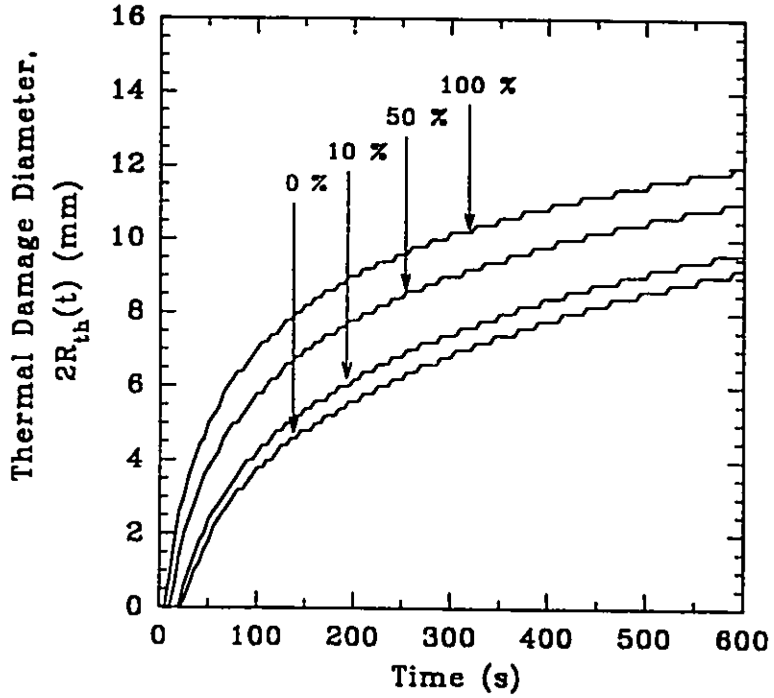

Figure 4.12. Effect of increased optical absorption *in vivo* on thermal damage formation. The curves represent percentage increases in μ_a above 0.53 cm^{-1}. The lesion perfusion approximation with w_b = 100 ml/100 g/min was used to calculate temperatures with increased μ_a limited to $r > R_{th}(t)$.

and any increase in optical absorption would most certainly be coupled with the perfusion rate.

4.2 Estimation of Tissue Charring Temperature *Ex vivo*

Photocoagulation was performed *ex vivo* in bovine muscle at either 1064 nm or 800 nm. Preliminary experiments showed that illuminating with 1.5 W at 1064 nm required an exposure duration of 300 s to produce char. For the same optical power at 800 nm, a 1200 s exposure was required for char production. Measured *ex vivo* temperature profiles for 300 s illuminations of 1.5 W at 1064 nm in bovine muscle are shown in Fig. 4.13. Temperatures were acquired at 5 s intervals. Measured temperature profiles in Figs. 4.13(a) and (b) are unremarkable up to approximately 200 s. At t > 200 s, temperature increases in Fig. 4.13(a) are much larger than in Fig. 4.13(b).

Measured *ex vivo* temperature profiles for 1200 s illuminations of 1.5 W at 800 nm in bovine muscle are shown in Fig. 4.14. Measured temperature profiles at 5 mm and 7 mm in Figs. 4.14(a) and (b) are unremarkable. At 3 mm temperature increases in Figs. 4.14(a) and (b) differ slightly. This may be a result of slight differences in the local tissue properties of each sample. The temperature reduction reported at 3 mm at 900 s, in Fig. 4.14(a), is likely a result of damage to the fiber tip, observed post-illumination, brought about by tissue charring. Generally, measured temperatures for 1064 nm illuminations are greater than those for 800 nm illuminations. This will be discussed in section 4.3.

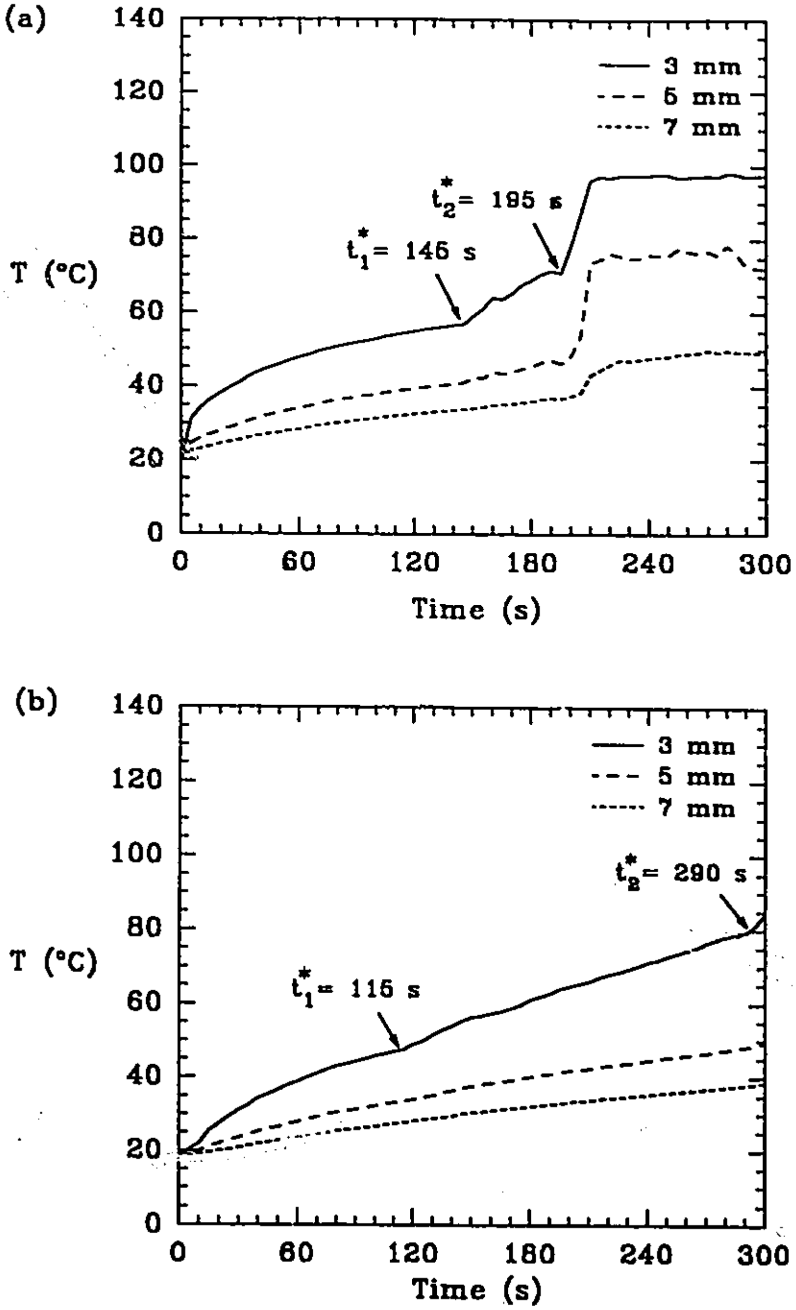

Figure 4.13. Measured temperature profiles in lean bovine muscle illuminated by 1.5 W of continuous-wave 1064 nm Nd:YAG laser energy for 300 s. (a) Trial 1 and (b) Trial 2; t_1^* and t_2^* are times of sudden temperature changes at 3 mm from the source.

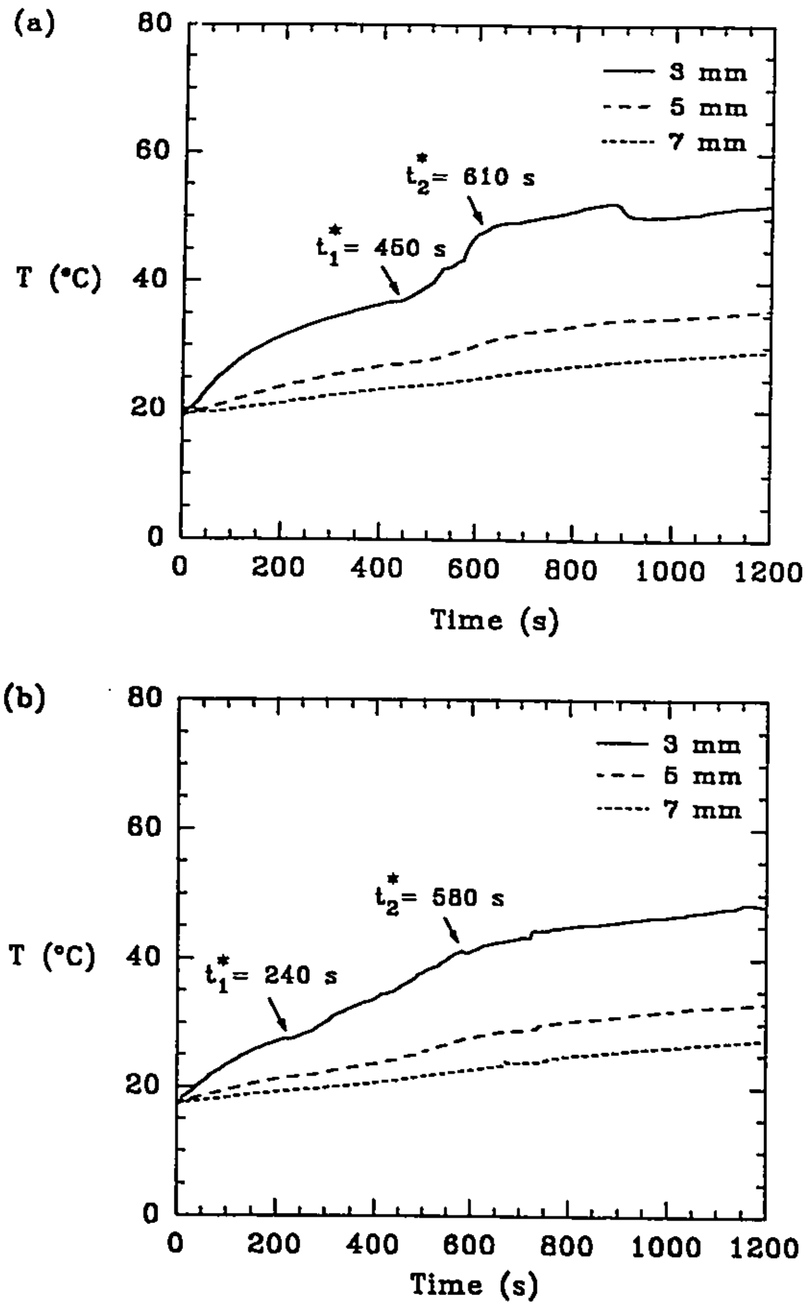

Figure 4.14. Measured temperature profiles in lean bovine muscle illuminated by 1.5 W of continuous-wave 800 nm diode laser energy for 1200 s. (a) Trial 1 and (b) Trial 2; t_1^* and t_2^* are times of sudden temperature changes at 3 mm from the source.

The measured char diameter for each *ex vivo* illumination at 1064 nm was 2.0 ± 0.3 mm, whereas at 800 nm each char diameter was 2.5 ± 0.3 mm. Measurement uncertainty was dominated by geometric irregularity. Given the heat of vaporization of water to be 2255 J/g, the energy required to vaporize the small volume of tissue water in the charred regions for the 1064 nm and 800 nm illuminations was estimated to be 8 J and 19 J, respectively. This is equivalent to ~ 1% of the exposure for each experiment and was, therefore, not incorporated into the thermal model. In Fig. 4.13 there is no significant flattening of the measured temperature profiles at or near 60°C. Therefore the change in enthalpy for the coagulation transition was also not modelled.

Each profile in Figs. 4.13 and 4.14 exhibits a sudden change in the rate of temperature increase at times t_1^* and t_2^* as reported by a microthermocouple positioned 3 mm away from the optical fiber. The choice of t_1^* in Figs. 4.13(b) and 4.14(b) is less arbitrary than may appear, this is discussed later. Once the charring process begins at the source fiber, there is a time delay given by $t_{delay} = r^2\rho c/3k$ (Chapman 1987) before this event will register as a sudden temperature change r mm away. Thus, t_1^* and t_2^* values were corrected using this single delay time, according to $t_n = t_n^* - t_{delay}$ before being input into the calculational model.

These temperature changes were interpreted 3 different ways:

1) sudden onset of opaque char at $t_c = t_1$,

2) sudden onset of opaque char at $t_c = t_2$,

3) onset of a continuous progressive browning at $t_b = t_1$ culminating in

opaque char at $t_c = t_2$.

The optical and thermophysical properties used in the calculational model are shown in Table 4.2. Initial properties are shown in the last column. The absorption and reduced scattering coefficients are valid for bovine muscle at 1064 nm (Cheong et al. 1990) and at 810 nm (Jaywant et al. 1993). Initial thermophysical properties were determined using (2.12), assuming that bovine muscle is composed of 80% water, 10% fat and 10% protein, consistent with published values (Duck 1990). For coagulated tissue, $r \leq R_{coag}(t)$, we assume a twofold increase in μ_s' whereas μ_a remains at the initial value. For vaporization of tissue water, $r \leq R_{vapr}(t)$, the thermophysical properties are determined using (2.12) assuming that the residual material after vaporization is composed of 0% water, 50% fat and 50% protein.

Calculated transient temperature profiles (see section 3.5) at 1 mm and 3 mm from the source for each charring/browning interpretation, generated using t_1 and t_2 determined for each 1064 nm experiment in Fig. 4.13, are shown in Figs. 4.15 and 4.16, respectively. For the initial thermophysical properties in Table 4.2, $t_{delay} \sim 20$ s at $r = 3$ mm.

At 1 mm from the source, Fig. 4.15, sudden onset of opaque char causes the temperature to rise rapidly. The time it takes for the temperature to rise to within a factor 1/e of the steady state temperature (time to shoulder of curve) is ~ 15 s, and in general depends on the thermal diffusion time, $L(t) = (4kt/\rho c)^{1/2}$ (Chapman 1987). The model for tissue browning in Figs. 4.15(a) and (b) has at all

Table 4.2. Optical and thermophysical properties used in the calculational model.

Absorption Coefficient (cm^{-1})	$r \le R_{coag}$	$r > R_{coag}$
at 800 nm	0.12	0.12
at 1064 nm	1.2	1.2
Reduced Scattering Coefficient (cm^{-1})		
at 800 nm	8.0	4.0
at 1064 nm	5.6	2.8
	$r \le R_{vapr}$	$r > R_{vapr}$
Tissue Thermal Conductivity (W/cm/°C)	0.00186	0.00548
Tissue Density (g/cm^3)	1.07	1.02
Specific Heat of Tissue (J/g/°C)	1.70	3.70

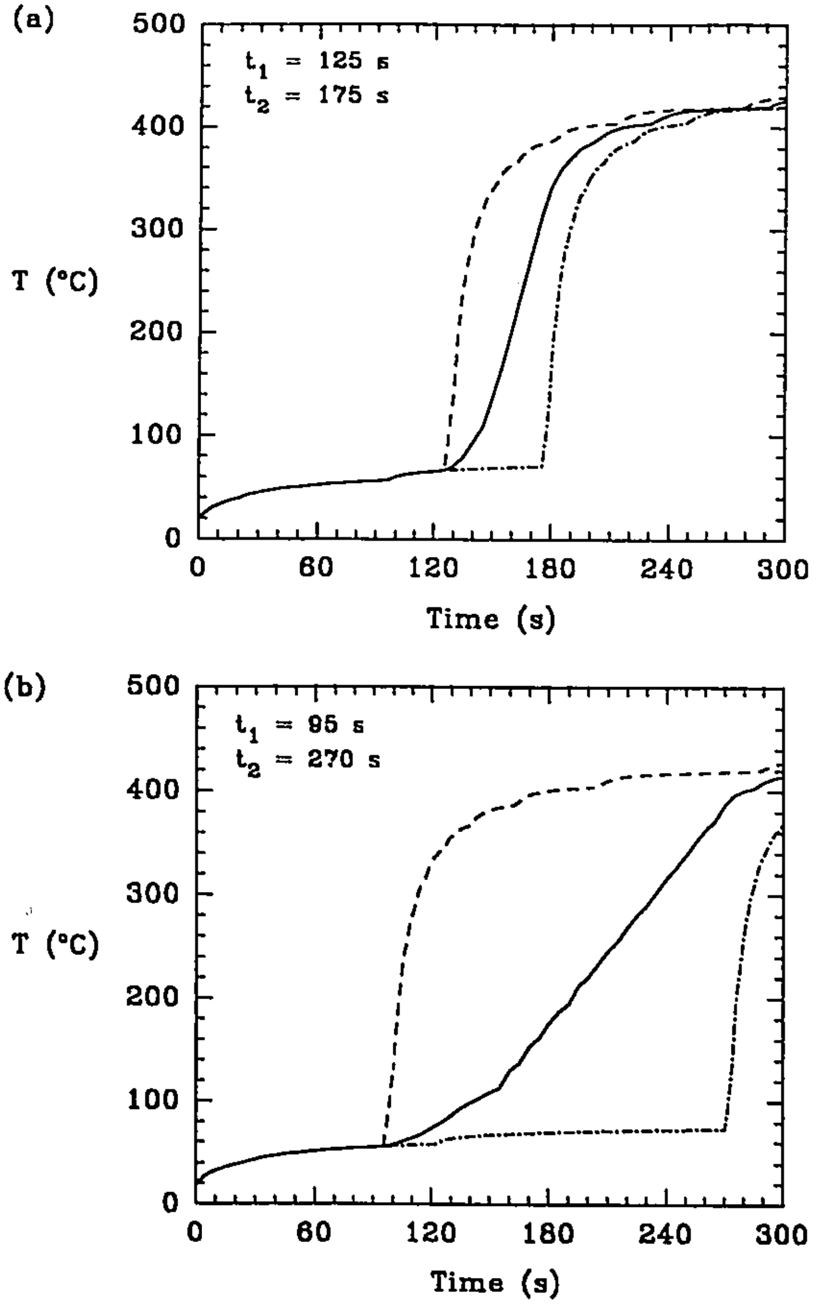

Figure 4.15. Calculated thermal history at r = 1 mm for the 1064 nm illuminations, using t_1 and t_2 determined from Fig. 4.13 as timers for the onset of tissue charring and/or browning. (a) t_1 = 125 s, t_2 = 175 s and (b) t_1 = 95 s, t_2 = 270 s; sudden onset of opaque char at $t_c = t_1$ (—) or at $t_c = t_2$ (---), browning at $t_b = t_1$ culminating in opaque char at $t_c = t_2$ (——).

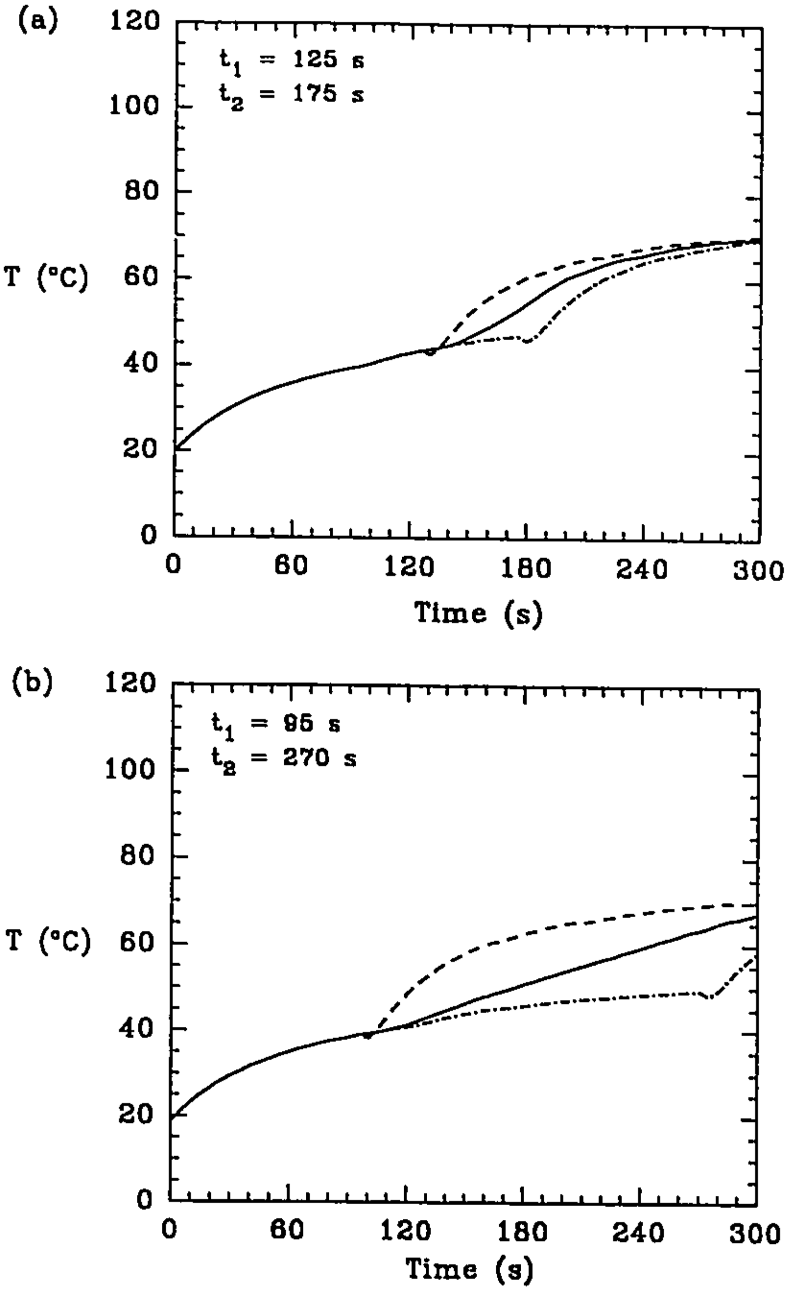

Figure 4.16. Calculated thermal history at r = 3 mm for the 1064 nm illuminations, using t_1 and t_2 determined from Fig. 4.13 as timers for the onset of tissue charring and/or browning. (a) t_1 = 125 s, t_2 = 175 s and (b) t_1 = 95 s, t_2 = 270 s; sudden onset of opaque char at $t_c = t_1$ (---), or at $t_c = t_2$ (-·-), browning at $t_b = t_1$ culminating in opaque char at $t_c = t_2$ (——).

points an approximate linear increase in temperature from t_b to t_c. The bumpiness of the calculated curves in Figs. 4.15 and 4.16 is a result of our threshold vaporization model and the discrete nature of its solution on a finite difference grid. As node spacing is decreased, the curves can be further smoothed.

Prior to tissue charring or browning, measured (Fig. 4.13) and model-predicted temperatures at 3 mm (Fig. 4.16) for each 1064 nm illumination show only qualitative agreement. The differences can be attributed to the 1.0 mm uncertainty associated with microthermocouple array position, showing clearly the rationale for using measured temperatures only as timers. Calculated temperature profiles at 3 mm in Fig. 4.16 for sudden onset of opaque char exhibit a temperature decrease immediately following t_c, characteristic of a delay in the arrival of thermal energy from a heat source at r=0. The model for tissue browning in Figs. 4.16(a) and (b) produces, however, an approximate linear increase in temperature from t_b to t_c, consistent with the measured temperature profiles at 3 mm in Figs. 4.13(a) and (b). This suggests that temperature increases in lean bovine muscle for Nd:YAG illumination are consistent with a tissue browning model. Fig. 4.13 also indicates that the time over which charring develops can differ substantially between samples of the same tissue type. The sudden and rapid measured temperature increase at t_2 in Fig. 4.13(a) could not be accounted for in either description of tissue charring.

The choice of t_1^* in Figs. 4.13(b) and 4.14(b) was based on prior observations of the shape of transient temperature profiles associated with laser illuminations without browning or char production. This shape is illustrated in Fig. 4.16(b) for the case of a strictly optical source (---) up to t=270 s. Measured temperature profiles at 3 mm in Figs. 4.13(b) and 4.14(b) begin to deviate from this shape at t_1^*.

The calculated char temperatures at the char radius for each 1064 nm and 800 nm illumination and each interpretation are shown in Table 4.3. All calculated char temperatures at 1064 nm agree to within 14°C, except for sudden onset of opaque char at t_2 from Fig. 4.15(b), where the shoulder of the calculated temperature profile was not reached at the end of the illumination. Calculated char temperatures for the 800 nm illuminations were determined by linear interpolation between model-predicted temperatures at 1.2 mm and 1.3 mm and agree to within 8°C. The ~ 92°C and 62°C uncertainties in individual estimates of T_{char} at 1064 nm and 800 nm, respectively, were determined by the calculated temperatures corresponding to a ± 0.3 mm error in the char diameters. These uncertainties are a result of the extremely large predicted thermal gradients, ~ 610°C/mm and ~ 410°C/mm, at the measured char boundaries for 1064 nm and 800 nm illuminations, respectively.

The average T_{char} values for each wavelength investigated differ by ~ 59°C, but agree within estimated uncertainties. Given that the continuous browning model is most consistent with temperature changes observed in this study, T_{char} was determined using the four results obtained using this model (last column of Table 4.3). The mean of these estimates of T_{char} is 389 ± 77°C, using quadrature

Table 4.3. Estimates of tissue char temperature, T_{char}, based on three different interpretations of Figs. 4.13 and 4.14.

Timers determined from *ex vivo* observations in Figs. 4.13 and 4.14	**Sudden onset of opaque char at t_1**	**Sudden onset of opaque char at t_2**	**Browning at t_1, opaque char at t_2**
1064 nm: (t_1=125 s,t_2=175 s)	429 ± 92 °C	419 ± 92 °C	426 ± 92 °C
1064 nm: (t_1=95 s,t_2=270 s)	427 ± 92 °C	369 ± 90 °C	415 ± 92 °C
800 nm: (t_1=430 s,t_2=590 s)	361 ± 62 °C	361 ± 62 °C	361 ± 62 °C
800 nm: (t_1=220 s,t_2=560 s)	353 ± 62 °C	353 ± 62 °C	353 ± 62 °C

summation for the combined uncertainty.

The effect of different step increases in the reduced scattering coefficient on the calculated charring temperature, T_{char}, is shown in Fig. 4.17. Char temperatures were generated using the browning model for the 1064 nm illumination with t_1 and t_2 from Fig. 4.15(b). Step increases in the reduced scattering coefficient at $r \leq R_{coag}$ up to an order of magnitude increased the model-predicted T_{char} by only 4.5°C (~ 1%). A similar result was observed for 800 nm illuminations. In the absence of tissue water vaporization and carbonization, temperatures are sensitive to coagulation-induced changes in scattering as observed in Fig. 4.2. It was observed in this study that calculated temperature distributions are more sensitive to changes in the thermal conductivity than to changes in the reduced scattering coefficient. Therefore, Fig. 4.17 indicates that if charring occurs, final tissue temperatures are effected minimally by coagulation-induced increases in scattering.

The optical model presented here is likely more valid for spherically diffusing fiber tips, than for plane-cut fiber tips which emit optical energy in the forward direction. In some instances, plane-cut fibers produce ellipsoidal lesions around and centered ahead of the fiber tip (Matsumoto et al. 1992). Given that the char diameters were measured orthogonal to the plane-cut fiber tip, our approximation would, therefore, likely overestimate T_{char}. Additionally, increased optical absorption in the browned region was modelled as a power spike at the fiber tip (r=0 in the model). With this approximation, optical diffusion in the

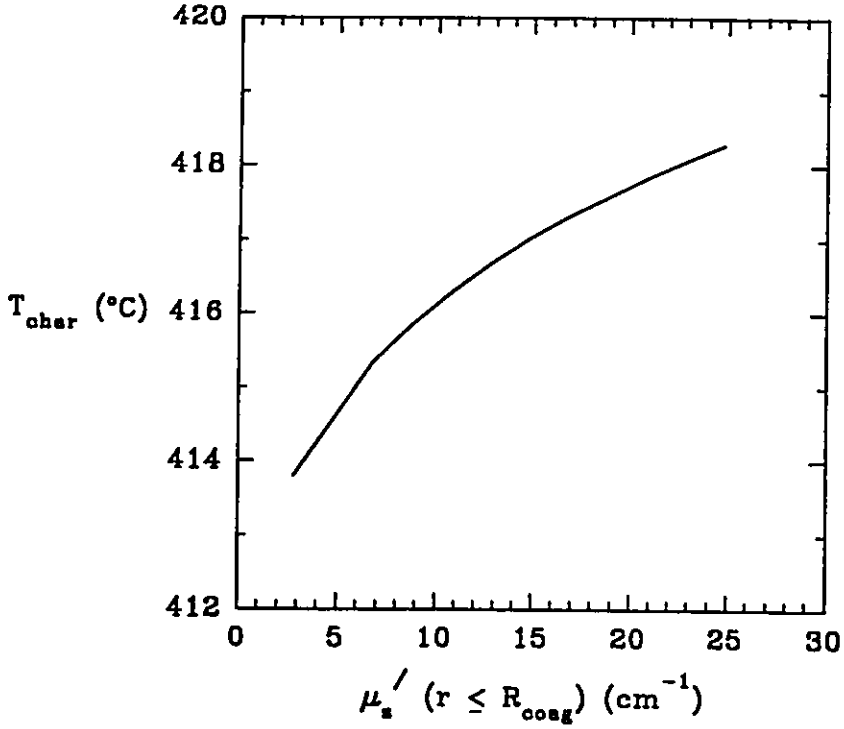

Figure 4.17. Calculated T_{char} using the tissue browning model for the 1064 nm illumination, with t_1 and t_2 from Fig. 4.15(b), as a function of the step increase in the reduced scattering coefficient at $r \leq R_{coag}(t)$.

browned region is removed and, thus, predicted temperature profiles near the source are steepened. However, T_{char} was insensitive to coagulation-induced increases in optical scattering, indicating that changes in optical diffusion during browning should not strongly influence temperature distributions after the onset of opaque char.

Following the production of opaque char, the thermophysical properties in the charred region were assumed to be the same as the vaporized region. McKenzie (1986) estimated the thermal conductivity of tissue char to be 5.0×10^{-5} W/cm/°C, approximately 2 orders of magnitude smaller than that of bovine muscle *ex vivo* or the estimate for the water vaporization region. Our assumption would, therefore, likely underestimate temperatures within the measured char radius.

Despite these limitations, our estimate, $T_{char} = 389 \pm 77°C$, agrees with a published value of ~ 425°C for carbonization (charring) of porcine aortae illuminated by Nd:YAG optical energy (LeCarpentier et al. 1989). Calculated temperature profiles at 1 mm for continuous browning, Fig. 4.15, agree qualitatively with the thermographically measured post-ablation surface temperature profiles in that study. This indicates that tissue charring is likely the endpoint of a tissue browning process, characterized by increased optical absorption.

By determining T_{char}, current mathematical models of ILP can be extended to provide estimates of the char boundary, similar to the way 60°C is used to estimate the coagulation boundary (Whelan et al. 1995). This work also provides a useful insight into the time over which charring develops. It is uncertain how blood perfusion would affect the time or temperature at which charring occurs *in vivo*. The removal of heat by blood flow could delay the onset of charring. Conversely, significant absorption by hemoglobin (Boulnois 1986, Cheong et al. 1990) might quicken the onset of charring.

4.3 Photocoagulation in Bovine Muscle Ex Vivo at 800 nm and 1064 nm

Photocoagulation was performed ex vivo in bovine muscle at either 800 nm or 1064 nm. The choice of irradiation parameters required to induce a 10 mm coagulation lesion was assessed. The fiber tip was cleaned before each experiment. Coagulation lesions for 1.5 W irradiations at 800 nm are shown in Fig. 4.18. Lesions were elongated parallel to the fiber tip and central charring was observed. Lesion widths, measured orthogonal to the fiber tip, for 800 nm and 1064 nm irradiations are shown in Table 4.4.

For 1.5 W irradiations at 800 nm coagulation width increased with increased exposure. Central charring was observed for 1000 s and 1200 s exposures.

At 1064 nm central charring was absent in all 1.0 W irradiations and present in all 1.5 W irradiations. The 400 s coagulation width was anomalously small, likely a result of intersample variation in the tissue optical properties.

Table 4.4 shows that a 10 mm lesion can be produced in bovine muscle by

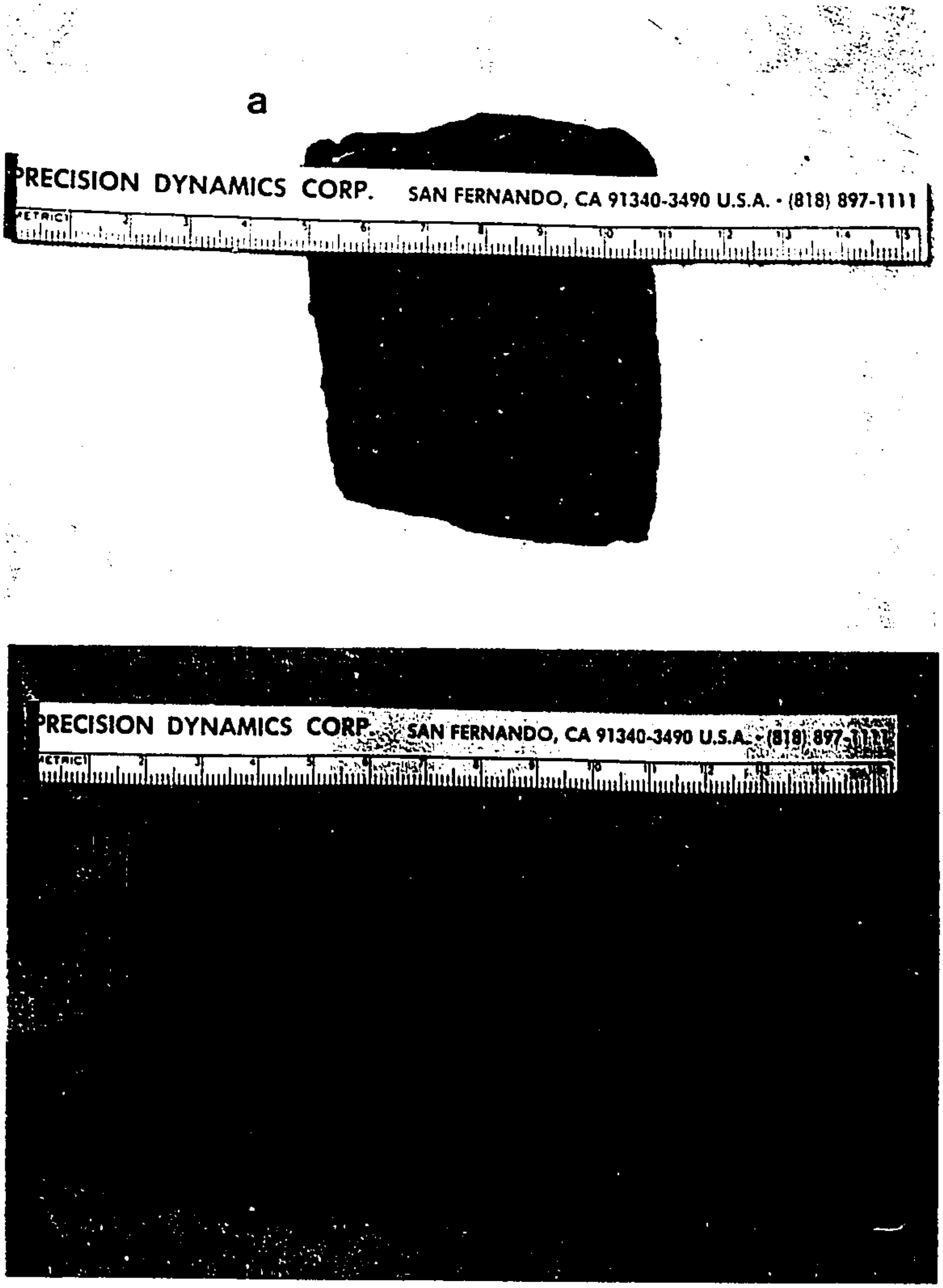

Figure 4.18. Single fiber ILP lesions in bovine muscle *ex vivo* produced by 1.5 W of 800 nm optical energy. (a) 1000 s exposure, (b) and (c) 1200 s exposures.

Table 4.4 Measured coagulation widths for ILP in bovine muscle at 800 nm and 1064 nm.

Delivered Power (W)	Exposure Duration (s)	Coagulation Width (mm)
<u>800nm</u>		
1.2	600	0
1.5	600	3.0
	1000	6.0*
	1200	9.5* (2)
<u>1064 nm</u>		
1.0	100	3.0
	200	4.0
	400	2.0
1.5	300	9.0* (2)
	600	10.0* (2)

* Denotes the presence of char in the lesions. () Denotes the number of repeated irradiations. The measurement uncertainty for each coagulation width is ±0.3 mm. For average widths the combined measurement and statistical uncertainty is ±1.0 mm.

depositing 1064 nm optical energy at 1.5 W for 600 s. Switching to 800 nm requires an approximate twofold increase in the exposure duration. This indicates that for the same power and exposure, 1064 nm ILP lesions in bovine muscle *ex vivo* are larger than 800 nm lesions. The difference may be explained in terms of the optical properties at the different wavelengths. Recently, Wyman and Whelan (1994) established a theoretical basis for ILP suggesting that lesion size increases with decreasing optical penetration, a result supported by experimental observations (Wyman et al. 1992). Using published values for the optical properties of uncoagulated bovine muscle *ex vivo* at 810 nm (Jaywant et al. 1993) and 1064 nm (Cheong et al. 1990), the corresponding optical penetration depths are 0.831 cm and 0.295 cm, respectively. The results presented are, therefore, consistent with the above hypothesis. In terms of heating, increased optical penetration reduces energy deposition near the fiber tip, as shown in Fig. 4.19.

These results contradict reports that 800 nm optical energy produced by laser diodes is, in fact, less penetrating *in vivo* than 1064 nm (Amin et al. 1993b, Jacques et al. 1992). This might be explained in terms of the differences between *ex vivo* and *in vivo* optical properties. Marchesini et al. (1994) observed that the absorption spectrum for human colon *ex vivo* from 300 nm to 800 nm resembled the hemoglobin absorption spectrum, indicating that optical absorption may be dominated by blood. The absorption coefficient for hemoglobin is approximately 20 and 2 times greater than the absorption coefficient for bovine muscle *ex vivo* at 810 nm and 1064 nm, respectively. This suggests that optical penetration in

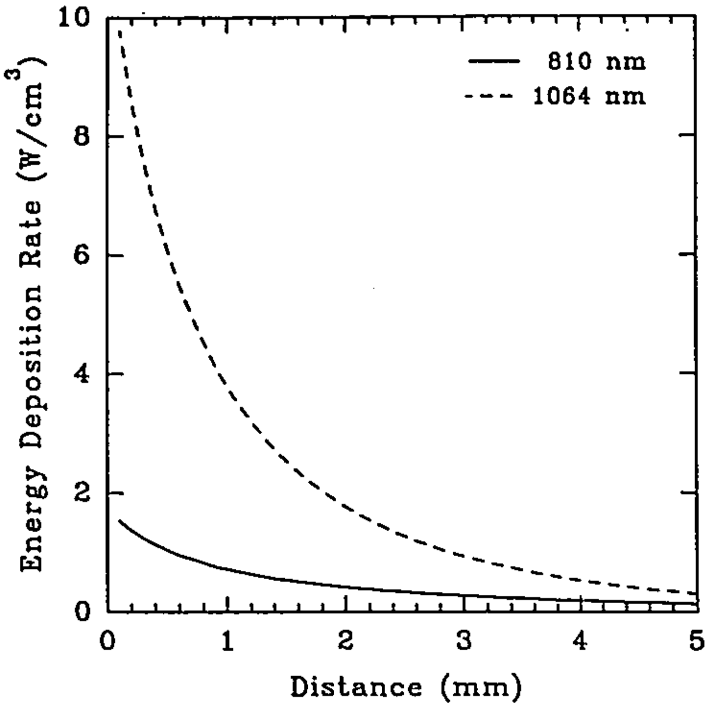

Figure 4.19. Calculated energy deposition rates for 1.5 W of 810 nm and 1064 nm optical energy in bovine muscle. Results are determined using published optical properties at 810 nm (Jaywant et al. 1993) and 1064 nm (Cheong et al. 1990).

bovine muscle would be reduced *in vivo* compared to *ex vivo*. It also suggests that the presence of blood may effect a greater decrease in optical penetration *in vivo* at 810 nm than at 1064 nm.

4.4 Temperature Reconstruction During Simulated ILP

4.4.1 1-D Homogeneous Test Cases

Initially we simplify the formulation to a linear description of interstitial laser photocoagulation for uniform optical and thermophysical properties. Simulated temperature measurements were generated using (3.4) with $\phi_{point} = 2.0$ W. The thermophysical (Bowman et al. 1975) and optical (Cheong et al. 1990) properties investigated are typical of mammalian tissues irradiated by 1064 nm optical energy and are represented by P_{true} in Table 4.5. The value for the effective thermal conductivity in Table 4.5 assumes a small blood perfusion contribution, enabling an assessment of the algorithm's performance for the difficult case where induced temperatures near the source are large. Estimations of larger k_{eff} values, which reduce radial temperatures, are presented later.

Stability of the algorithm was improved using relative sensitivity coefficients derived by multiplying (2.29) by P_n, reducing substantially the condition number of the inverse matrix in (2.31). The resulting relative parameter increments were converted to absolute increments at the end of each iteration. Reconstructions are presented as "Temperature Error", T_{err} (°C), distributions, the difference between reconstructed and true radial temperature profiles. The effects

Table 4.5. True and 2 sets of initial guess parameter vectors used, respectively, to generate simulated temperature measurements and start the parameter estimation algorithm.

	P_{true}	P_{g1}	P_{g2}
Effective thermal conductivity, (W/cm/°C)	5.0E-3	4.0E-3	1.0E-3
Volumetric heat capacity, (J/cm^3/°C)	4.0	3.2	1.0
Absorption coefficient, (cm^{-1})	2.0	1.6	1.0
Reduced scattering coefficient, (cm^{-1})	5.0	6.0	10.0

of sensor array design and positioning, sensor sampling, experimental noise and systematic errors were investigated.

4.4.1.1 Optimization of Temperature Acquisition Parameters

To optimize the number of sensors (M), sensor spacing and array-source distance, reconstructions were simulated using 2, 4 or 6 sensors with intersensor spacing of 2 mm, 4 mm or 6 mm, and with the sensor array positioned such that the first sensor was at a radial distance of 1, 3 or 5 mm from the optical source. The iterative temperature reconstruction algorithm, Fig. 3.6, was used to reconstruct temperatures at 30 s, 120 s and 300 s for each combination of the above three acquisition parameters, resulting in 81 test cases. In each reconstruction, sensors were sampled only once (S=1), at the time of reconstruction, 30 s, 120 s or 300 s.

Reconstructions were scored as successful, temperature errors less than 1°C at all points in the thermal field, or unsuccessful, temperature error greater than 1°C at any point. The influence of the initial guess parameter vector on the parameter estimates and resulting predicted temperature distribution was assessed using the two initial guess parameter vectors in Table 4.5. $\mathbf{P}_{g1}$ is a 20% deviation from each true tissue parameter and $\mathbf{P}_{g2}$ represents an "order of magnitude" guess in the same direction as $\mathbf{P}_{g1}$.

The scores, at 30 s, 120 s and 300 s, for temperatures reconstructed using

P_{g1} are shown in Fig. 4.20. Fig. 4.20 shows that the success of temperature reconstruction depends strongly on the number of sensors, sensor spacing and array-source distance, suggesting optimal temperature acquisition parameters exist. Scores from Fig. 4.20 were totalled for each value of a given acquisition parameter, representing a total of 27 reconstructions. Scores are presented in Fig. 4.21 as a percentage success rate. Success rates using P_{g2} to start the estimation algorithm are also presented in Fig. 4.21. Generally Fig. 4.21 shows that the reconstruction success rate is improved significantly using P_{g1} rather than P_{g2}, indicating that it is desirable to use an initial guess which is close to the true values. This could prove difficult for *in vivo* reconstructions given that k_{eff} may vary by a factor of ~ 3.5 (Weinbaum and Jiji 1985) and the optical properties of *in vivo* tissues are not well determined.

Fig. 4.21 indicates that the optimal sensor array design is 4 sensors spaced 2 mm apart. The optimal sensor number is not surprising given that the algorithm recovered 4 unknown tissue parameters. The success rate, in Fig. 4.21(a), remains unchanged for an overdetermined system of equations, increasing M from 4 to 6. Increasing the coupling information by decreasing sensor spacing to 2 mm improves the performance of the algorithm. A similar result was reported by Liauh *et al.* (1991) when trying to recover 2-D perfusion patterns.

The array-source distance was the dominant factor in determining the success of a reconstruction. Generally, as the array moves away from the source, at r=0, the reconstructed temperature profile degrades. However, for optimal

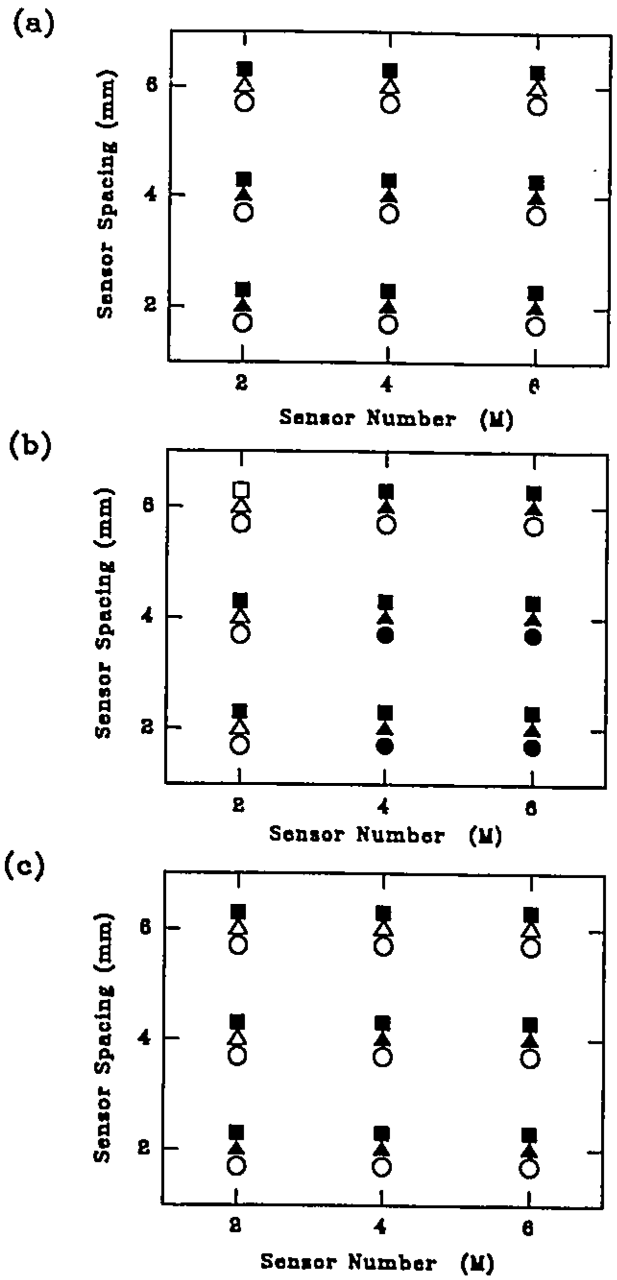

Figure 4.20. Success in reconstructing the true radial temperature profile as a function of temperature acquisition parameters (a) at 30 s, (b) 120 s and (c) 300 s. The symbols represent different array-source distances, 1 mm (□), 3 mm (△) and 5 mm (○). Filled symbols denote a successful reconstruction defined as a temperature error less than 1°C at all points in the thermal field.

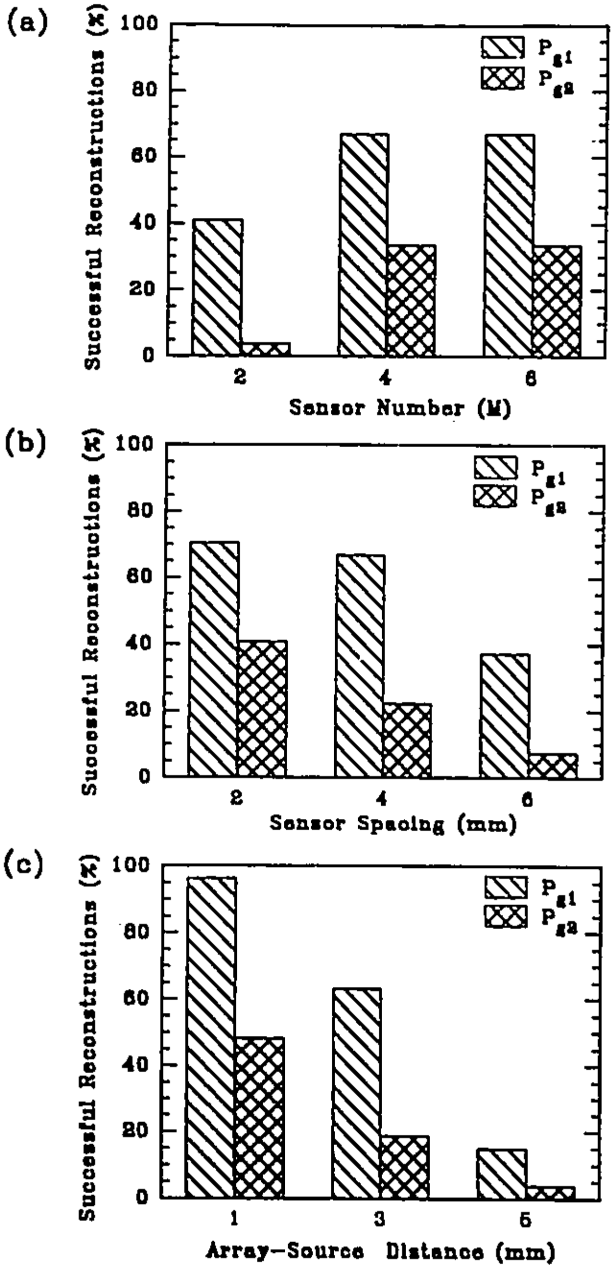

Figure 4.21. Success rates determined for each investigated choice of (a) sensor number (M), (b) sensor spacing and (c) array-source distance. Success rates for P_{g1} and P_{g2}, used to start the estimation algorithm, are presented.

array design, the reconstruction was successful for all array-source distances investigated. The systematic search for the optimal regularization parameter depended on the degree to which J^TJ was ill-conditioned. Stability was achieved in most instances for a λ of 0.001 added to diagonal elements of magnitude, 10^2 - 10^3.

To illustrate the algorithm's ability to recover the true biophysical properties, parameter estimates are shown in Figs. 4.22(a)-(d), as a function of iteration number, for optimal array design. Parameter estimates stabilize at the true values after 2 iterations when P_{g1} is used to start the algorithm. For P_{g2} the true parameters are recovered after 4 iterations. Functional reduction, shown in Fig. 4.22(e), is characteristic of a zero-finding algorithm.

Each reconstruction in Fig. 4.21 was believed to be good, as F was reduced to a least 10^{-4}°C^2, indicating that parameter estimates predicted the true temperatures at sensor locations. Failure, when it occurred, was at other locations, as illustrated in Fig. 4.23 for reconstructions at 30 s using P_{g2} . For sensors at 1, 3, 5 and 7 mm, temperatures were reconstructed identically. Increasing sensor spacing to 4 mm, such that sensors were at 1, 5, 9 and 15 mm, introduced a reconstruction temperature error between the first two sensors. Placing the sensors further from the source at 5, 7, 9 and 11 mm, degraded the reconstruction accuracy substantially between the source and the first sensor. For sensors at 3, 9, 15 and 21 mm, an error oscillation, crossed the origin at 3 mm and 9 mm, and was maximal, ~ 1.5°C, at 2 mm.

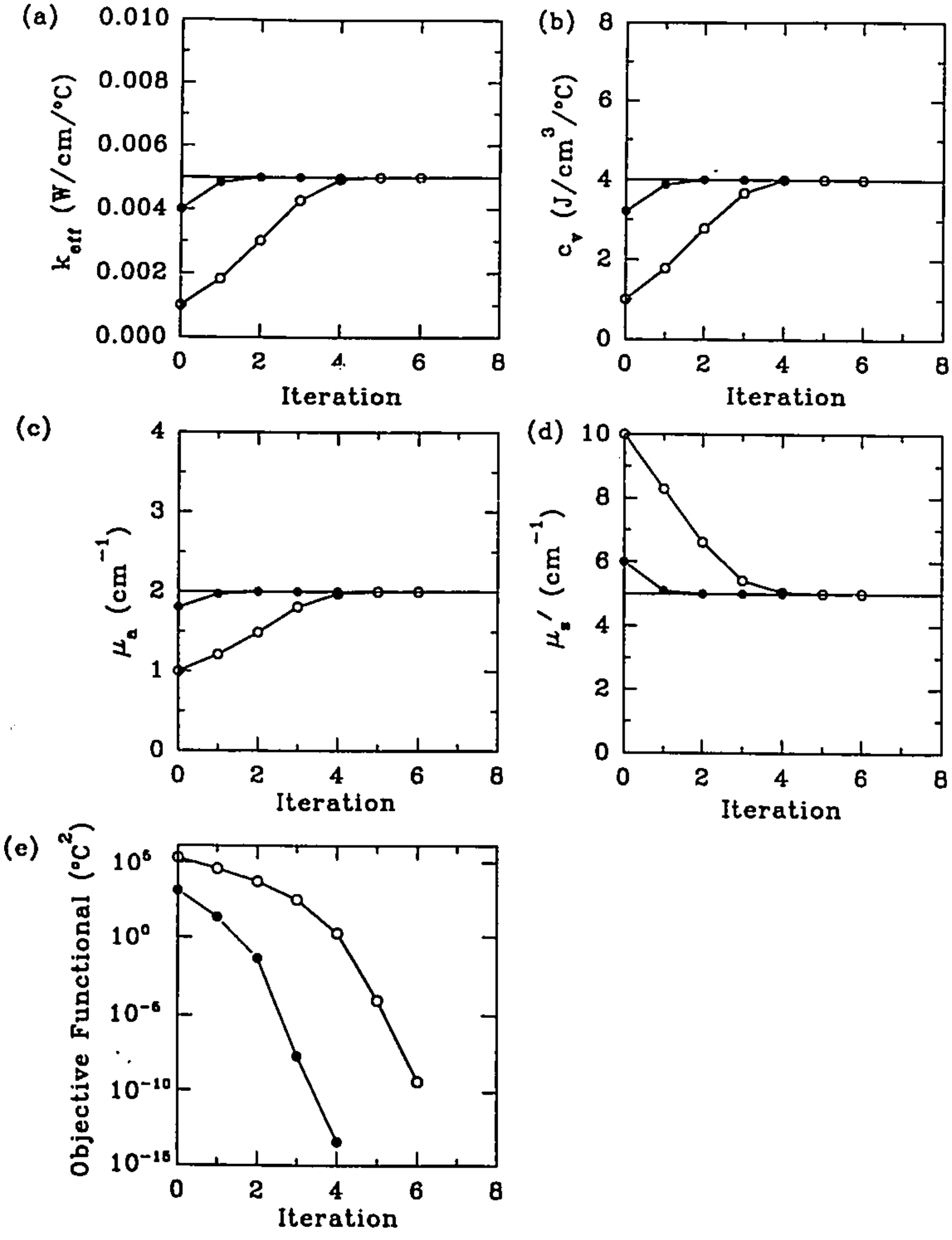

Figure 4.22. Values of (a) k_{eff}, (b) c_v, (c) μ_a, (d) μ_s' and (e) the objective functional as a function of iteration number for P_{g1} (●) and P_{g2} (○) reconstructions using optimal array design. The true parameter values are represented by the horizontal lines.

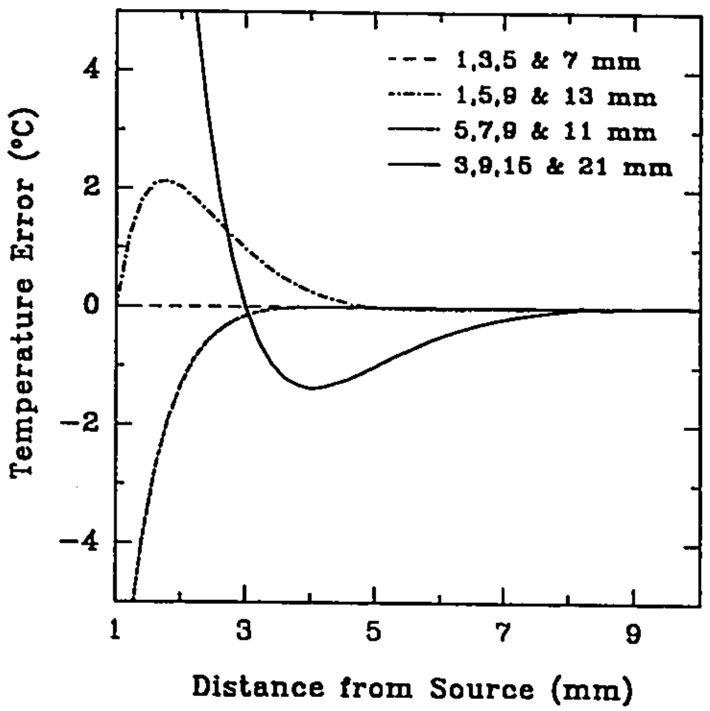

Figure 4.23. Radial temperature errors for reconstructions at 30 s, using P_{g2}, for different sensor arrangements.

Fig. 4.23 indicates that functional reduction, although necessary, is not a sufficient measure of reconstruction accuracy. Errors in Fig. 4.23 are small compared to the absolute true temperature increase, but they do demonstrate the potential for reconstruction errors which may be important when temperatures are reduced during hyperthermia applications.

4.4.1.2 Transient Temperature Sampling and Effect of Random Noise

During interstitial laser photocoagulation, temperature measurements from implanted sensors such as microthermocouples generally contain errors arising from thermal conduction smearing (Samulski et al. 1985), averaging over the finite sensor volume and uncertainty in sensor position (typically ± 1 mm). Near the source, large temperature gradients (100 -500°C/mm) potentiate all 3 types of errors. Temperature measurements can thus be highly inaccurate. Therefore, placing the sensor array 1 mm from the source may be clinically impractical. The algorithm was evaluated for more relevant array-source distances, 3-5 mm, using simulated noisy temperature measurements, generated using (3.4) with random noise added by sampling a normal distribution of mean zero and standard deviation σ=1°C.

Temperatures were reconstructed at an intermediate time of 120 s for 10 simulated noisy data sets with sensors at 3, 5, 7 and 9 mm or 5, 7, 9 and 11 mm. The number of transient samples was 1, 10 or 100, corresponding to sampling the sensor array every 30 s, 3 s or 0.3 s, respectively, in a time window from 90 s to

120 s. The initial parameter vector was $\mathbf{P}_{g2}$, to assess the performance of the algorithm for the more relevant case, when the initial guess parameter vector is far from the true values.

In a preliminary investigation the unconstrained routine found, in some instances, a minimum at nonsensical optical property values, resulting in a degraded reconstruction. In these instances, iterative estimates of μ_a and μ_s' approached zero or converged at $\mu_a > \mu_s'$. The known optical properties satisfy $\mu_a < \mu_s'$ cm^{-1}, a condition that exists in most soft tissues (Cheong et al. 1990). Therefore the reconstructions were repeated restricting the optical properties to obey this physical condition. Failure to meet this constraint prompted an increase in μ_s' given by $\mu_s' = \mu_a + \delta\mu_d$, where δ is a random number between 0 and 1 and μ_d, set to 5, is an empirical value based on reported differences between the optical coefficients in the near infrared for mammalian tissues.

This improved the performance of the algorithm. Reconstruction temperature errors for the constrained routine are shown in Figs. 4.24 and demonstrate that noise degrades the reconstruction but only substantially between the source and the first sensor in the array. Increasing S from 1 (t=120 s) to 100 (t=90.3, 90.6, 90.9,..., 120 s) reduced absolute temperature errors, effectively smoothing the noise, and shifted the errors from positive to negative. There was no significant improvement in the reconstruction accuracy on increasing M and S beyond 4 and 100, respectively. For noisy temperature measurements, reconstruction errors were minimized by sampling 4 sensors every 0.3 s,

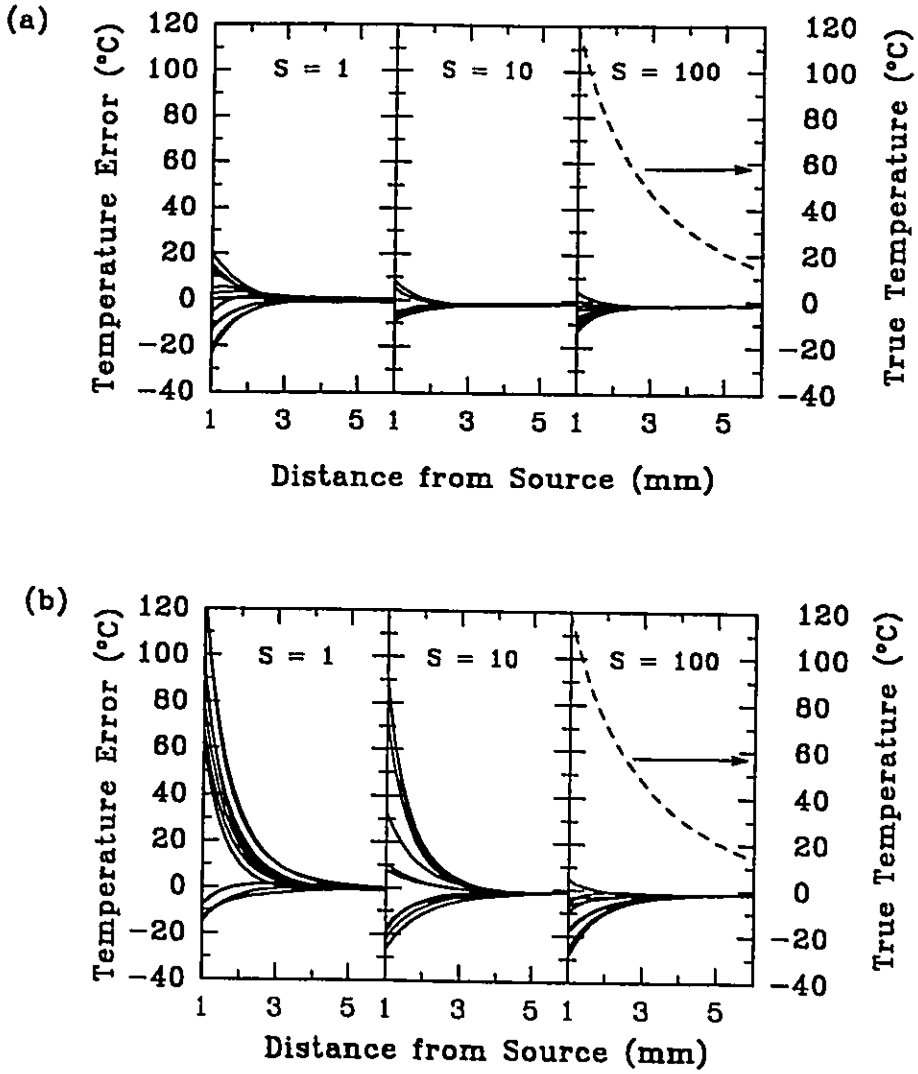

Figure 4.24. True temperature profile and radial temperature errors for reconstructions at 120 s as a function of the number of transient samples, S for (a) sensors at 3, 5, 7 and 9 mm and (b) sensors at 5, 7, 9 and 11 mm. Ten sets of random noise (σ = 1°C) were added to simulated temperatures to generate 10 measured noisy temperature data sets for reconstruction.

suggesting that reasonable reconstruction accuracy may require sampling of 10 Hz or greater. By increasing S from 10 to 100, there was a greater improvement in the reconstruction accuracy for sensors at 5, 7, 9 and 11 mm than that observed for sensors at 3, 5, 7 and 9 mm. This is likely a result of noise contributing more to measured temperatures at 11 mm than at 3 mm.

For noisy simulated temperature measurements, the optimal λ was, in most instances, 0.1 or 1, reducing the condition number of J^TJ by 2-6 orders of magnitude.

4.4.1.3 Accuracy of Parameter Estimates

The parameter estimates for the S=100 reconstructions in Fig. 4.24(a) are shown in Fig. 4.25. The estimated effective thermal conductivities and volumetric heat capacities, in Fig. 4.25, are all within 40% of the true values, except for trial 4 where deviations are ~ 80%. The estimated absorption and reduced scattering coefficients vary between -80% and 1000% of the true values, respectively. There was a predominant overestimation of k_{eff}, c_v and μ_s' and underestimation of μ_a. The observed large inter-trial variations confirm inherent ill-conditioning of the problem and indicate limited success of Levenberg-Marquardt regularization. In trials 4, 5 and 7, the large underestimation of μ_a accompanied by an overestimation of μ_s' is likely a result of optical similarity (Wyman et al. 1989), in which different sets of optical properties produce similar irradiance distributions.

The iterative changes in the parameter estimates for trials 3 and 4 are

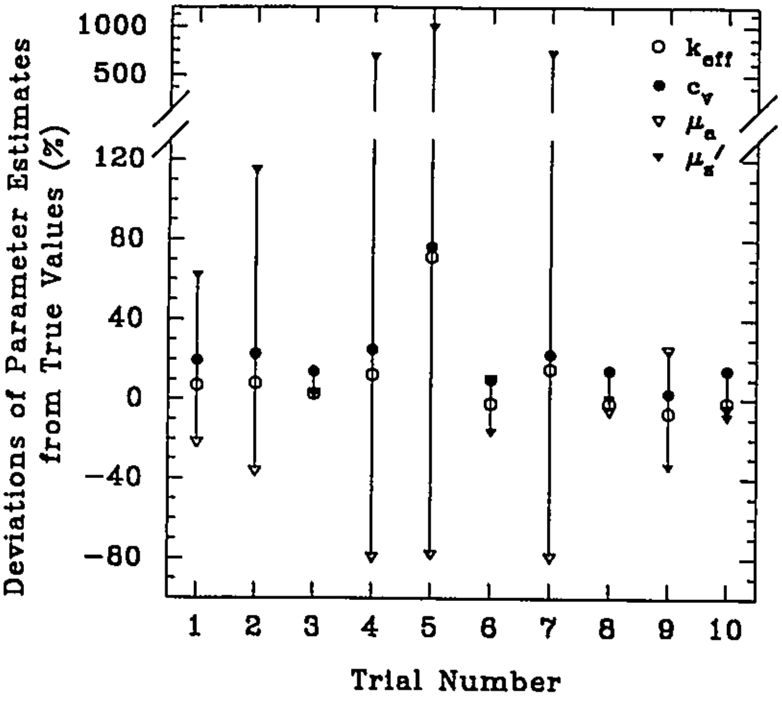

Figure 4.25. Parameter estimates obtained for the S = 100 reconstructions in Fig. 4.24(a).

shown in Fig. 4.26. In each trial the values of the thermophysical and optical properties stabilize after 5 iterations. In trial 3, the parameter estimates generally change in the desired direction with each iteration and stabilize to near the true values. However, in trial 4, we observe that after the first iteration, the estimates of the optical properties are further from the true values. This directional change continues, resulting in an overestimation of μ_s' and underestimation of μ_a. In trials 3 and 4, λ attained a maximum value of 10 and 0.01, respectively. The corresponding change in the objective functional, F, with iteration number is shown in Fig. 4.26(e). The functional for each trial is reduced by approximately four orders of magnitude, stabilizing at 5 iterations.

Remarkably, reconstructed temperatures and the true temperature profile, shown in Fig. 4.24(a), are in reasonable agreement, indicating that different sets of thermophysical and optical parameters can produce highly similar temperature distributions. Recently, a strong theoretical basis has been provided for this "optothermal similarity" (Wyman and Whelan 1994). Optothermal similarity appears to limit how accurately true parameters are recovered, without degrading substantially the reconstruction of temperatures. This suggests that the potential of multiple-parameter estimation to recover true tissue parameters is limited. Estimation of spatially dependent tissue parameters may introduce similarity within each parameter distribution, enhancing the difficulty of recovering true tissue parameters and possibly further reducing the accuracy of reconstructed temperatures.

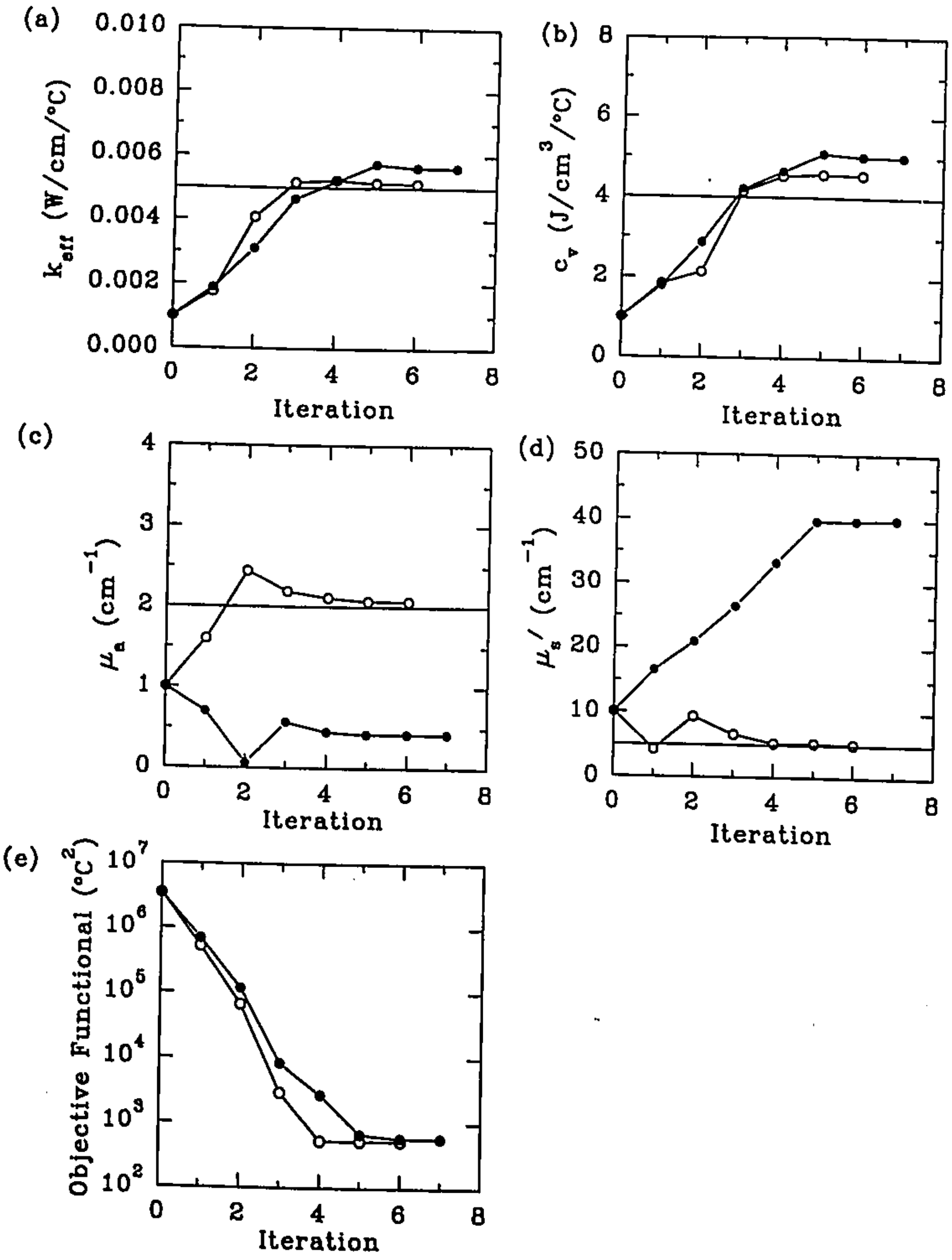

Figure 4.26. Values of (a) k_{eff}, (b) c_v, (c) μ_a, (d) μ_s' and (e) the objective functional as a function of iteration number for trials 3(O) and 4 (●) of the S = 100 reconstructions in Fig. 4.24(a). The true parameter values are represented by the horizontal lines.

The inability of the algorithm to recover true tissue parameters consistently can best be understood from sensitivity studies of temperature to variation in the parameters to be estimated. The sensitivity coefficients given by (2.29) describe how sensitive the temperature at radial distance, r, is to changes in each of the unknown tissue parameters. If sensitivity to a given parameter is large then there is a better chance that this parameter can be estimated accurately in inverse problems. Relative sensitivities, **P** dT(r,t)/d**P**, as a function of radial distance at 120 s for the true parameter vector, $\mathbf{P}_{true}$, in Table 4.5 are shown in Fig. 4.27.

Relative sensitivities for k_{eff}, c_v, μ_a and μ_s' are maximal at the source and decrease exponentially with increasing radial distance, except c_v which decreases almost linearly. This indicates that sensor location would likely affect strongly the algorithm's performance and explains the improvement in the reconstruction accuracy in Fig. 4.24 when sensors are placed closer to the source. The sensitivity for k_{eff} appears to be directly proportional to the absolute temperature increase, while that for c_v approaches a constant value near steady state. It is observed in Fig. 4.27 that sensitivity coefficients for k_{eff}, μ_a and μ_s' appear to be linearly dependent, making it difficult to obtain independent parameter estimates. Liauh and Roemer (1993) reported that linear dependence between blood perfusion patterns can exist, making accurate parameter estimation and complete temperature reconstruction difficult. This suggests that the potential of parameter estimation to recover true tissue parameters is limited.

Interestingly, the sensitivities for μ_a and k_{eff} change sign at ~ 5 mm and 7

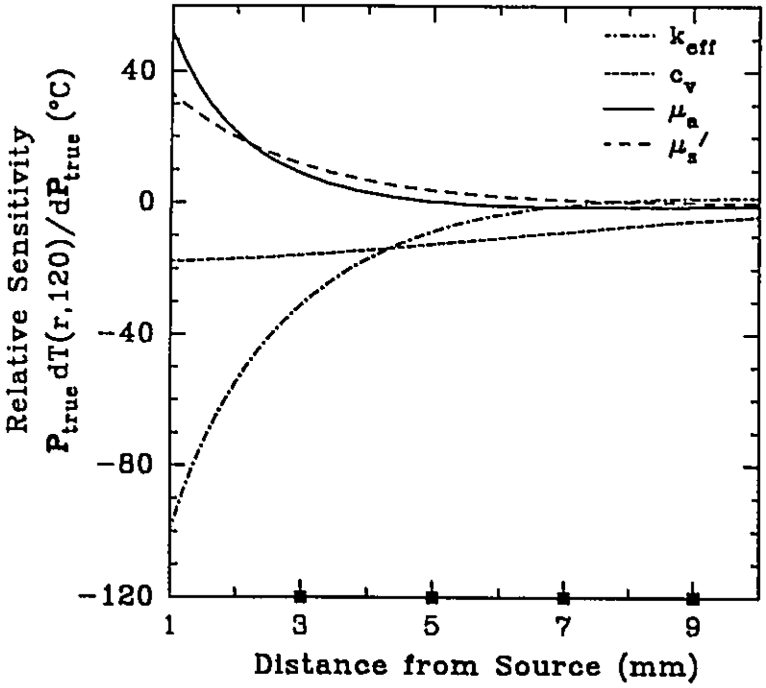

Figure 4.27. Relative radial parameter sensitivities at 120 s for the known parameter vector, P_{true}, from Table 4.5. ■ indicate sensor locations.

mm, respectively. A sensitivity coefficient changing sign indicates opposite directional changes for the parameter estimate within an iteration, which may degrade the reconstruction. Low parameter sensitivity in regions far from the source makes the problem ill-conditioned.

4.4.1.4 Sensor Placement Errors

An anticipated problem in on-line temperature reconstruction is the inaccurate knowledge of sensor positions when sensors are implanted percutaneously. Accurate sensor positioning requires uniform tissue collapse around the implanted sensor upon withdrawal of the insertion cannula. Position errors of ±1 mm can be routinely expected (Whelan et al. 1995). To assess the effect of systematic positioning errors on the reconstruction, the algorithm was evaluated with sensor placement errors, Δr_{err}, generating errors in the simulated temperature measurements according to $T^{s}_{err,m} = T^{s}_{meas,m} + \Delta r_{err} \, (dT^{s}_{meas,m}/dr)$. A positive placement error indicates that the sensor is further from the source than believed. The placement error is identical for all sensors in a linear array.

Sensor placement errors of ±0.5 mm were introduced into the simulated temperature measurements with $\mathbf{P}_{true}$ from Table 4.5. The resulting temperature reconstructions at 30 s and 300 s for sensors at 5, 7, 9 and 11 mm are shown in Fig. 4.28(a). The reconstructed temperature profile is an underestimate of the true temperature profile when the position error is positive (array further from source than believed) and an overestimate when the position error is negative. In all four

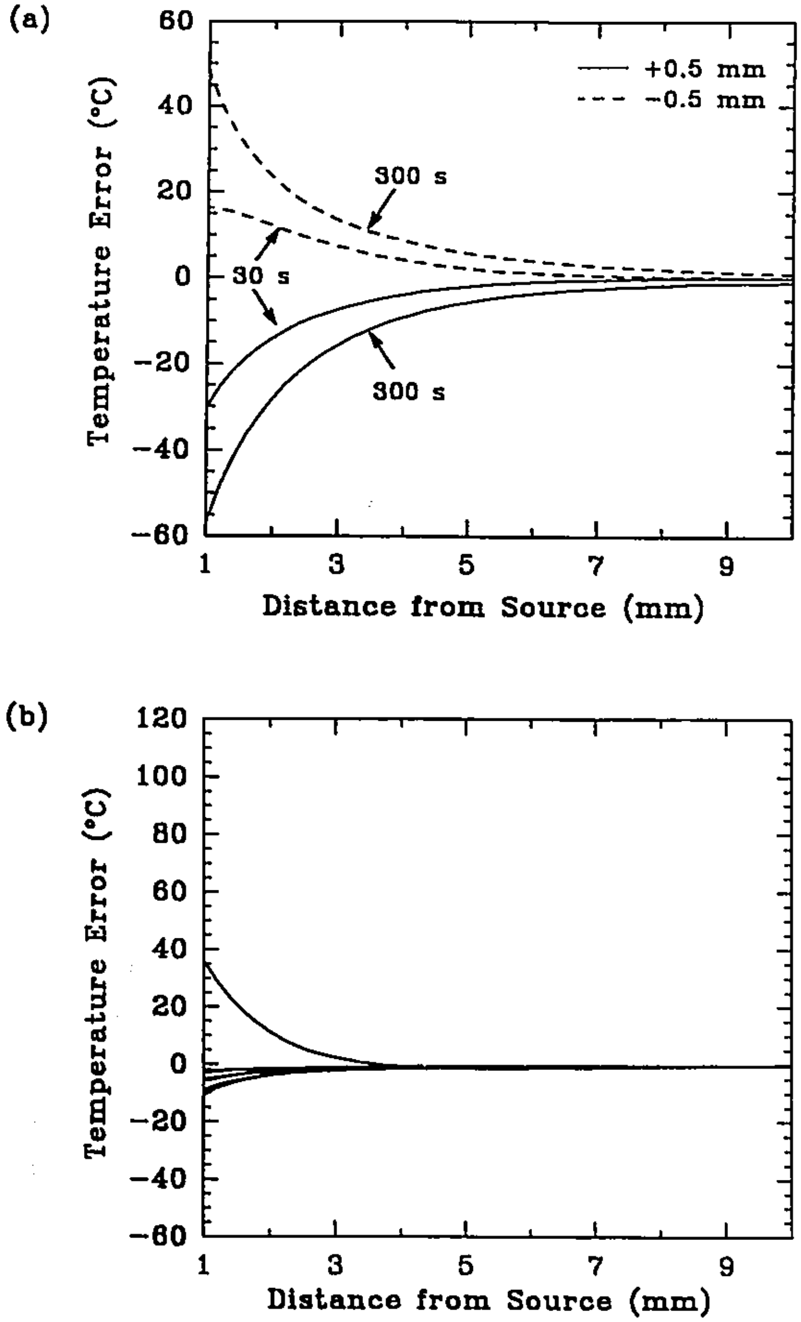

Figure 4.28. Radial temperature errors for reconstructions using P_{g2}, with sensors at 5, 7, 9 and 11 mm. (a) simulated temperature measurements contain sensor placement errors of $\Delta r_{err} = \pm 0.5$ mm, (b) simulated noisy ($\sigma = 1$°C) temperature measurements for ten known sets of randomly chosen biophysical parameters are reconstructed at 120 s.

reconstructions F was reduced to less than 10^{-1}°C^2, indicating that the algorithm accurately reconstructed the measured temperatures at sensor locations. Therefore reconstructed temperatures at the sensor locations were offset by amounts proportional to the local temperature gradient. Fig. 4.28(a) suggests that inaccurate knowledge of sensor placement is the principal cause of reconstruction degradation. However, in clinical practice, optical fiber(s) and sensor array(s) would likely be implanted parallel to each other such that sensor leads would be orthogonal to the induced thermal gradients and reconstruction degradation due to placement errors may be reduced.

4.4.1.5 Random Tissue Parameter Sets

The performance of the algorithm was evaluated for ten laser heating simulations, generated by randomly choosing tissue parameters from $0.005 \leq k_{eff} \leq 0.0175$ W/cm/°C, $3 \leq c_v \leq 4$ J/cm^3/°C, $0.2 \leq \mu_a \leq 2.0$ cm^{-1} and $2 \leq \mu_s' \leq 10$ cm^{-1}, valid for mammalian tissues irradiated by 1064 nm optical energy. The upper limit of k_{eff} was based on the contribution of blood perfusion to the effective thermal conductivity being 1-3.5 times the true thermal conductivity (Weinbaum and Jiji 1985), which for mammalian tissues is ~ 0.005 W/cm/°C (Duck 1990). Simulated temperature measurements with added random noise were generated from sensors at clinically relevant distances of 5, 7, 9 and 11 mm with S = 100 (s=90.3, 90.6, 90.9,..., 120 s). The reconstructed radial temperature errors using $\mathbf{P}_{g2}$ are presented in Fig. 4.28(b). For 9 of the 10 parameter sets where the absolute temperature range at 1 mm is less than 100°C, reconstructed temperatures underestimate true temperatures but remain within 11°C (15%) and 1°C of the true temperatures at 1 mm and $r \geq 3$ mm, respectively. Fig. 4.28(b) indicates that accurate temperature reconstruction may be achievable within a limited distance from the first sensor at 5 mm towards the source.

Temperature induced modifications of the thermophysical and optical properties, not considered to this point, would produce higher thermal gradients near the source. Modelling spatially and temporally varying biophysical properties requires a numerical approach and is considered in the next section.

4.4.2 1-D Inhomogeneous Test Cases

4.4.2.1 Static Tissue Discretization

In this section we investigate the capability of the estimation algorithm to reconstruct temperatures during simulated ILP in tissues when the biophysical properties to be estimated are discretized into spatial parameter zones. Simulated measured temperature data, for a 300 s irradiation at 2.0 W, were generated by solving the finite difference expressions, (3.9) and (3.10), for a sphere of radius 24 mm with 0.25 mm node spacing and a 5 s temporal step. A single parameter zone (homogeneous case) was assumed with biophysical properties given by $\mathbf{P}_{true}$ in Table 4.5. By contrast, the number of parameter zones in the estimation algorithm was varied to investigate the effect of spatial discretization on the parameter estimates and temperature reconstruction accuracy. In other words, given a homogeneous medium, can reconstructing based on discrete parameter zones introduce errors into the reconstruction? The tissue was discretized into 8, 4, or 2 static parameter zones as shown in Fig. 4.29. Thus each biophysical property to be estimated was represented by a Z-component vector (see section 2.4).

Considering the optimization data from section 4.4.1.1 and clinical practicality, transient temperature profiles were reconstructed at 30 s intervals using a simulated 4 sensor array with sensors at either 3, 5, 7 and 9 mm or 5, 7, 9 and 11 mm from the optical source. Simulated temperature measurements were noiseless. Sensors were sampled every 3 s (S=10). The order of magnitude initial guess parameter vector, P_{g2}, from Table 4.5 was used to start the algorithm.

Reconstructions for a 2 zone model were successful for each array-source distance investigated (data not shown). The true temperature distribution and reconstructed temperature errors for 4 and 8 zone models are shown in Fig. 4.30. With sensors at 3, 5, 7 and 9 mm, the reconstructions are accurate for the 4 zone model, Fig. 4.30(b). However, for the 8 zone model, Fig. 4.30(c), the reconstructions are a slight overestimation of the true temperatures at $r \leq 3$ mm. Reconstructions are degraded for both 4 and 8 zone models with sensors at 5, 7, 9 and 11 mm, shown in Fig. 4.30(d) and (e), respectively. The substantial reconstruction error at $r \leq 3$ mm in Fig. 4.30(e) is due to the absence of temperature sampling in zone 1.

It is observed in Fig. 4.30(e) that reconstruction errors shift from positive to negative during the simulation. This may be explained in terms of the

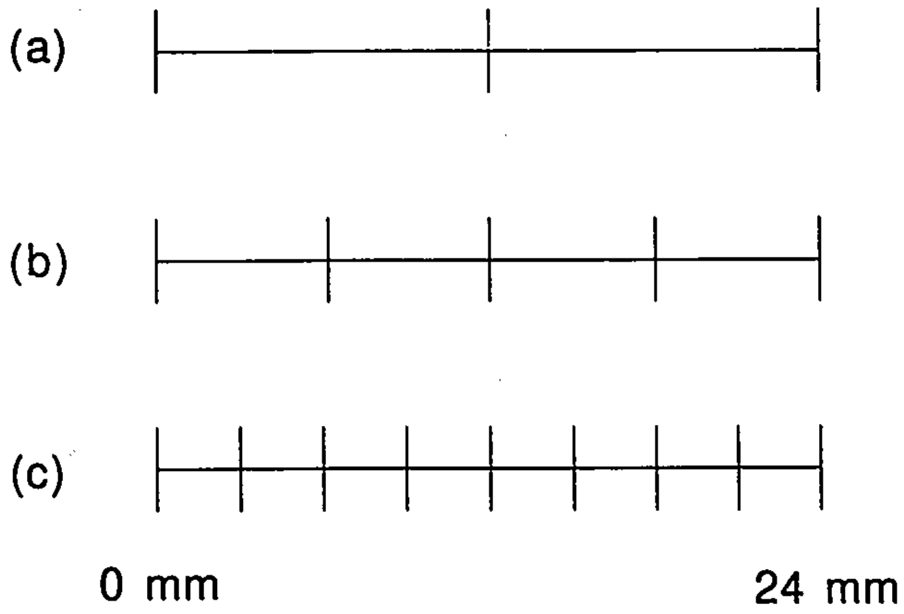

Figure 4.29. Static tissue discretization scheme. The number of spatial parameter zones, Z, is (a) 2, (b) 4 or (c) 8.

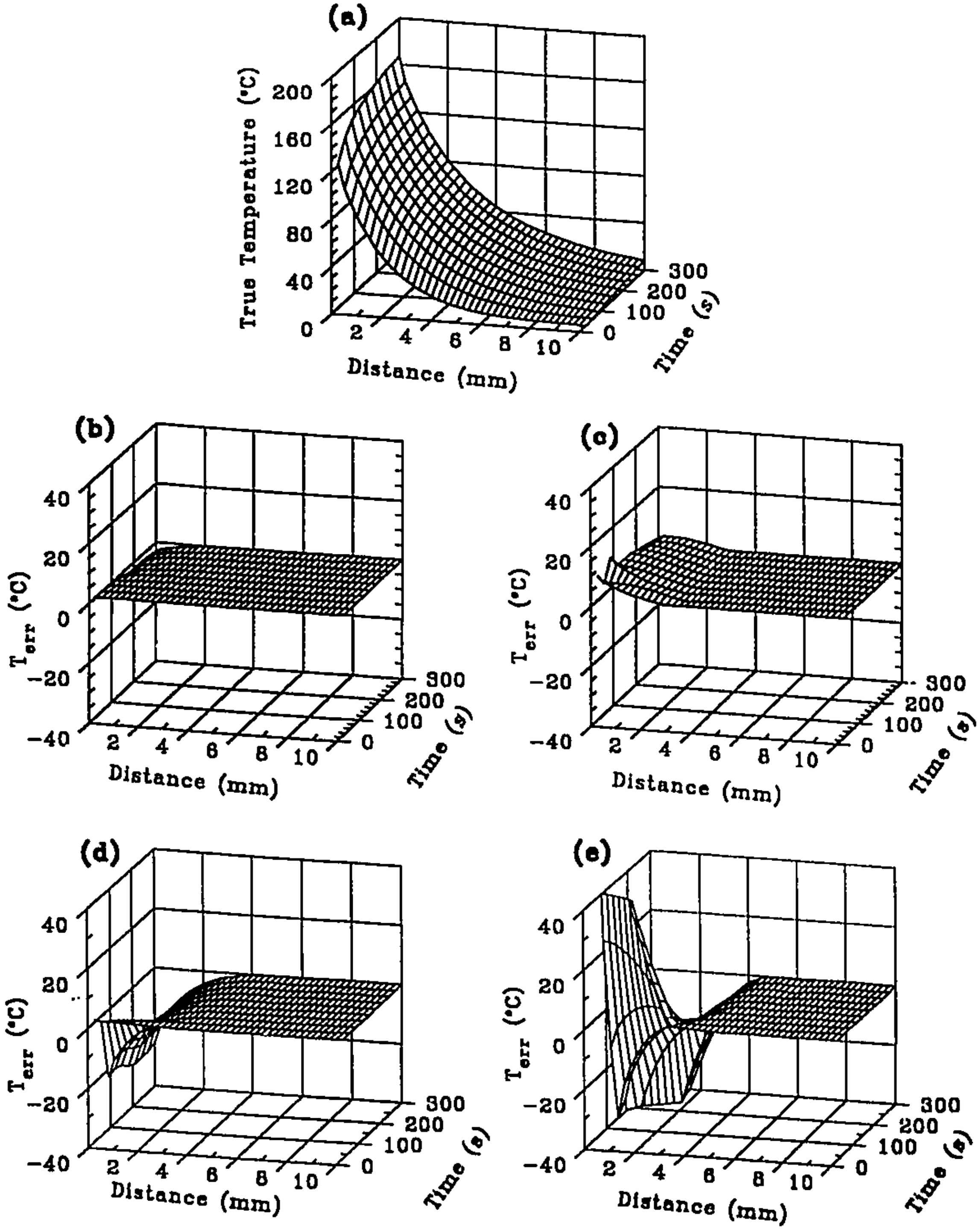

Figure 4.30. (a) True radial temperature profiles at 30 s intervals for a 300 s irradiation at 2.0 W. Reconstructed radial temperature errors at 30 s intervals for sensors at 3, 5, 7 and 9 mm (b) 4 zone model and (c) 8 zone model. Reconstructed radial temperature errors at 30 s intervals for sensors at 5, 7, 9 and 11 mm (d) 4 zone model and (e) 8 zone model.

relationship between solutions for successive reconstructions. In the estimation algorithm, the reconstructed temperature profile at time, t (30 s, 60 s, 120 s, ..., 300 s), is the initial temperature profile for the next 30 s time interval. Thus reconstructed temperature errors can influence subsequent transient temperature calculations. However, the initial guess parameter vector for each transient reconstruction was always $\mathbf{P}_{g2}$. This prevented the algorithm from converging to a similar solution for each reconstruction. Therefore, Fig. 4.30 suggests that the estimation algorithm attempts to correct for errors in the initial temperature profile.

To illustrate the recovery of the biophysical properties, parameter estimates for the 2, 4 and 8 zone model reconstructions at 30 s with sensors at 3, 5, 7 and 9 mm are shown in Fig. 4.31. The estimated biophysical parameters are spatially distributed, with the distribution depending on the number of parameter zones modelled. Generally, estimates for k_{eff} and c_v agree with the true values in the zones containing sensors. The estimates for μ_a and μ_s' converged near the initial values which differ substantially from the true homogeneous values. However, the temperature errors at 30 s in Figs. 4.30(b) and (c) are minimal, indicating that true and reconstructed temperature profiles are highly similar.

Estimates for k_{eff} and c_v at 30 s for the 8 zone model as a function of array position are shown in Fig. 4.32. Clearly, with temperature sampling in the first zone, $r \leq 3.125$ mm, parameter estimates in this zone are improved. For sensors at 5, 7, 9 and 11 mm, the parameter estimates in the first zone remain near the initial

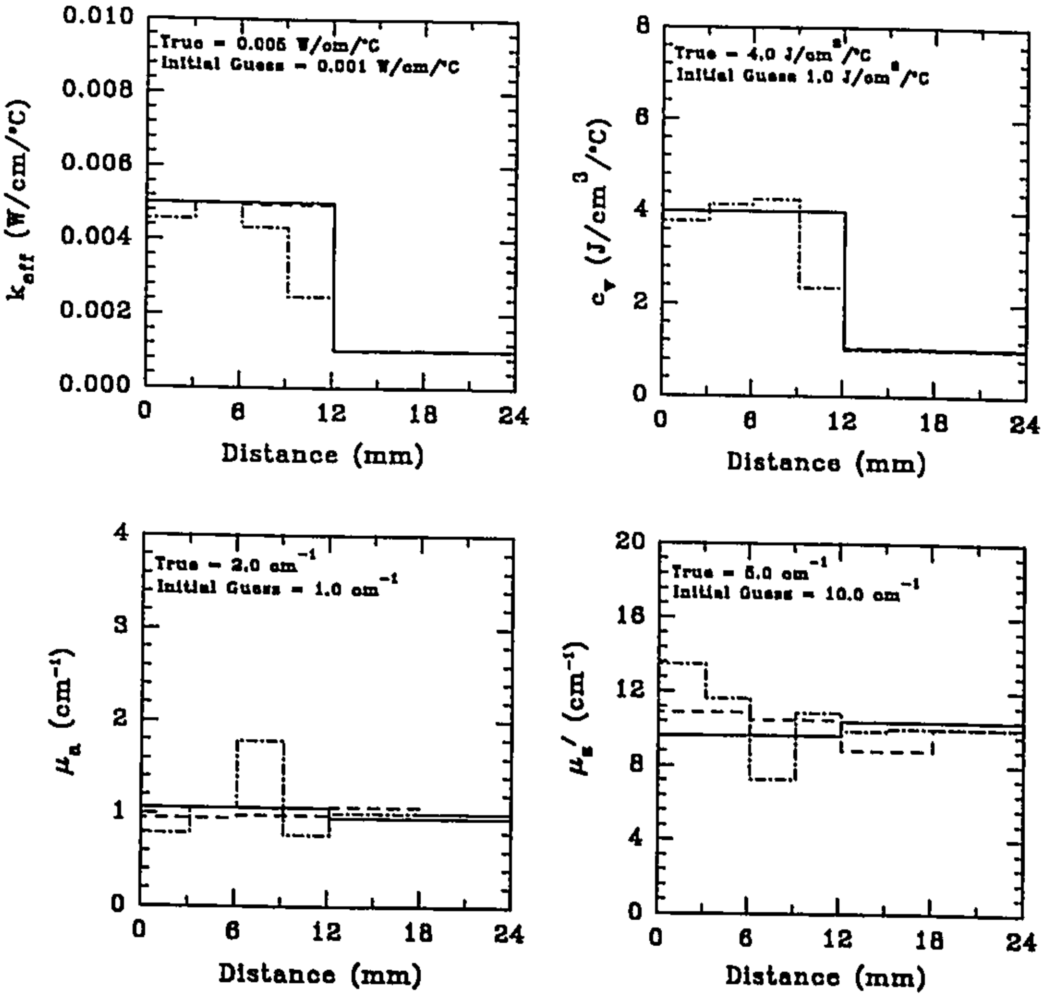

Figure 4.31. Values of the estimated thermophysical and optical properties at 30 s for 2 zone (——), 4 zone (--) and 8 zone (-·-) reconstruction with simulated sensors at 3, 5, 7 and 9 mm.

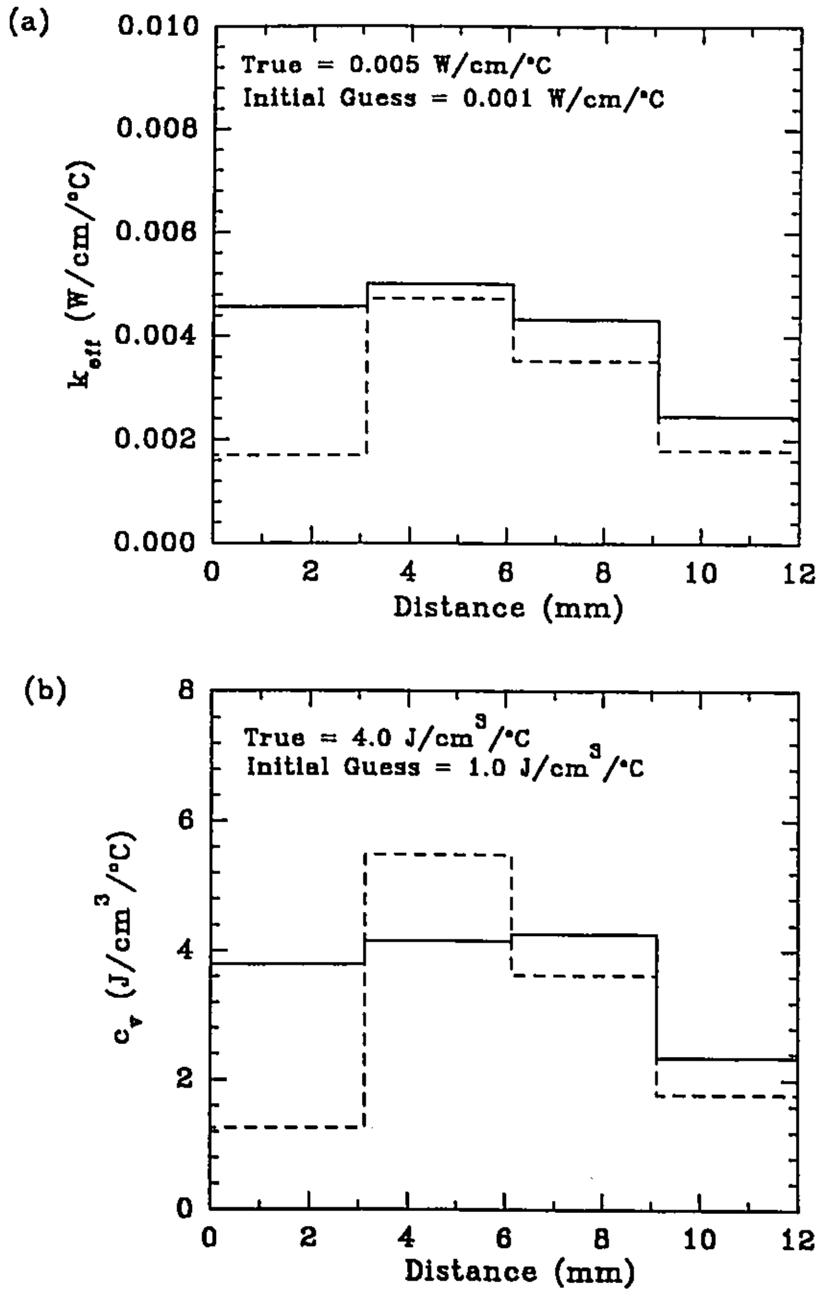

Figure 4.32. Values of the estimated thermophysical properties at 30 s for 8 zone reconstruction with simulated sensors at 3, 5, 7 and 9 mm (—) or at 5, 7, 9 and 11 mm (--). Only 4 of 8 zones are shown.

values.

The k_{eff} and c_v estimates at $r \geq 12$ mm in Fig. 4.31 remained at initial values without degrading the reconstruction. This was observed in each of the transient reconstructions up to 300 s. This is likely a result of reduced parameter sensitivity and small absolute temperatures (in this case $T(r \geq 12 \text{ mm}) < 5°C$), such that the elements of the Jacobian matrix for z=5-8 (r=12-24 mm) are effectively zero. This indicates that the region of tissue where knowledge of the biophysical properties is important depends on the induced temperature distribution and, for single fiber ILP, may be limited to ~ 10 mm from the source. For multiple-fiber ILP, larger volumes of tissue are heated and it may be necessary to extend parameter estimation to larger regions of tissue.

Relative sensitivities at 30 s for the 8 zone model as a function of radial distance for the true parameter vector, $\mathbf{P}_{true}$, in Table 4.5 are shown in Fig. 4.33. Radial sensitivity distributions in Fig. 4.33 describe how sensitive radial temperatures at 30 s are to a 0.1% parameter change in zone, z, during transient temperature calculations from 0 - 30 s. Relative sensitivity distributions for zone 1 (0-3.125 mm) parameters $k_{eff}^{z=1}$, $\mu_a^{z=1}$ and $\mu_s'^{z=1}$, Fig. 4.33(a), are maximal at the source and decrease exponentially with increasing radial distance, such that there is an order of magnitude reduction at the interface. This indicates that zone 1 temperature sampling would be required to estimate accurately the zone 1 parameters and explains the results shown in Fig. 4.32.

Relative sensitivity distributions for zone 2 (3.125-6.125 mm) parameters,

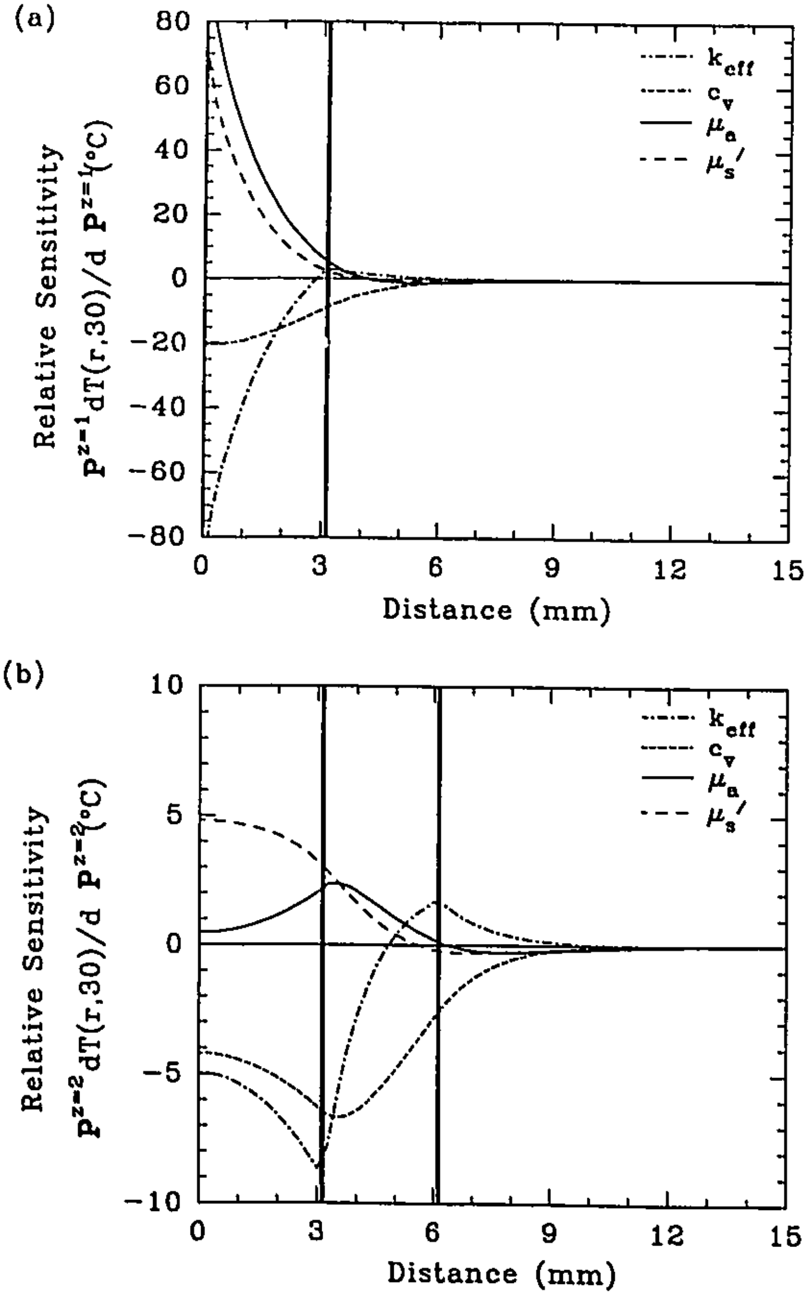

Figure 4.33. Relative radial parameter sensitivities at 30 s for (a) zone 1 (0-3.125 mm) parameters and (b) zone 2 (3.125-6.125 mm) parameters, based on the 8 zone model. The true parameter vector in Table 4.5 was used to generate these sensitivity distributions.

Fig. 4.33(b), are structure-rich and are markedly different from those for zone 1 parameters. It is observed that the effect on temperature profiles of zone 1 parameter changes is more substantial than zone 2 parameter changes. This is a result of the exponential decrease in the optical irradiance and corresponding heat generation rate with increasing radial distance. The penetration depth for the optical properties modelled is ~ 2 mm, such that in zone 2 the irradiance is reduced substantially.

Interestingly, sensitivities for zone 2 parameters $k_{eff}^{z=2}$ and $\mu_s'^{z=2}$ are maximal in zone 1. In addition, $k_{eff}^{z=2}$ and $\mu_s'^{z=2}$ sensitivities change sign within zone 2 at ~ 5.0 and 5.5 mm, respectively. Thus, there is the potential for sensitivities to be zero at sensor locations, thereby contributing no information to the estimation algorithm. These observations indicate that temperature sampling in the first zone is required and suggests that placing a sensor in each parameter zone is not necessarily optimal. However, in hyperthermia simulations when the temperature field is approximately uniform, temperature sampling in each zone has been shown to be optimal for the recovery of perfusion patterns (Liauh et al. 1991). Relative sensitivities for parameter changes in zones 3-8 are similar in shape to those in Fig. 4.33(b) but reduced in magnitude.

Fig. 4.33 indicates that the number of parameter zones affects the magnitude of sensitivity coefficients at sensor locations and therefore influences the solution. Furthermore, it suggests that optimal sensor location would be at or near the interface between zones.

Static discretization, although instructive, would not be suitable for ILP due to the induced transient coagulation boundary and its associated increase in optical scattering. Clearly, a better approach would be to discretize the tissue according to some physical description of the temperature induced modifications of the thermophysical and optical properties.

4.4.2.2 Dynamic Tissue Discretization

In this section the effects of coagulation and tissue water vaporization on temperature distributions are incorporated into the forward and inverse simulations in order to predict how successful the reconstruction system might be for practical applications. Tissue discretization is based on our description of coagulation and tissue water vaporization (see section 3.3). Interfaces between zones are determined by $R_{vapr}(t)$ and $R_{coag}(t)$ corresponding to radial distances where the model-predicted temperatures are 100°C and 60°C, respectively. Thus, the number of parameter zones is now a dynamic quantity, Z(t), as shown in Fig. 4.34. A Z(t)=1 is the initial homogeneous case, Z(t)=2 indicates that coagulation has occurred and Z(t)=3 indicates that water vaporization has occurred. In generating measured temperature data (forward simulations), values of $R_{vapr}(t)$ and $R_{coag}(t)$ can be updated at any user defined time interval during transient temperature calculations. By contrast, in the estimation algorithm (inverse simulations), estimates of $R_{vapr}(t)$ and $R_{coag}(t)$ are updated only at each reconstruction time and determine the number and location of spatial parameter

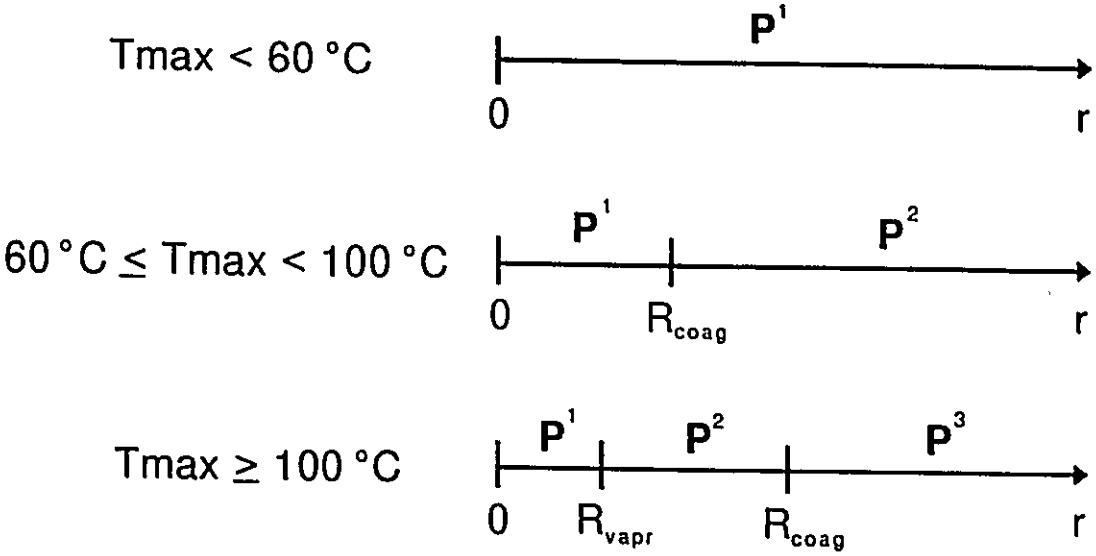

Figure 4.34. Dynamic tissue discretization scheme based on the description of coagulation and water vaporization in section 3.3. The number of spatial parameter zones, Z(t), varies from 1-3 as determined by the maximum tissue temperature, T_{max}.

zones for the next reconstruction interval (see Fig. 3.7). Thus, within a reconstruction interval, the spatial discretization is constant. However, in generating the measured temperature data the true interfaces (spatial discretization) may vary during a reconstruction interval. This introduces a systematic error into the estimation algorithm. The magnitude of this error would most likely depend on the length of the reconstruction interval.

The effect of this systematic error on the performance of the algorithm is demonstrated by reconstructing a simulated ILP test case in bovine muscle using different reconstruction intervals. Initially, the irradiation parameters were chosen such that the maximum tissue temperature was less than 100°C (no water vaporization, $R_{vapr}(t \geq 0) = 0$). Simulated measured temperature data were generated as in section 4.4.2.1 for a 120 s irradiation at 1.0 W using biophysical properties for bovine muscle given in Table 4.6. A threefold increase in μ_s' at $r \leq R_{coag}(t)$ was assumed, with all other biophysical properties remaining at the values in Table 4.6. The ambient temperature was 37°C. In the simulated measured temperature data, $R_{coag}(t)$ was updated every 1 s and is shown in Fig. 4.35. For the simulated ILP test case, the onset of coagulation occurs at 32 s with $R_{coag}(120\ s)=1.85$ mm. The reconstruction interval, Δt_{rec} was 1 s, 10 s or 30 s corresponding to 120, 12 or 4 reconstructions during the irradiation. The simulated sensor array consisted of 20 sensors placed at each node in the finite difference temperature calculating mesh (0.1 mm sensor spacing) from 0.1 mm to 2.0 mm. This ensured that the effect of the systematic error could be isolated from

Table 4.6. True and two initial guess parameter vectors used, respectively, to generate simulated temperature measurements and start the parameter estimation algorithm. True biophysical properties are valid for bovine muscle irradiated by 1064 nm optical energy.

	$\mathbf{P}_{true}$	$\mathbf{P}_{go}$	$\mathbf{P}_{ge}$
Effective thermal conductivity, (W/cm/°C)	5.5E-3	1.0E-3	5.0E-3
Volumetric heat capacity, (J/cm^3/°C)	3.8	1.0	4.0
Absorption coefficient, (cm^{-1})	1.2	1.0	2.0
Reduced scattering coefficient, (cm^{-1})	2.8	10.0	5.0

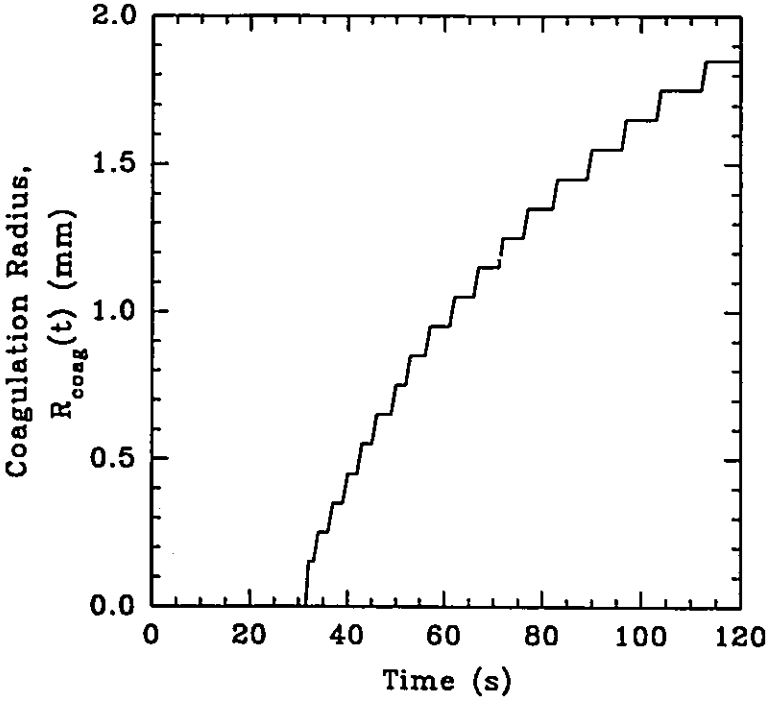

Figure 4.35. Predicted coagulation radius in bovine muscle for a 120 s irradiation of 1.0 W at 1064 nm.

all possible sources of error such as reduced parameter sensitivity. Furthermore, the placement of the simulated sensor array allows for the objective functional to be a good measure of reconstruction accuracy, in contrast to the case when sensors are far from the source as discussed in section 4.4.1.1. The algorithm began with the initial "order of magnitude" guess parameter vector, $\mathbf{P}_{g,v}$ in Table 4.6.

We define F^*, a subset of F, as the sum of the square of the errors between measured and predicted temperatures at sensor locations at the reconstruction time. When sampling sensors only at the reconstruction time (S=1), $F^* = F$. Values of F^* as a function of reconstruction interval and sensor sampling are shown in Fig. 4.36. The increase in F^* at 33 s, 40 s and 60 s in Figs 4.36(a), (b) and (c), respectively, is a result of a mismatch between the model used to generate the measured data ($R_{coag}(t) > 0$, $Z(t)=2$) and the model in the estimation algorithm ($R_{coag}(t) = 0$, $Z(t)=1$) for the reconstruction interval. The maximum F^* increases by ~ 2 orders of magnitude as Δt_{rec} increases from 1 s to 30 s. For S=1, the algorithm's performance improves at the next reconstruction interval, converging to the global minimum.

Interestingly, in Figs. 4.36(b) and (c), the reconstruction is generally better for S=1 than S=2 or 10 at and following the model mismatch interval. For multiple sampling, parameter fits are essentially average values over Δt_{rec}. Such averaging limits the reconstruction of temperature transients, in this case, caused by a coagulation-induced increase in optical scattering. Degradation due to multiple

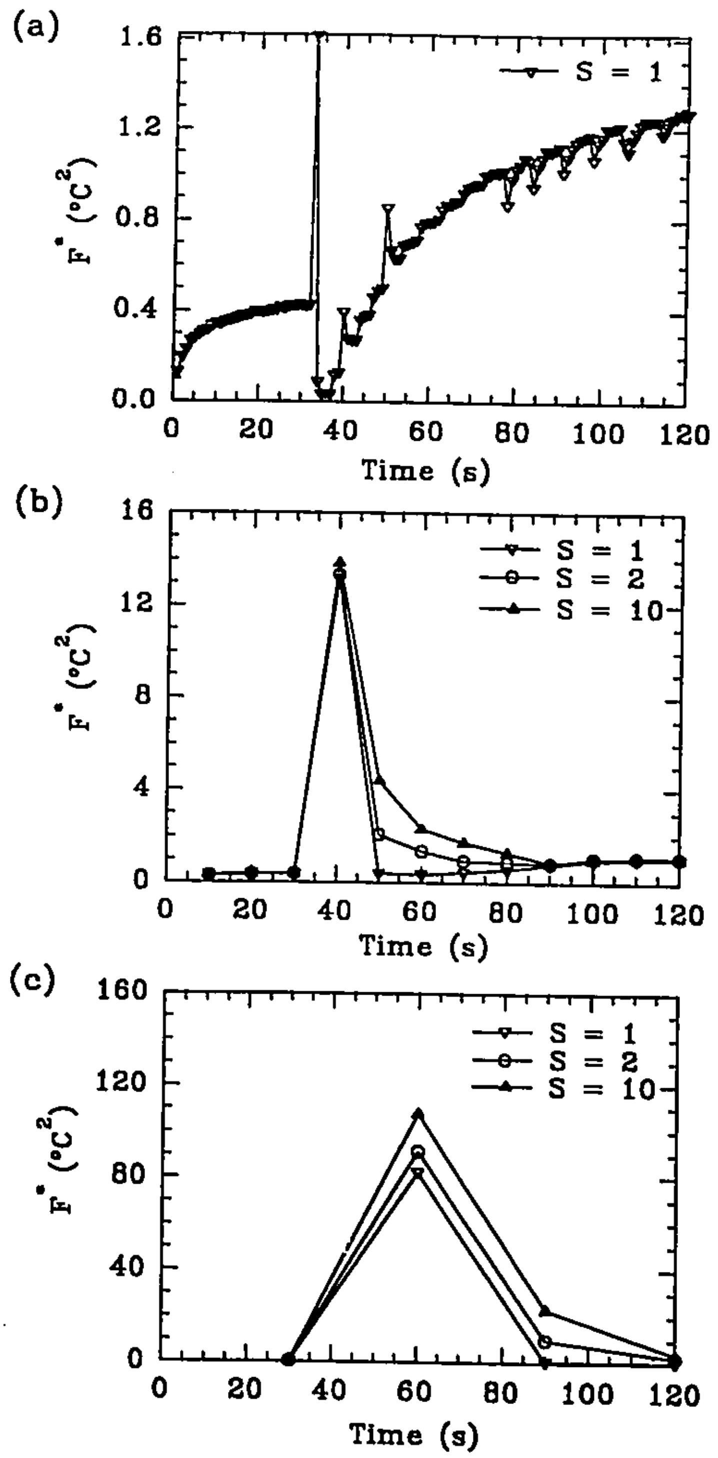

Figure 4.36. Values of F^{*} as a function of sensor sampling for the simulated irradiation in bovine muscle depicted in Fig. 4.35. The reconstruction time interval, Δt_{rec}, is (a) 1 s, (b) 10 s and (c) 30 s.

sampling is more pronounced for longer reconstruction intervals. These results indicate that for dynamic parameter estimation, the reconstruction interval should be less than 30 s. Furthermore, the $R_{coag}(t)$ profiles in Fig. 4.3(a) (*in vivo* liver simulation) and Fig. 4.35 (*ex vivo* bovine simulation) suggest using short reconstruction intervals early in the irradiation during rapid coagulation transients and longer intervals as the coagulation boundary approaches steady state.

To illustrate the performance of the dynamic estimation algorithm for "practical" reconstruction conditions, temperatures are reconstructed using sensors at 5, 7, 9 and 11 mm. Reconstructed radial temperature errors at 30 s for S=1 as a function of Δt_{rec} are shown in Fig. 4.37. A Δt_{rec} of 1 s, 10 s and 30 s corresponds to 30, 3 and 1 reconstruction(s) from 0 to 30 s. For Δt_{rec}= 1 s and 10 s the parameter sensitivities at the first sensor (5 mm) at 1 s and 10 s (the first reconstruction in each case), respectively, are small due to temperature increases of only 0.09°C and 0.97°C, respectively. This combined with an initial guess far from the true values results in a substantial overestimation of temperatures. Moreover, the algorithm-predicted onset of coagulation ($R_{coag}(t) > 0$) was 4 s and 20 s for Δt_{rec} of 1 s and 10 s, respectively, such that Z=2 in the estimation algorithm before the true onset at 33 s (see Fig. 4.35).

For Δt_{rec}=30 s the temperature profile is accurately reconstructed. This is a result of Z=1 in the estimation algorithm at 30 s (the first reconstruction in this case) being consistent with the simulated measured temperature data at 30 s. In addition, the temperature increase at the first sensor (5 mm) at 30 s was 3.01°C.

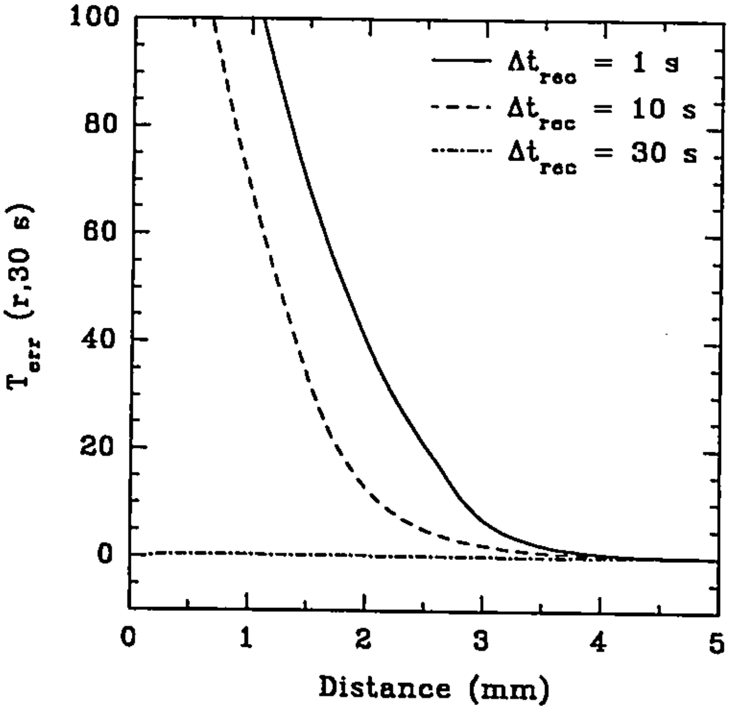

Figure 4.37. Reconstructed radial temperature errors at 30 s for S=1 as a function of Δt_{rec}.

These observations indicate that short reconstruction intervals < 10 s early in the irradiation may lead to poor reconstructions if minimal temperature increases are reported by sensors. Thus, the optimal reconstruction system would rely on temperature feedback to determine the length of the first reconstruction interval.

Fig. 4.36 indicates that the performance of the dynamic algorithm improves as Δt_{rec} is reduced. However, a small Δt_{rec} may lead to poor reconstructions early in the irradiation as shown in Fig. 4.37. Therefore, we consider a reconstruction scheme with an initial 30 s interval followed by 10 s intervals such that temperature profiles are reconstructed at 30, 40, 50, 60,...110 and 120 s. The effect of sensor sampling on reconstruction accuracy is also investigated. The true temperature increase and reconstructed radial temperature errors as a function of sensor sampling are shown in Fig. 4.38. Not surprisingly, the temperature profile at 30 s is accurately reconstructed for each sampling case. Generally, for S=1 and 10, reconstruction errors are in the same direction. However, for S=100, errors change direction, a result of the algorithm attempting to compensate for the errors in the reconstruction at a previous interval. In Figs. 4.38(b)-(d), reconstruction errors fall to near zero at the algorithm-predicted $R_{coag}(t)$ and define zones 1 and 2 in the estimation algorithm. As sensor sampling is increased, reconstructed temperature errors are reduced but remain substantial for S=100 due to the combination of reduced sensitivity at sensors for zone 1 parameters and an initial guess far from the true values.

The ability of the dynamic algorithm to resolve the true coagulation

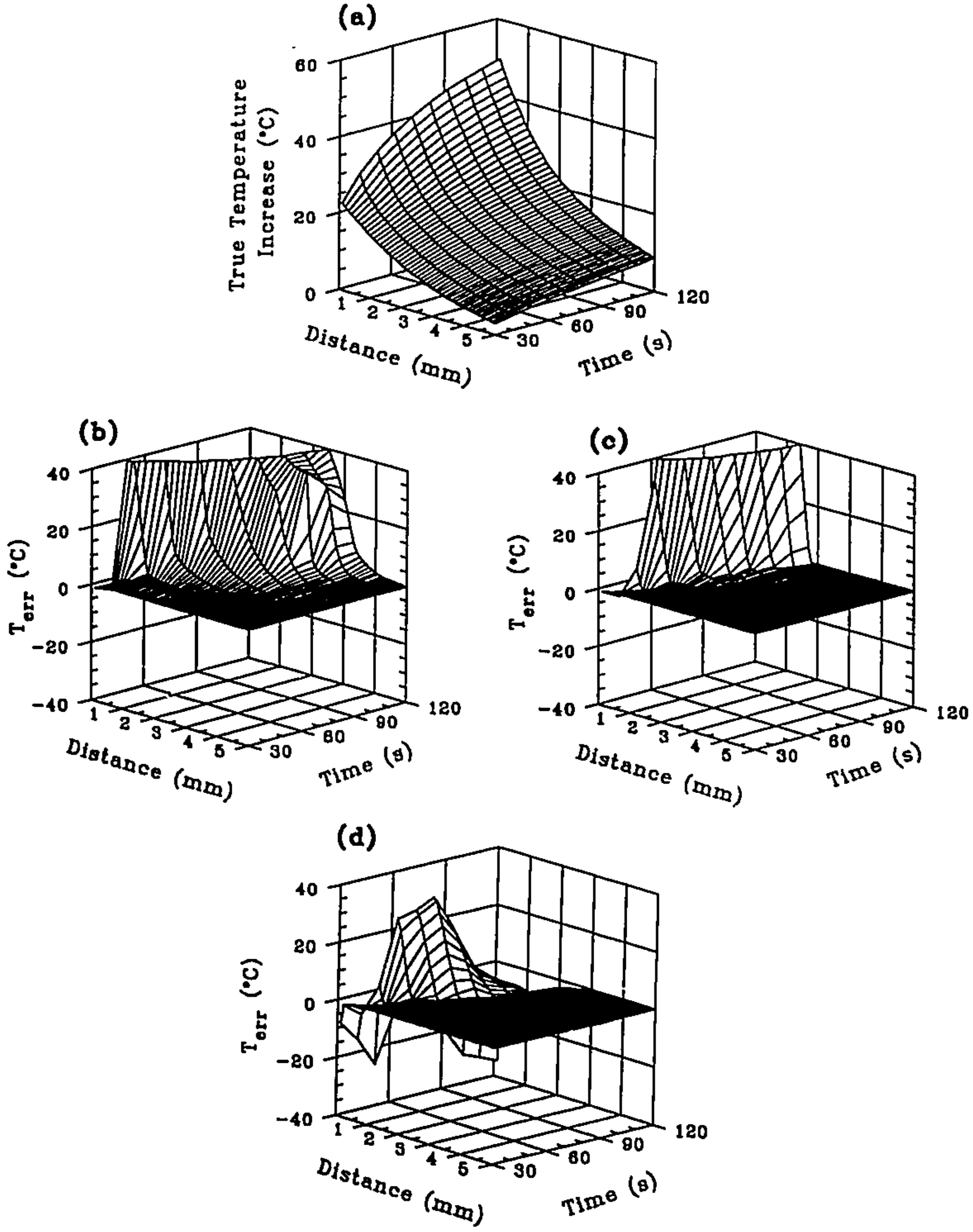

Figure 4.38. (a) True radial temperature profiles for a simulated ILP test case (120 s irradiation at 1.0 W). Reconstructed radial temperature errors at 30 s followed by 10 s reconstruction intervals as a function of sensor sampling, S= (b) 1, (c) 10 and (d) 100. In all reconstructions simulated sensors were at 5, 7, 9 and 11 mm from the source. The initial guess parameter vector was P_{go} from Table 4.6.

radius, for the reconstructions in Figs. 4.38(b)-(d), is shown in Fig. 4.39. For S=1, the algorithm-predicted $R_{coag}(t)$ is an overestimation of the true values at all times. The true $R_{coag}(t)$ is well predicted for S=10. However, for S=100, the algorithm-predicted $R_{coag}(t)$ differs from the S=10 values at t>70 s, underestimating the true values for the remainder of the irradiation. This indicates that, for practical sensor locations, multiple sampling can compensate for reduced parameter sensitivity without introducing substantial parameter averaging errors, in contrast to Fig. 4.36. However, for large sampling, parameter averaging may affect the algorithm's ability to resolve the true coagulation radius. Moreover, as indicated in section 4.1.1.1, multiple sampling is required to compensate for noisy temperature data.

The effect of random noise on the performance of the dynamic algorithm is demonstrated by reconstructing our simulated ILP test case with and without random noise added to the measured temperatures. The true temperature distribution to be reconstructed is shown in Fig. 4.40(a). In all reconstructions a 4-sensor array with 2 mm sensor spacing was used with S=100. An initial "educated" guess parameter vector, P_{ge} from Table 4.6, was used to start the algorithm. Figs. 4.40(b), (c), (d) and (e) show reconstructed radial temperature errors for random noise levels of σ=0, 0.1, 0.5 and 1°C, respectively.

Without noise, the reconstruction is reasonable (Fig. 4.40(b)), in contrast to Fig. 4.38(d) when an initial "order of magnitude" guess parameter vector was used. As the noise level increases, the performance of the algorithm is degraded substantially. Again, as in Figs. 4.38(b)-(d), reconstruction errors in Figs. 4.40 (b)-

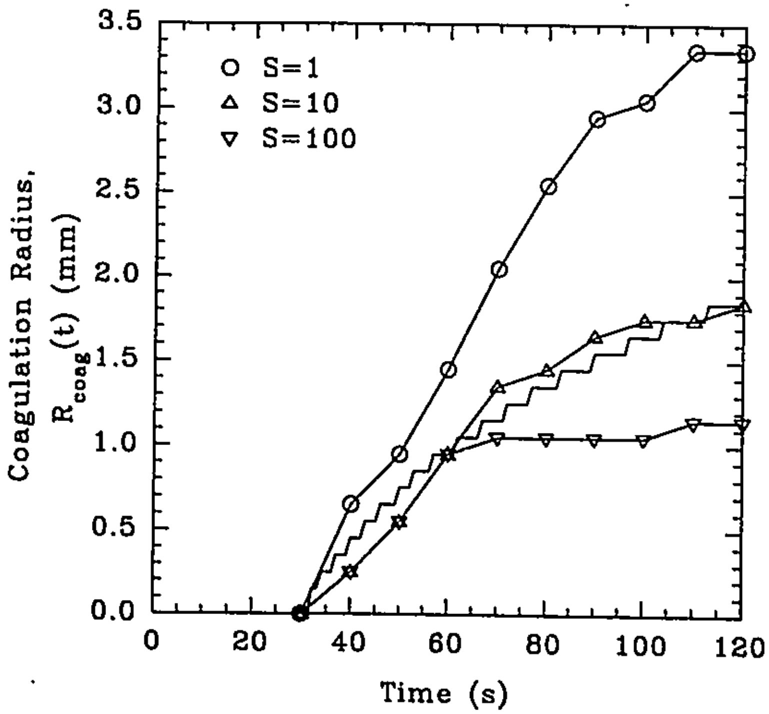

Figure 4.39. Algorithm-predicted $R_{coag}(t)$ as a function of sensor sampling from the reconstructions shown in Fig. 4.38. The true $R_{coag}(t)$ is given by the stepped curve.

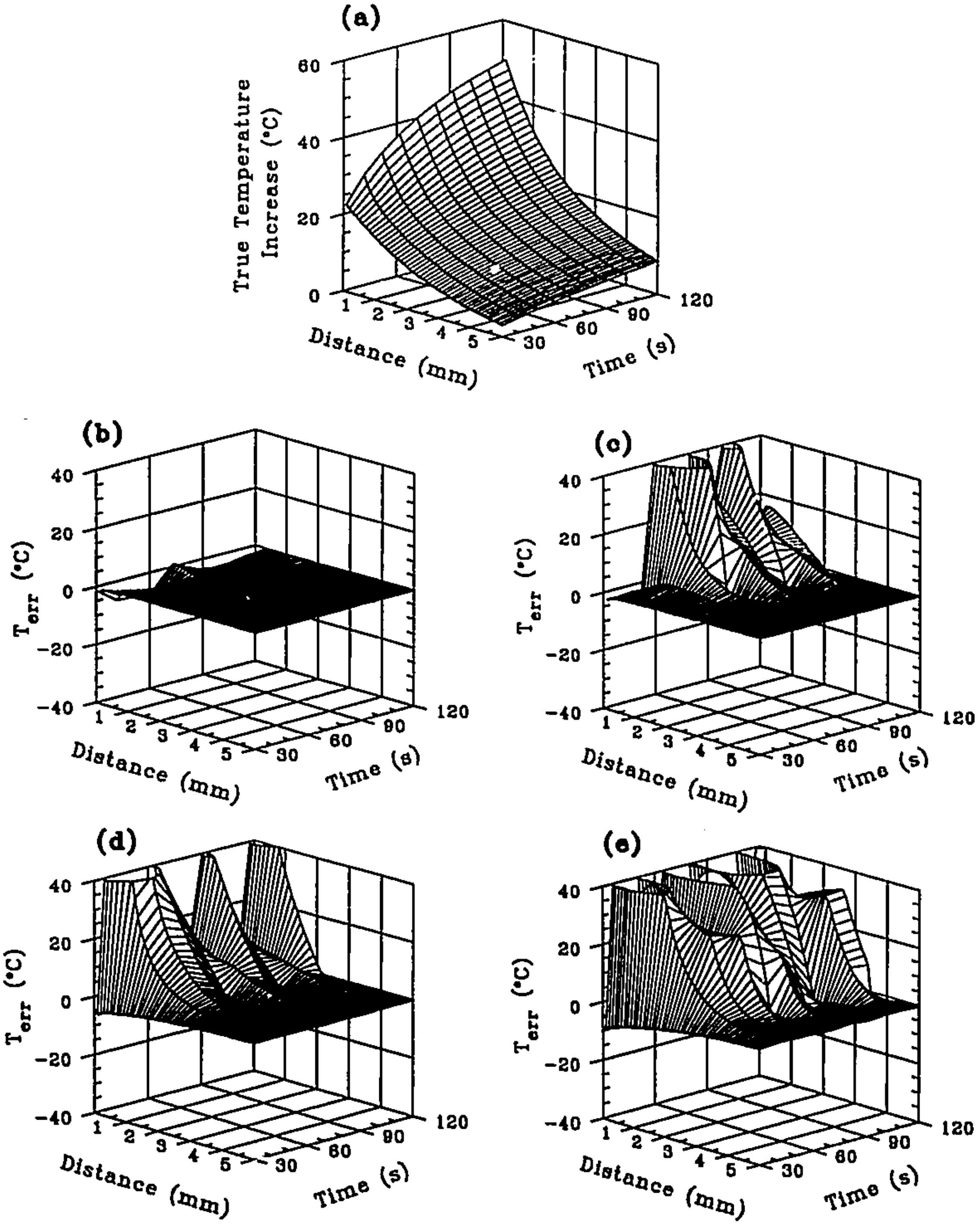

Figure 4.40. (a) True radial temperature profiles for a simulated ILP test case (120 s irradiation at 1.0 W). Reconstructed radial temperature errors at 30 s followed by 10 s reconstruction intervals for noisy measured temperature data as a function of random noise level, σ = (b) 0°C, (c) 0.1°C, (d) 0.5°C and (e) 1.0°C. In all reconstructions simulated sensors were at 5, 7, 9 and 11 mm from the source and S=100. The initial guess parameter vector was P_{ge} from Table 4.6.

(e) fall to near zero at the algorithm-predicted $R_{coag}(t)$ and define zones 1 and 2 in the estimation algorithm. In each reconstruction the algorithm-predicted $R_{coag}(t)$ was always less than 5 mm, such that temperatures were never sampled in zone 1. These results indicate that, for noisy temperature data, the absence of temperature sampling in zone 1 degrades reconstructions more than a poor initial guess.

The reconstruction errors at $r \leq 4$ mm for σ=1°C in Fig. 4.40(e) were due in large part to a substantial underestimation of k_{eff} and c_v in the algorithm-predicted coagulation zone (zone 1). Therefore, the reconstructions were repeated with estimates restricted by simple upper and lower bounds. The thermophysical and optical properties were constrained to lie within the reasonable intervals: $0.001 \leq k_{eff} \leq 0.01$ W/cm/°C, $3 \leq c_v \leq 5$ J/cm^3/°C, 0.25 cm^{-1} $\leq \mu_a \leq$ 2.5 cm^{-1}, and 1 cm^{-1} $\leq \mu_s' \leq$ 10 cm^{-1}. The k_{eff} range assumes that the true effective thermal conductivity is known only to within an order of magnitude, a reasonable assumption given the variability of blood perfusion in tumors (Feldmann et al. 1992). The c_v range is typical for mammalian tissues (Duck 1990), the optical property ranges are valid at 1064 nm (Cheong et al. 1990). An iterative estimate outside its allowed interval was randomly set to lie within the interval. The reconstruction errors for the constrained estimation are shown in Fig. 4.41. The performance of the algorithm improved when parameters were constrained. However, reconstruction errors are still substantial for the σ=1°C noise level simulated.

When estimates were tightly bounded to ±20% of the true values, the

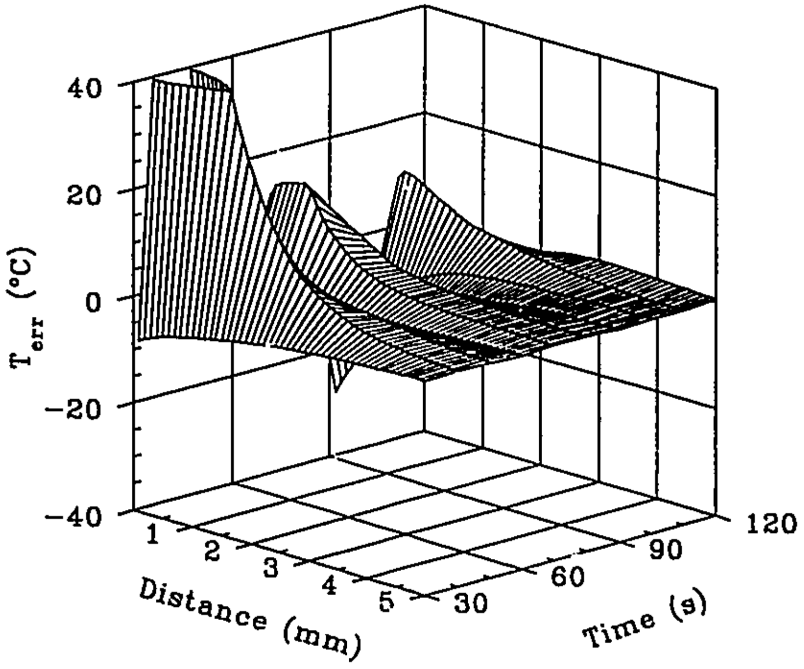

Figure 4.41. Reconstruction conditions used in Fig. 4.40(e) repeated with parameter estimates constrained to remain within reasonable intervals.

constrained routine, in most cases, was unable to find a minimum as λ continued to increase, within an iteration, until it reached its maximum, λ_{max}, pre-set to 10^3. In these instances, the diagonal elements of $(J^TJ + \lambda I)$ dominated the matrix causing the change in the parameter estimates to tend to zero. As a result the algorithm converged to an incorrect set of parameters and the functional was reduced minimally.

The reconstructions in Fig. 4.41 required ~ 7-10 min of CPU time. The evaluation of the Jacobian dominates the CPU effort. It is observed from (2.33) that each evaluation of the Jacobian matrix requires NZ+1 numerical solutions of the heat transfer model (HTM). Thus, the total CPU time is linearly related to the number of unknown parameters, $CPU \sim (NZ+1)t_{HTM}$, where t_{HTM}, the computational time required to solve the HTM, depends on the spatial and temporal resolution of the finite difference scheme. The CPU time, therefore, does not depend on the number of sensors or transient samples. For each reconstruction in Fig. 4.41, temperatures were calculated at 300 radial points (Δr=0.1 mm) for 100 temporal steps. The number of unknown parameters in the dynamic estimation algorithm ranged from 4 to 8. These observations indicate that real-time temperature reconstruction for practical applications may be limited.

Liauh et al. (1993) reported that, based on theoretical considerations, estimating the Jacobian using the adjoint method should be less computationally intensive than using the influence coefficient method. However, when solving practical inverse hyperthermia problems, the influence coefficient method consistently proved faster because the total number of iterations required for convergence was always less than for the adjoint method. Clearly, Jacobian approximations need to be further investigated before real-time applications can be realized.

4.4.3 2-D Inhomogeneous Test Case

To this point, in all reconstructions of simulated ILP test cases, the sensor array was positioned orthogonal to the optical fiber. However, in clinical practice, optical fiber(s) and sensor array(s) might be implanted parallel to each other. The optimal array design from section 4.4.1.1 was therefore re-evaluated for parallel source-sensor geometry. This required a suitable 2-D mathematical model.

Simulated measured temperature data, for a 120 s irradiation at 2.0 W in bovine liver *ex vivo*, were generated by solving the finite element expressions, (3.28) and (3.29), for the square mesh of side 40 mm shown in Fig. 3.5. The biophysical properties used are shown in Table 4.1. A single parameter zone, Z=1, was used in both forward and inverse simulations. The source was located at the center of the mesh. The finite element solutions with 1 mm mesh spacing and a 3 s temporal step agreed exactly with an approximation for an infinite line source of optical energy in an infinite homogenous medium (see Fig. 4.42). The exact calculation involved summing analytically evaluated temperatures for a point source of optical energy in an infinite homogeneous medium, Eq. (3.4), over a 6

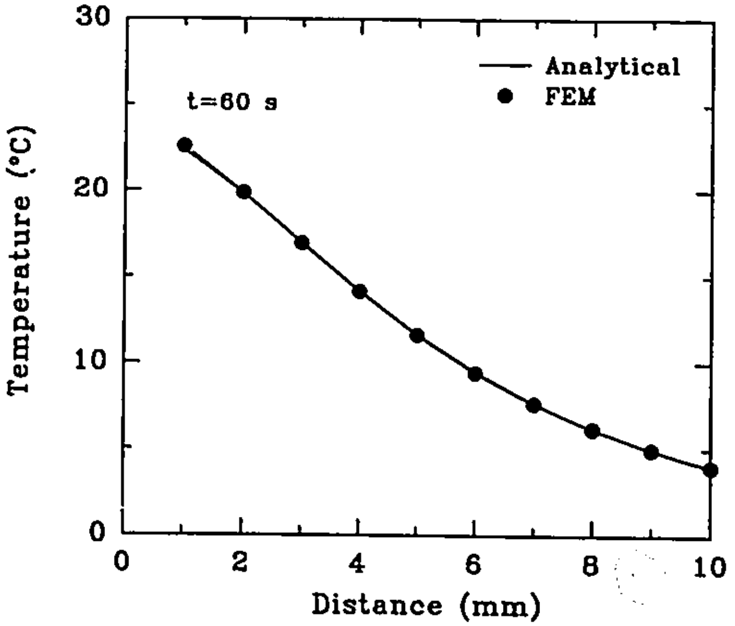

Figure 4.42. Finite element calculated temperatures, as a function of distance from the source, for a 2-D square mesh of side 40 mm with 1 mm mesh spacing and a 3 s temporal step verses an analytical approximation for an infinite line optical source in an infinite homogemeous medium.

cm finite length.

Temperatures were reconstructed using a 5 sensor array, with 2 mm sensor spacing, positioned orthogonal or parallel to the optical fiber as shown in Fig. 4.43. For the parallel case, the center of the array was directly opposite the source, a geometry of clinical relevance given possibly nonsymmetric temperature increases with respect to the source. In each geometry, the distance from the source to the nearest sensor was consistent, 5 mm.

Reconstructed temperature errors at the end of the first interval, 30 s, are shown in Fig. 4.44. The complete temperature field was accurately reconstructed for the orthogonal case, Fig 4.44(a), consistent with the 1-D simulations for optimal array design in section 4.4.1.1. However, with the array positioned parallel to the fiber, the reconstruction is degraded substantially as shown in Fig. 4.44(b). This is likely due to differences in the extent of the thermal field being sampled. For the orthogonal case, the thermal field is sampled by 5 sensors from 5-11 mm, whereas in the parallel case, temperature sampling is effectively by 3 sensors from 5-6.4 mm. By increasing sensor spacing to 4 mm, such that temperature sampling is from 5-9.5 mm, the algorithm can accuracy reconstruct temperatures as shown in Fig. 4.44(c). This indicates that optimal array design will depend on source-sensor geometry.

The potential of the estimation algorithm to resolve 2-D parameter distributions was evaluated by investigating the influence of localized tissue inhomogeneities on temperature distributions. The 2-D finite element mesh was

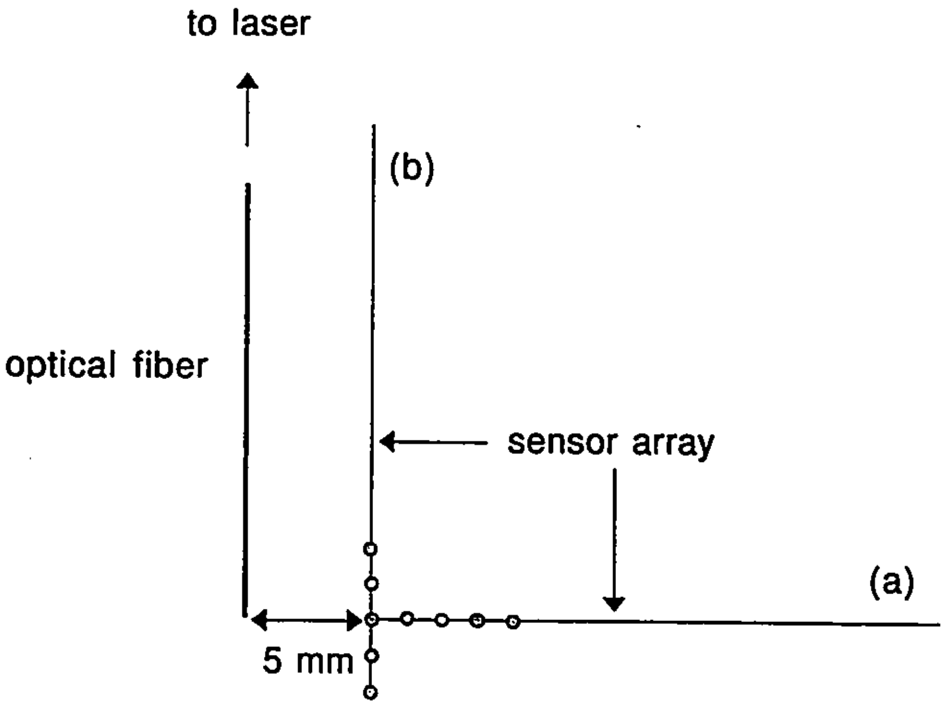

Figure 4.43. Source-sensor array geometries used to reconstruct temperatures during simulated ILP in liver *ex vivo*. The array is comprised of 5 sensors spaced 2 mm apart. (a) Sensor array orthogonal to optical fiber and (b) sensor array parallel to optical fiber.

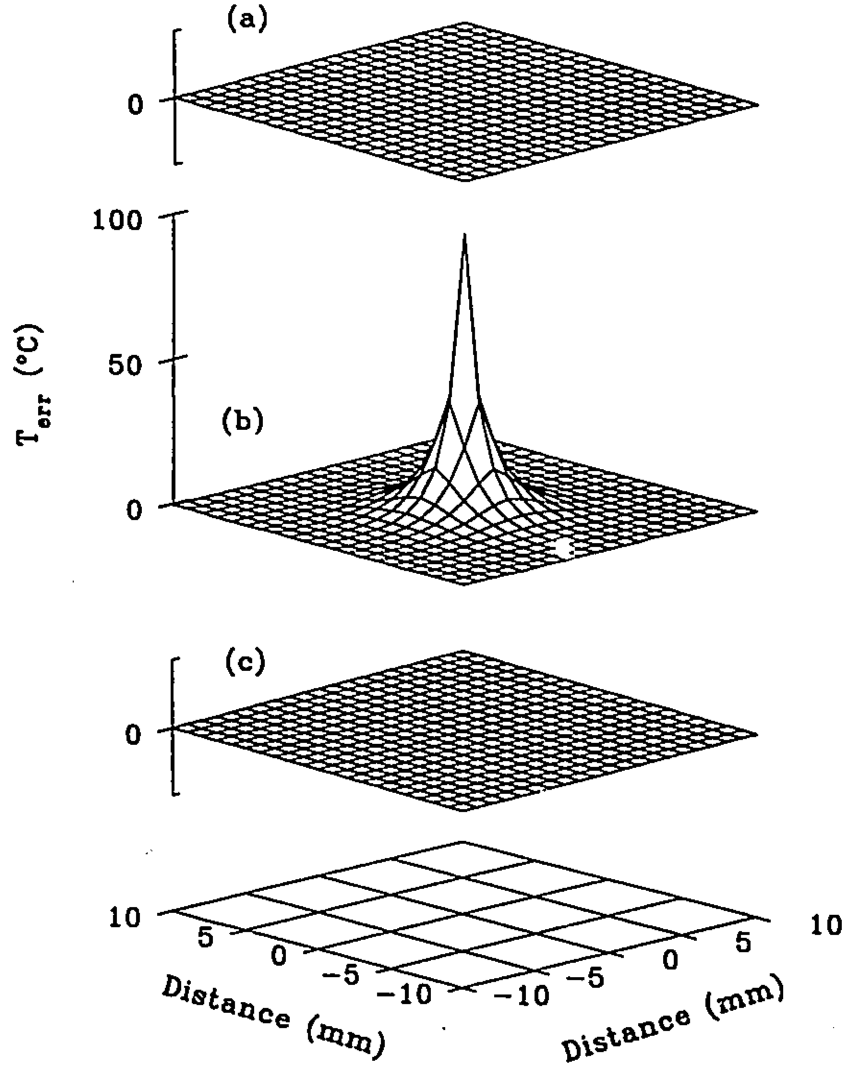

Figure 4.44. Reconstructions of simulated ILP in liver *ex vivo* as a function of source-sensor array geometries from Fig.4.43. A single parameter zone (homogeneous case) was used in the estimation algorithm with S=10. (a) Sensor array orthogonal to optical fiber, (b) sensor array parallel to optical fiber and (c) case (b) with 4 mm intersensor spacing.

divided into four equal-sized square quadrants about the origin. A twofold increase in the effective thermal conductivity or optical absorption coefficient in one of the four quadrants was modelled as shown in Fig. 4.45. This represents the presence of a large scale tissue parameter inhomogeneity. The true temperature distributions at 30 s and 120 s for the homogeneous case are shown in Figs. 4.46(a) and (b), respectively. The differences between temperature distributions at these two times for the homogeneous and inhomogeneous (see Fig. 4.45) cases are shown in Figs. 4.46(c)-(f). It is observed that substantial temperature changes due to the presence of the tissue parameter inhomogeneity are generally limited to the site of the inhomogeneity. The influence on temperature distributions is almost completely diminished at ~ 5 mm from the boundary of the inhomogeneity. This indicates that, for the ILP geometry shown in Fig. 4.43(b), accurate temperature reconstruction will likely not be possible if a tissue inhomogeneity, such as a blood vessel, and the sensor array are on opposite sides of the source.

4.5. Temperature Reconstruction During ILP in Bovine Muscle *Ex vivo*

The performance of the parameter estimation algorithm is demonstrated using *ex vivo* measured temperature data in bovine muscle for 300 s irradiations of 1.5 W at 1064 nm. The experimental setup and procedure was described in section 3.1. The 6-sensor array was used and was sampled at 5 s intervals during an irradiation. This was the shortest sampling interval achievable using the 286-16

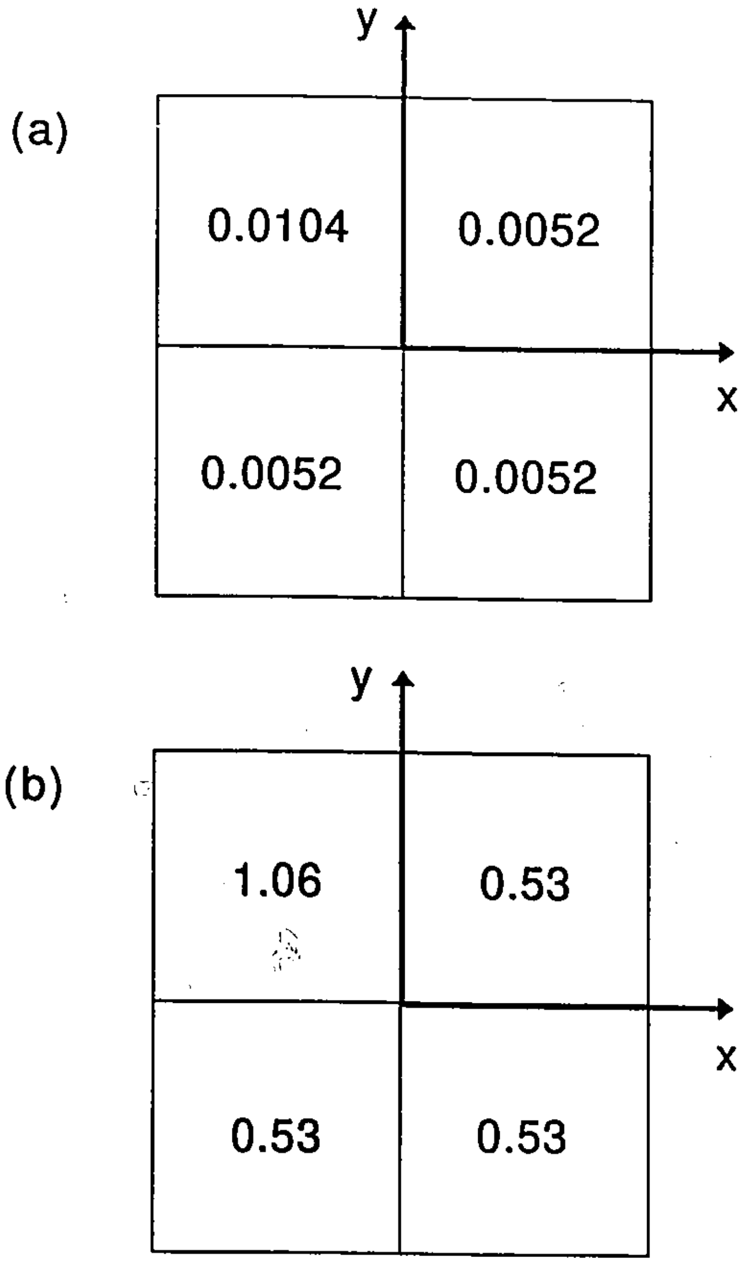

Figure 4.45. 2-D tissue parameter distributions used to generate finite element temperature solutions for the mesh shown in Fig. 3.6. An inhomogeneity in the distribution of the (a) effective thermal conductivity (W/cm/°C) or (b) absorption coefficient (cm^{-1}) was modelled. All other tissue parameters were spatially constant.

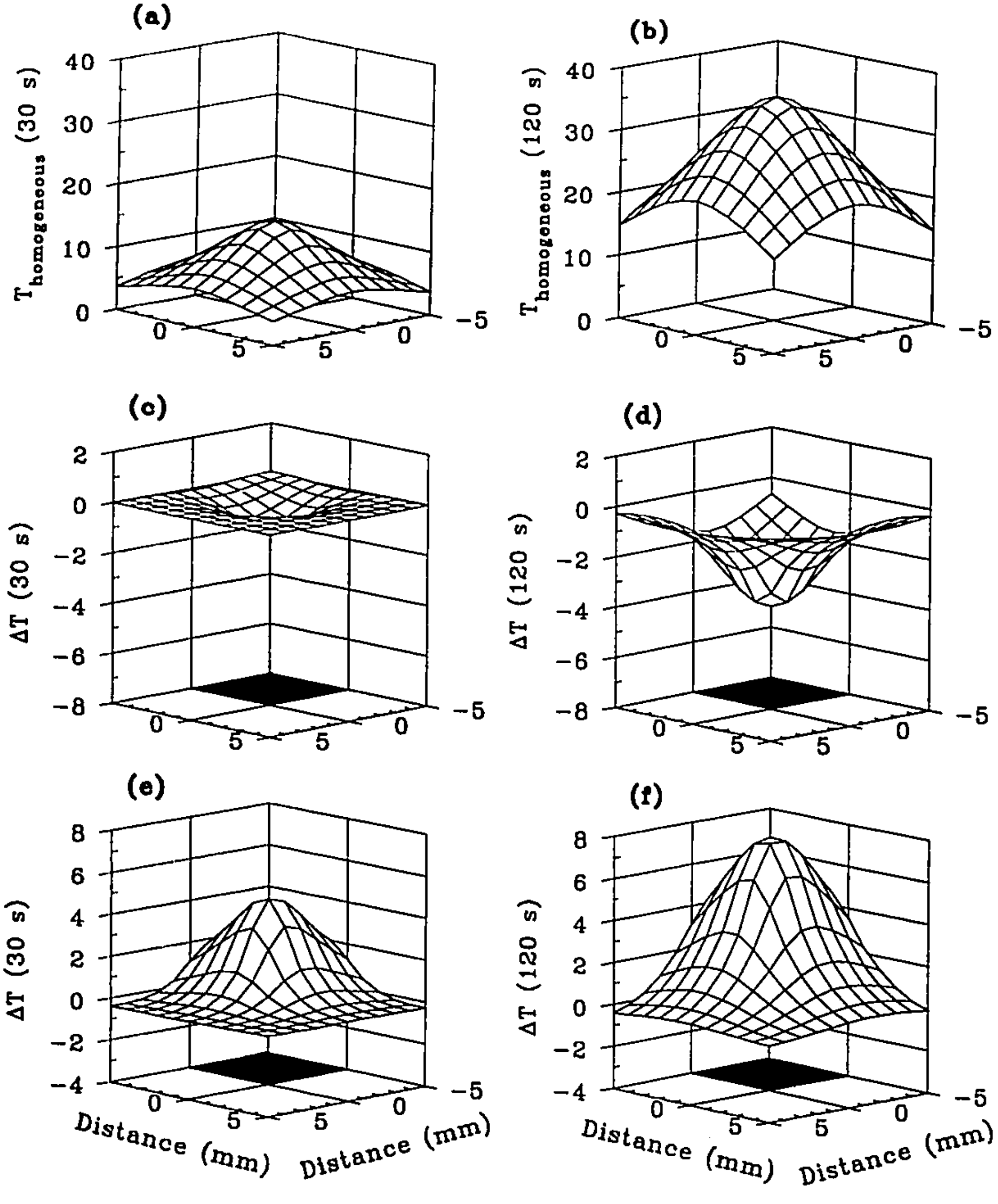

Figure 4.46. True temperature distributions at (a) 30 s and (b) 120 s for homogeneous tissue parameters. Temperature differences (ΔT), at 30 s and 120 s, between homogeneous and inhomogeneous distributions of (c) and (d), the effective thermal conductivity, and (e) and (f), the absorption coefficient. The shaded region in (c), (d), (e) and (f) represents the location of the inhomogeneity.

MHz processor. Two markedly different measured temperature profiles were chosen for reconstruction.

In the estimation algorithm, optical and thermal distributions were determined using the finite difference solutions for a sphere of radius 30 mm with 0.1 mm node spacing and a 1 s temporal step. Parameters were estimated according to the dynamic tissue discretization model shown in Fig. 4.34. An initial "educated" guess parameter vector, comprised of published values for bovine muscle, P_{true} in Table 4.6, was used. Reconstructions were performed every 30 s during the 300 s irradiations. Therefore, the maximum number of sensor samples was 6.

The performance of the temperature reconstruction algorithm with temperatures sampled *ex vivo* at 4 microthermocouple locations (5, 7, 9 and 11 mm) was assessed by comparing reconstructed temperatures with temperatures measured *ex vivo* at the remaining 2 microthermocouple locations (1 and 3 mm).

The first set of measured *ex vivo* transient temperature profiles and reconstructed temperatures at 1, 3, 5, 7, 9 and 11 mm, as a function of sensor sampling, are shown in Fig. 4.47. Generally, reconstructed and measured temperatures at input sensor locations show good agreement. It is observed that the reconstructed temperatures at 1 and 3 mm for $S=1$ and $S=6$ in Figs. 4.47(a) and (b), respectively, are the similar up 120 s (the first 4 reconstructions). The algorithm-predicted time of onset of coagulation was 120 s. Interestingly, the transient shape of the measured temperature profile at 1 mm around 120 s is

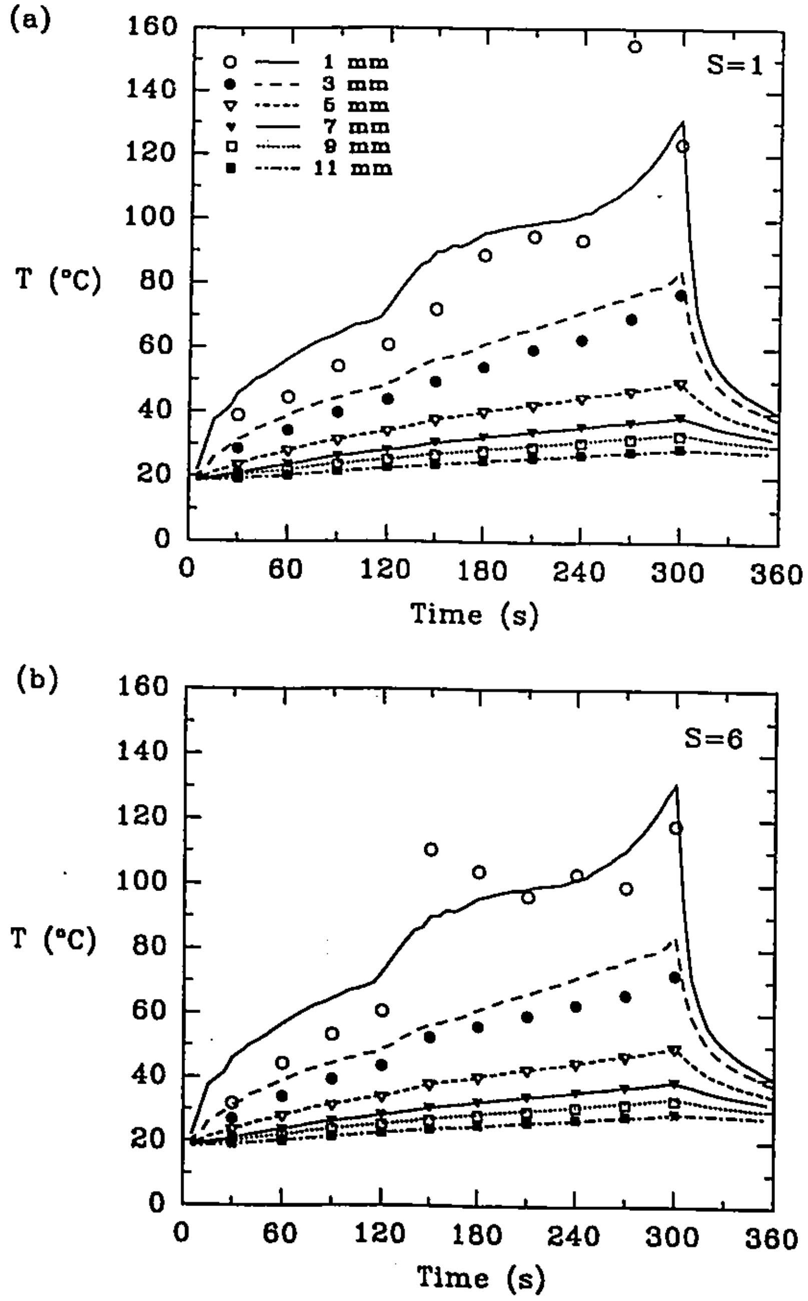

Figure 4.47. Measured *ex vivo* transient temperature profiles for a 300 s irradiation at 1.5 W in bovine muscle and reconstructed temperatures at 30 s intervals for (a) S=1 and (b) S=6. Parameters were estimated according to the dynamic tissue discretization model, Z(t)=1-3, with temperature inputs from sensors at 5, 7, 9 and 11 mm.

qualitatively similar to that in Fig. 4.2(a) for a coagulation-induced sixfold increase in scattering. Furthermore, this observed temperature transition occurred at ~ 70°C. It is therefore reasonable to assume that onset of coagulation occurred at ~ 120 s and, thus, was well predicted by the estimation algorithm.

Following the predicted onset of coagulation, reconstructions at 1 mm are generally better for S=1, Fig. 4.47(a) than for S=6, Fig. 4.47(b), for which parameter fits are essentially average values over the 30 s reconstruction interval. As discussed in section 4.4.2.2, such averaging limits the reconstruction of rapid temperature transients. However, reconstructed temperatures at 3 mm for S=1 and for S=6 are generally simiiar. In Fig. 4.47(a) the transient shape of the temperature profile at 1 mm was well estimated, except at 270 s. Interestingly, the algorithm recovered from this poor reconstruction. The algorithm-predicted time of onset of vaporization was 210 s, consistent with the measured temperature plateau at 1 mm occuring at ~ 100°C. The consistent underestimation of tissue temperatures at 1 and 3 mm in Fig. 4.47(a) is likely a result of tissue charring, present in the *ex vivo* lesion, but not considered in the dynamic model.

The second set of measured *ex vivo* transient temperature profiles and reconstructed temperatures at 1 and 3 mm are shown in Fig. 4.48. For clarity, reconstructed temperatures at 5, 7, 9 and 11 mm are omitted from the graphs. Reconstructed temperatures at both 1 and 3 mm are generally better for S=1, Fig. 4.48(a) than for S=6, Fig. 4.48(b). In Fig. 4.48(a), measured and reconstructed temperatures at 1 and 3 mm show reasonable agreement, such that the transient

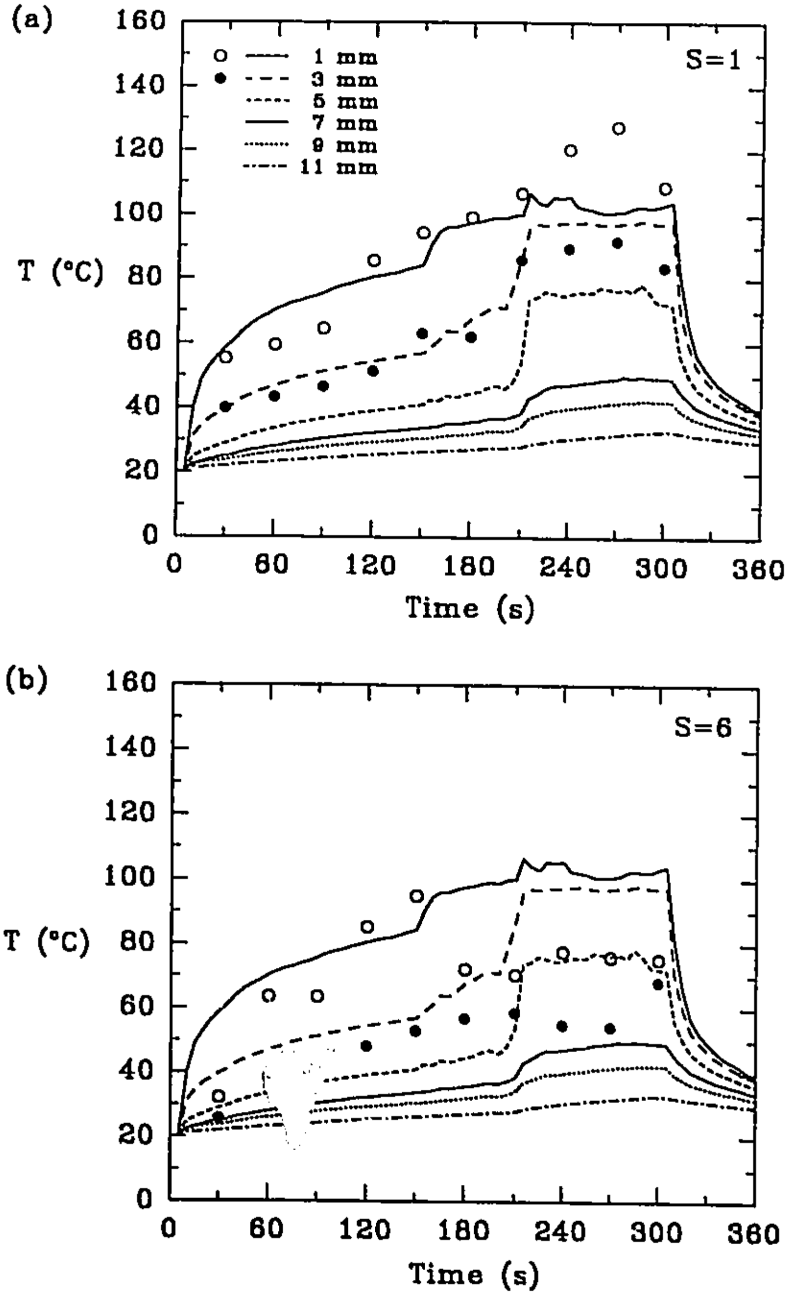

Figure 4.48. Same as Fig. 4.47 for a second set of measured *ex vivo* transient temperature profiles. (a) S=1 and (b) S=6.

shapes of the temperature profiles are well predicted. Again, char was present in the *ex vivo* lesion, but not considered in the model.

The reasonable accuracy observed for the S=1 reconstructions indicates that the noise level in our system may be negligible. The CPU time required for the S=1 reconstructions ranged from 4-10 min.

CHAPTER 5. Conclusions and Future Considerations

5.1 Dynamic Models of ILP

Thermal and optical models of ILP generally are developed to evaluate its potential in various soft tissues. Theoretical parametric investigations attempt to characterize the thermal response of tissues to various irradiation parameters in order to optimize a treatment protocol. In this thesis, tissue coagulation and water vaporization have been identified as important optical and thermal events which need to be considered in the physical description of ILP. These phase changes have been incorporated into a dynamic model of tissue heating during ILP. Additionally, for *in vivo* modelling, dynamic changes in the perfusion pattern due to induced thermal damage have been incorporated.

The results of section 4.1 demonstrate that increases in scattering due to coagulation change the energy deposition pattern, broadening the heated region. The difference between predicted temperature distributions for uniform and coagulation-induced increased scattering increases with exposure duration until thermal equilibrium is established. Furthermore, the coagulation-induced transient change in the energy deposition rate shown in Fig. 4.3. delays the onset of thermal equilibrium. Increased perfusion decreases the time to steady-state and the temperature at steady-state is reduced compared to the non-perfused case.

It was demonstrated in Fig. 4.6 that for spatially uniform scattering, the choice of blood perfusion pattern affects minimally temperature distributions. However, for coagulation-increased scattering, the coagulation diameters predicted by the uniform and lesion perfusion models can be markedly different. The difference in the predicted extent of thermal damage becomes more pronounced with increasing exposure duration. The lesion perfusion model predicts that the volume of thermal damage will continue to expand at longer exposures. This could explain the nonflat asymptotes observed by Malone et al. (1994b).

Beacco et al. (1994) and Prapavat et al. (1996) have considered coagulation-increased scattering in the physical description of ILP based on an Arrhenius-type damage integral model and a 60°C threshold model, respectively. In the latter study, predicted coagulation dimensions agreed with experimentally measured lesions. The 60°C threshold coagulation model seems to be a good predictor of coagulation dimensions at early and intermediate times. This is further supported by empirical data, indicating that irreversible tissue coagulation occurs in ~ 3 s (Prapavat et al. 1996). However, the instantaneous step increase in optical scattering, assumed in our model, overestimates the empirical near-linear increase in μ_s' with increasing temperature (Jaywant et al. 1993, Pickering et al. 1994). Furthermore, tissue coagulation has been observed to increase long after thermal equilibrium has been established (Wyman et al. 1994, Matsumoto et al. 1992), indicating that an Arrhenius-type damage integral would be a better predictor of coagulation dimensions at steady-state. Coagulation at ~ 48°C (Foepping 1996, private communication) has been observed in rabbit muscle *in vivo* at 1200 s, long after thermal equilibrium. Thus the predicted coagulation diameters presented in this thesis should be considered underestimations. Clearly, the accuracy of the dynamic models should be examined using experimental data *in vivo*.

In the future, the need for dynamic optical models may be limited. Recently, Wyman et al. (1992) reported that point heat sources produce larger coagulation volumes than point optical sources and, in some organs, tissue charring is required to produce clinically relevant lesions. There has since been interest in precharring of the fiber tip (Amin et al. 1993b). Once charring occurs, tissue optical properties affect minimally temperature distributions, such that temperatures are determined principally by thermal diffusion and blood perfusion. However, there continues to be concern about the release of CO and CO_2, and the potential for air emboli. Furthermore, charring can damage the fiber tip, as observed in this work following ILP in bovine muscle.

Therefore, optimizing irradiation parameters to maximize lesion formation while minimizing the potential for charring was investigated. The results from section 4.1 indicate that 8-10 mm diameter lesions in liver are possible without charring. The potential for charring is greater in highly perfused tissues with small optical penetration depths. These data should provide a basis with which to conduct experimental studies *in vivo*. The potential of ILP without charring has yet to be thoroughly investigated. To this end, modelling and experimental studies of multiple fiber arrangements, such as described by Steger et al. (1992) and Wyman (1993), could prove useful.

The literature indicates that coagulation-induced increases in optical scattering vary with tissue type and wavelength. Clearly, there is a need to investigate further the temperature-induced dynamic changes in the optical properties of *in vivo* tissues.

5.2 Estimating Tissue Charring Temperature

A quasi-linear model of tissue browning/charring during single fiber ILP was presented. Given that the time of onset of browning/charring and the rate of increase in optical absorption is unknown, measured temperatures were used as *timers* to guide model calculations. The results demonstrate that tissue charring is likely the endpoint of a tissue browning process, characterized by increased optical absorption. This process was approximated as a linear continuous shift in energy deposition from a point optical source to a point heat source.

Two major limitations of the model are that water vaporization was considered to be instantaneous and that, following the production of opaque char, the thermophysical properties in the charred region were assumed to be the same as the vaporized region. The first assumption will likely overestimate the tissue charring temperature while the latter will underestimate temperatures within the measured char radius.

It is clear from Figs. 4.13 and 4.14 that temperature monitoring at practical distances, 3-5 mm from the source, may not predict accurately the onset of charring due to the minimal effect on temperature at these distances. However, with the use of an optical probe, such as described by Matthewson et al. (1987), the onset of charring would most certainly be detectable as a complete loss of optical intensity.

Future development of the browning/charring model should consider blood perfusion for *in vivo* applications. Furthermore, the accuracy of the model should be examined with more experimental data. The approach of placing observed charring dimensions on calculated temperatures after illumination substitutes limited uncertainty in the calculational model for potentially great uncertainty associated with direct temperature measurements. It may be possible to achieve still greater accuracy by using this approach with a different geometry, for example, planar geometry, in which the temperature gradients might be reduced.

5.3 Temperature Reconstruction

The temperature reconstruction work presented in this thesis was an initial assessment of on-line temperature reconstruction by estimating the biophysical properties of tissue during ILP. Insight into some of the practical and technical limitations of a temperature reconstruction system has been gained. The following temperature acquisition parameters were identified: 1) number of sensors, 2) intersensor spacing, 3) source-sensor geometry and 4) number of transient sensor samples. The results indicate that there are optimal sensor arrangements and sampling frequencies for accurate temperature reconstruction. Solutions to this inverse problem required Levenberg-Marquardt regularization due to inherent ill-conditioning of the sensitivity matrices; but its success was limited. However, the inverse algorithm seems to be stable. The potential of the parameter estimation algorithm to recover the true biophysical properties may be restricted due to "optothermal similarity". Reduced parameter sensitivity at practical sensor locations was the dominant cause of reconstruction errors. For accurate reconstruction near the source a sensor must be placed ~ 1 mm from the optical fiber, which is not clinically practical.

The presence of random noise degraded reconstruction accuracy, principally between the source and the first sensor in an array located at relevant distances of 3-5 mm. For homogeneous tissues, reasonable reconstruction accuracy for noisy temperature data may require sampling of 10 Hz or greater. However, for a 2 zone tissue model, reconstructions of simulated ILP test cases are poor in the coagulation region regardless of the sampling frequency. Interestingly, for a 2 zone model, with a single sample, the algorithm was able to reconstruct measured temperature profiles in bovine muscle *ex vivo* with reasonable accuracy. This suggests that the level of noise in the temperature acquisition system was less than that modelled. Further testing of the algorithm using real measured data is required.

The following criteria necessary to judge, in clinical practice, the success of a reconstruction have been identified : 1) convergence to reasonable values, 2) F reduced, 3) rapid convergence for final few iterations and 4) a small condition number for the Hessian matrix. It was demonstrated that all four criteria can be satisfied for homogeneous tissues when temperature acquisition is optimal. However, for inhomogeneous tissues, only the second criterion was consistently satisfied, resulting in poor reconstructions.

Ultimately, the results indicate that the major limitation to the use of this temperature reconstruction system is the accuracy of source/sensor placement. Generally, positioning of sensors and optical fibers is achieved using a template placed near the tissue surface. Axial positioning is achieved using graded marks along the length of the devices. At best, the placement accuracy is ±1 mm. Therefore the use of a stereotactic guidance system may be required. This becomes increasingly important in tissues with small optical penetration depths where induced thermal gradients near the source are large.

Although the recovery of true tissue parameters and accurate reconstruction near the source are limited, the potential exists for accurate predicted of the boundary of coagulative necrosis, as observed in Fig. 4.39. Clearly, the potential of multiple-parameter estimation to predict accurately asymmetric necrotic boundaries needs to be investigated using 3-D non-linear reconstruction models with temperature measurements obtained from microthermocouple arrays.

It is indicated that the reconstruction system should rely on temperature feedback from sensors to determine the first reconstruction interval. Furthermore, to minimize systematic errors in the dynamic estimation algorithm, a short reconstruction interval should be used, approximately 10 s. However, the choice of optimal length for the reconstruction interval would likely depend on the time rate of change of the coagulation boundary, which in turn should depend on tissue type and wavelength. Further simulations are warranted.

The simulated ILP test cases presented in this thesis by no means represents a comprehensive set of possible biophysical properties or irradiation parameters. For *in vivo* applications, the possible mismatch between the effective thermal conductivity model used in the estimation algorithm and real tissue behaviour needs to be investigated.

For applications in real-time monitoring, it may be possible to update only certain parts of the Jacobian matrix, allowing for faster calculation of the matrix at each iteration. This needs to be explored.

Finally, the *ex vivo* results indicate that accurate temperature reconstruction in the water vaporized zone, T≥100°C, may not be possible with sensors at practical locations. Furthermore, the dynamics of tissue browning/charring, as described in sections 3.5 and 4.2, could not be well predicted using a dynamic 3 zone model. Therefore, future testing of the dynamic estimation algorithm should be limited to ILP applications with temperature less than 100°C. The potential exists to use the reconstructed maximum tissue temperature at the fiber tip in a feedback loop to control transient laser power deposition, in order to maintain temperatures below 100°C and reduce the potential for charring.

APPENDIX

This thesis is part of a larger project investigating ILP in soft tissues from which several papers have been published:

Whelan, W.M., Wyman, D.R. and Wilson, B.C., 1995, "Investigations of large vessel cooling during interstitial laser heating", *Med. Phys.*, **22**, pp. 105-115.

Wyman, D.R. and Whelan, W.M., 1994, "Basic optothermal diffusion theory for interstitial laser photocoagulation", *Med. Phys.*, **21**, pp. 1651-1656.

Wyman, D.R., Whelan, W.M. and Wilson, B.C., 1992, "Interstitial laser photocoagulation: Nd:YAG 1064 nm optical source compared to point heat source," *Lasers Surg. Med.*, **12**, pp. 659-664, 1992.

The work presented in this thesis has been separated into a number of papers which have been accepted for publication or will be submitted for publication:

Whelan, W.M. and Wyman, D.R., 1995, "Temperature reconstruction by estimating the thermophysical and optical properties of tissues during interstitial laser heating", in L.J. Hayes ed., *Advances in Heat and Mass Transfer in Biotechnology*, **HTD-322**, pp. 17-26.

Whelan, W.M. and Wyman, D.R., 1996, "A model of tissue charring during *ex vivo*

interstitial laser photocoagulation: Estimating tissue charring temperature", *IEEE Trans Biomed. Eng.* (in press).

Whelan, W.M. and Wyman, D.R., "Dynamic modelling of interstitial laser photocoagulation *in vivo*: Implications for lesion formation in liver", *Lasers Surg. Med.*, (to be submitted).

Whelan, W.M. and Wyman, D.R., "Dynamic temperature reconstruction during interstitial laser photocoagulation: A study of multiple-parameter estimation", *Med. Phys.*, (to be submitted).

REFERENCES

Amin, Z., Bown, S.G. and Lees, W.R., 1993a, "Liver tumor ablation by interstitial laser photocoagulation: review of experimental and clinical studies," *Sem. Interventional Radiology*, **10**, pp. 88-100.

Amin, Z., Buonaccorsi, G., Mills, T., Harries, S., Lees. W.R. and Bown, S.G., 1993b, "Interstitial laser photocoagulation: Evaluation of a 1320 nm Nd-YAG and an 805 nm Diode Laser: the significance of charring and the value of precharring the fibre tip," *Lasers Med. Sci.*, **8**, pp. 113-120.

Amin, Z., Donald, J.J., Masters, A., Kant, R., Steger, A.C., Bown, S.G. and Lees, W.R., 1993c, "Hepatic metastases: Interstitial laser photocoagulation with real-time US monitoring and dynamic CT evaluation of treatment," *Radiology*, 187, pp. 339-347.

Anderson, R.R., 1991, "Introduction to laser photobiology", in Goldman, L., ed. Laser Non-Surgical Medicine:New Challenges for an Old Application, Lancaster: Technomic Publishing, pp. 17-22.

Anhalt, D. and Hynynen, K., 1992, "Thermocouples-The Arizona experience with in-house manufactured probes", *Med. Phys.*, **19**, pp. 1325-1333.

Anvari, B., Motamedi, M., Torres, J.H., Rastegar, S. and Orihuela, E., 1994a, " Effects of surface irrigation on the thermal response of tissue during laser irradiation", *Lasers Surg. Med.*, **14**, 386-395.

Anvari, B., Rastegar, S. and Motamedi, M., 1994b, "Modeling of intraluminal heating of biological tissue: Implications for treatment of benign prostatic hyperplasia", *IEEE Trans. Biomed. Eng.*, **41**, pp. 854-864.

Arfken, G., 1985, Mathematical Methods for Physicists, Academic Press: London, pp. 897-923.

Arkin, H, Xu, L.X. and Holmes, K.R., 1994, "Recent developments in modeling heat transfer in blood perfused tissues", *IEEE Trans. Biomed. Eng.*, **41**, pp. 97-107.

Arnfield, M.R., Tulip, J. and McPhee, M.S., 1988, "Optical propagation in tissue with anisotropic scattering", *IEEE Trans. Biomed. Eng.*, 35, pp. 372-381.

Arrhenius, S., 1889, "Uber die Reaktionsgeschwindigkeit bei der Inversion von Rohrzucker durch Sauren", Z. *Physik Chem.*, 4, p. 226.

Arridge, S.R., Schweiger, M., Hiraoka, M. and Delpy, D.T., 1993, "A finite element approach for modelling photon transport in tissue", *Med. Phys.*, 20, pp. 299-309.

Babbs, C.F., Fearnot, N.E., Marchoshy, J.A., Moran, C.J., Jones, J.T. and Plantenga, T.D., 1990, " Theoretical basis for controlling minimal tumor temperature during interstitial conductive heat therapy", *IEEE Trans. Biomed. Eng.*, 37, pp. 662-672.

Beacco, C.M., Mordon, S.R. and Brunetaud, J.M., 1994, "Development and experimental in vivo validation of mathematical modeling of laser coagulation", *Lasers Surg. Med.*, 14, pp. 362-373.

Becker, M., 1986, Heat Transfer: A Modern Approach, Plenum Press, N.Y.

Bettag, M., Ulrich, F., Schober, R., Furst, G., Langen, K.J., Sabel, M. and Kiwit, J.C.W., 1991, "Stereotactic laser therapy in cerebral gliomas", *Acta. Neurochir. Suppl.*, 52, pp. 81-83.

Bevington, P.R., 1969, Data Reduction and Error Analysis for Scientists and Engineers, New York: McGraw Hill.

Birngruber, R., 1979, "Thermal modelling in biological tissues". In Hillenkamp, F., Pratesi, R. and Sacchi, C.A., eds. Lasers in Biology and Medicine, New York: Plenum Press, pp. 77-97.

Boulnois, J., 1986, "Photophysical processes in recent medical laser developments: a review", *Lasers Med. Sci.*, 1, pp.47-66.

Bowman, H.F., Cravalho, E.G. and Woods, M., 1975, "Theory, measurement, and application of thermal properties of biomaterials," *Ann. Rev. Biophys. Bioeng.*, 4, pp. 43-80, 1975.

Bown, S.G., 1983, "Phototherapy of tumours," *World J. Surg.*, 7, p. 700.

Carslaw, H.S. and Jaeger, J.C., 1958, Conduction of Heat Solids, Oxford University, New York.

Castren-Parsons, M., Lipasti, J., Puolakkainen, P. and Schroder, T., 1992, " Laser-induced hyperthermia: Comparison of two different methods, " *Lasers Surg. Med.*, 12, pp. 665-668.

Castro, D.J., Lufkin, R.B., Saxton, R.E., Nyerges, A., Schiller, V., Grant, E., Soudant, J., Szabey, M. and Ward, P.M., 1992, "MRI and/or ultrasound guided interstitial ND:YAG laser phototherapy for palliative treatment of recurrent head and neck tumors: Clinical experience," *Lasers Surg. Med. Suppl.*, 4, p. 48.

Chapman, A.J., 1987, Fundamentals of Heat Transfer, MacMillan Publishing Co., N.Y.

Charny, C.K. and Levin, R.L., 1989, "Bioheat transfer in a branching countercurrent network during hyperthermia," *J. Biomech. Eng.*, **111**, pp. 263-270.

Charny, C.K., Weinbaum, S. and Levin, R.L., 1990, "An evaluation of the Weinbaum-Jiji bioheat equation for normal and hyperthermic conditions," *J. Biomech. Eng.*, **112**, pp. 80-87.

Chen, M.M. and Holmes, K.R., 1980, " Microvascular contributions in tissue heat transfer", *Ann. N.Y. Acad. Sci.*, **335**, pp. 137-150.

Cheong, W.F., Prahl, S.A. and Welch, A.J., 1990, "A review of the optical properties of biological tissues," *IEEE J. Quantum Electron.*, **26**, pp. 2166-2185.

Clegg, S.T. and Roemer, R.B., 1985a," A comparative evaluation of unconstrained optimization methods applied to the thermal tomography problem", *J. Biomech. Eng.*, **107**, pp. 228-233.

Clegg, S.T. and Roemer, R.B., 1985b, "A study of the effect of sensor placement and perfusion pattern variations on thermal tomography solutions in hyperthermia," *IEEE Trans. Biomed. Eng.*, **32**, pp. 677-682.

Clegg, S.T., Das, S.K., Zhang, Y., Macfall, J., Fullar, E. and Samulski, T.V., 1995, "Verification of a hyperthermia model method using MR thermometry", *Int. J. Hyperthermia*, **11**, pp. 409-424.

Cooper, T.E. and Trezek, G.J., 1971, "Correlation of thermal properties of some human tissues with water content", *Aerospace Med.*, **42**, pp. 24-27.

Dachman, A.H., McGehee, J.A., Beam, T.E., Burris, J.A. and Powell, D.A., 1990, " US-guided percutaneous laser ablation in liver tissue in a chronic pig model", *Radiology*, **176**, pp. 129-133.

Daikuzono, N., Suzuki, S., Tajiri, H., Tsunekawa, H., Ohyama, M. and Joffe, S.N., 1988, "Laserthermia: A new computer-controlled contact Nd:YAG system for interstitial local hyperthermia", *Lasers Surg. Med.*, **8**, pp. 254-258.

Davies, M., Dowden, J., Steger, A., Kapadia, P. Whiting, P., 1989, "A mathematical model for interstitial laser treatment of tumors using four fibers", *Lasers Med. Sci.*, **4**, pp. 41-53.

Delannoy, J., Lebihan, D., Hoult, D.I. and Levin, R.L., 1990, "Hyperthermia system combined with a MR unit", *Med. Phys.*, **17**, pp. 855.

Derbyshire, G.J., Bogen, D.K. and Unger, M., 1990, "Thermally induced optical property changes in myocardium at 1.06 μm", *Lasers Surg. Med.*, **10**, pp. 28-34.

Dewey, W.C., Hopwood, L.E., Sapareto, S.A. and Gerweck, L.E., 1976, "Cellular responses to combinations of hyperthermia and radiation", *Radiology*, **123**, pp. 463-479.

Dickinson, R.J., Hall, A.S., Hind, A.J. and Young I.R., 1986, "Measurement of changes in tissue temperature using MR imaging", *J. Computer-Assisted Tomography*, **10**, pp. 468-472.

Divrik, A.M., Roemer, R.B. and Cetas, T.C., 1984, "Inference of complete tissue temperature fields from a few measured temperatures: An unconstrained optimization method," *IEEE Trans. Biomed. Eng.*, **31**, pp. 150-160.

Doss, J.D., 1985, "Simulations of automatic temperature control in tissue hyperthermia calculations", *Med. Phys.*, **12**, pp. 693-697.

Dowden, J.M., Davis, M., Kapadia, P. and Matthewson, K., 1987, "Heat flow in laser treatment by local hyperthermia", *Lasers Med. Sci.*, **2**, pp. 211-221.

Dowlatshahi, K., Bhattacharya, A.K., Matalon, T., Silver, B. and Williams, J.W., 1992a, "Percutaneous interstitial laser therapy of patient with recurrent hepatoma in a transplanted liver," *Surgery*, **112**, pp. 603-606.

Dowlatshahi, K, Babish, D., Bangert, J.D. and Kluiber, R., 1992b, "Histologic evaluation of rat mammary tumor necrosis by interstitial Nd:YAG laser hyperthermia", *Lasers Surg. Med.*, **12**, pp. 159-164.

Duck, F.A., 1990, <u>Physical Properties of Tissue</u>, Academic Press: London.

Duderstadt, J.J. and Hamilton, L.J., 1976, <u>Nuclear Reactor Analysis</u>. Wiley and

Sons.

El-Ouahabi, A., Guttmann, C.R.G., Hushek, S.G., Bleier, A.R., Dashner, K., Dikkes, P., Black, P. and Jolesz, F.A., 1993, " MRI guided interstitial laser therapy in a rat malignant glioma model", *Lasers Surg. Med.*, **13**, pp. 503-510.

Feldmann, H.J., Molls, M., Hoederath, A., Krumpelmann, S. and Sack, H., 1992," Blood flow and steady state temperatures in deep-seated tumors and normal tissues", *Int. J. Rad. Oncol. Biol. Phys.*, **23**, pp. 1003-1008.

Gerig, L.H., Szanto, J. and Raaphorst, G.P., 1992, "On the spatial resolution of clinical thermometers," *Med. Phys.*, **19**, pp. 679-684.

Gewiese, B., Beuthan, J., Fobbe, F., Stiller, D., Muller, G., Bose-Landgraf, J., Wolf, K. Deimling, M., 1994, "Magnetic resonance imaging-controlled laser-induced interstitial thermotherapy," *Invest. Rad.*, **29**, pp. 345-351.

Gill, P.E., Murray, W. and Wright, M.H., 1993, Practical Optimization. San Diego, CA: Academic Press.

Hahl, J., Haapiainen, R., Ovaska, J., Puolakkainen, P. and Schöder, T., 1990, "Laser-induced hyperthermia in the treatment of liver tumours," *Laser Surg. Med.*, **10**, pp. 319-321.

Harries, S.A., Amin, Z., Smith, M.E.F., Lees, W.R., Cooke, J., Cook, M.G., Scurr, J.H., Kissin, M.W. and Bown, S.G., 1994, "Interstitial laser photocoagulation as a treatment for breast cancer", *Br. J. Surg.*, **81**, pp. 1617-1619.

Henriques, F.C., 1947, "Studies of thermal injury", *Arch. Pathol.*, **43**, pp. 489-502.

Hillenkamp F., 1979, "Interaction between laser radiation and biological systems". In Hillenkamp, F., Pratesi, R. and Sacchi, C.A., eds. Lasers in Biology and Medicine. New York:Plenum Press, pp. 37-76.

Jacques, S.L., Rastegar, S., Motamedi, M., Thomsen, S.L., Schwartz, J., Torres, J. and Mannonen, I., 1992, "Liver photocoagulation with diode laser (805 nm) vs ND:YAG laser (1064 nm)," *SPIE Proc.*, **1646**, pp. 107-117.

Jaywant, S., Wilson, B., Patterson, M., Lilge, L., Flotte, T., Woolsey, J. and McCulloch, C., 1993, "Temperature dependent changes in the optical absorption and scattering spectra of tissues", *SPIE Proc.* **1882**, pp. 218-229.

Jiji, L.M., Weinbaum, S. and Lemons, D.E., 1984, "Theory and experiment for the effect of vascular temperature on surface tissue heat transfer-Part II: Model formulation and solution", *J. Biomech. Eng.*, 106, pp. 331-341.

Judy, M.M., Matthews, L., Aronoff, B.L and Hults, D.F., 1993, "Soft tissue studies with 805 nm diode laser radiation: Thermal effects with contact tips and comparison wuth effects of 1064 nm Nd:YAG laser radiation", *Lasers Surg. Med.*, 13, pp. 528-536.

Kerker, M., 1969, The Scattering of Light, New York:Academic.

Kleinman, A.M. and Roemer, R.B., 1983, "A direct substitution, equation error technique for solving the thermographic tomography problem,"*J. Biomech. Eng.*, 105, pp. 237-243.

Kolios, M.C., Sherar, M.D. and Hunt, J.W., 1995, " Large blood vessel cooling in heated tissues: a numerical study", *Phys. Med. Biol.*, 40, pp. 477-494.

Lagendijk, J.J.W., 1982, "The influence of blood flow in large vessels on the temperature distributions in hyperthermia", *Phys. Med. Biol.*, 27, pp. 17-23.

Lagendijk, J.J.W., Schellekens, M., Schipper, J. and van der Linden, P.M., 1984, "A three-dimensional description of heating patterns in vascularized tissues during hyperthermic treatment", *Phys. Med. Biol*, 29, pp. 495-507.

Laible, J.P., Pflaster, D., Simon, B.R., Krag, M.H., Pope, M. and Haugh, L.D., 1994, "A dynamic material parameter estimation procedure for soft tissue using a poroelastic finite element model,", *J. Biomech. Eng.*, 116, pp. 19-29.

LeBihan, D., Delannoy, J. and Levin, R.L., 1989, "Temperature mapping with MR imaging of molecular diffusion: application to hyperthermia", *Radiology*, 171, pp. 853-857.

LeCarpentier, G.L., Motamedi, M., McMath, L.P., Rastegar, S. and Welch, A.J., 1993, "Continuous wave laser ablation of tissue: Analysis of thermal and mechanical events," *IEEE Trans. Biomed Eng.*, 40, pp. 188-200.

LeCarpentier, G.L., Motamedi, M., McMath, L.P., Rastegar, S. and Welch, A.J., 1989, "The effect of wavelength on ablation mechanism during cw laser irradiation: argon verses Nd:YAG (1.32 μm)", *Proc. IEEE Eng. in Medicine and Biology Society*, pp. 1209-1210.

Liauh, C-T, Clegg, S.T. and Roemer, R.B., 1991, "Estimating three-dimensional temperature fields during hyperthermia: Studies of the optimal regularization parameter and time sampling period," *J. Biomech. Eng.*, **113**, pp. 230-238.

Liauh, C-T and Roemer, R.B., 1993, "Multiple minima in inverse hyperthermia temperature estimation problems", *J. Biomech. Eng.*, **115**, pp. 239-246.

Liauh, C-T, Hills, R.G. and Roemer, R.B., 1993, "Comparison of the adjoint and influence coefficient methods for solving the inverse hyperthermia problem", *J. Biomech. Eng.*, **115**, pp. 63-71.

Linke, C., Elbadawi, A., Netto, V., Roberts, A. and Russo, M., 1972, "Effect of marked hyperthermia upon canine bladder", *J. Urology 4*, **117**, pp. 599-602.

Lofberg, A.M., Arvidsson, D., Andersson, T., Lindgren, P.G., Lorelius, L.E. and Nordlinder, H., 1994, "Ultrasound monitored laser-induced local hyperthermia in the liver", *Acta Radiologica*, **35**, pp. 6-9.

McKenzie, A.L., 1986, "A three-zone model of soft-tissue damage by a CO_2 laser", *Phys. Med. Biol.*, **31**, pp. 967-983.

McKenzie, A.L., 1990, "Physics of thermal processes in Laser-tissue interaction", *Phys. Med. Biol.*, **35**, pp. 1175-1209.

Malone, D.E., Lesiuk, L., Brady, A.P., Wyman, D.R. and Wilson, B.C., 1994a, "Hepatic interstitial laser photocoagulation: demonstration and possible clinical importance of intravascular gas", *Radiology*, **193**, pp. 233-237.

Malone, D.E., Wyman, D.R., DeNardi, F.G., McGrath, F.P., De Gara, C.J. and Wilson, B.C., 1994b," Hepatic interstitial laser photocoagulation, an investigation of the relationship between acute thermal lesions and their sonographic images", *Invest. Radiology*, **29**, pp. 915-921.

Marchesini, R., Pignoli, E., Tomatis, S., Fumagalli, S., Sichirollo, A.E., Di Palma, S., Dal Fante, M., Spinelli, P., Croce, A.C. and Bottiroli, G., 1994, "Ex vivo optical properties of human colon tissue," *Lasers Surg. Med.*, **15**, pp. 351-357.

Matsumoto, R., Selig, A.M., Colucci, V.M. and Jolesz, F.A., 1992, "Interstitial Nd:YAG laser ablation in normal rabbit liver: Trial to maximize the size of laser-induced lesions," *Lasers Surg. Med.*, **12**, pp. 650-658.

Matthewson, K., Colerridge-Smith, P., O'Sullivan, J.P., Northfield, T.C. and Bown, S.G., 1987, "Biological effects of intrahepatic neodymium: Yttrium-aluminum-garnet laser photocoagulation in rats," *Gastroenterology*, **93**, pp. 550-557.

Mihashi, S., Jako, G., Ireze, J., Strong, M.S. and Vaughan C.W., 1976, "Laser surgery in otolaryngology: interaction of CO_2 laser and soft tissue", *Ann. N.Y. Acad. Sci.*, 267, pp. 263-295.

Nolsoe, C.P., Torp-Pedersen, S., Burcharth, F., Horn, T., Pedersen, S., Christensen, N.E.H., Olldag, E.S., Andersen, P.H., Karstrup, S., Lorentzen, T. and Holm, H.H., 1993, "Interstitial hyperthermia of colorectal liver metastases with a US-guided Nd-YAG laser with a diffuser tip: A pilot clinical study," *Radiology*, 187, pp. 333-337.

Ohyama, M., Nobori, T., Moriyama, I., Furuta, S. and Shima, T., 1988, "Laserthermia on head and neck malignancies: Experimental and clinical studies," *Acta Otolaryngol Suppl.*, 458, pp. 7-12.

Ouyang, T., 1992, "Analysis of parameter estimation heat conduction problems with phase change using finite element method," *Int. J. for Numerical Methods in Eng.*, 33, pp. 2015-2037.

Overgaard, J. and Suit, H.D., 1979, "Time-temperature relationship in hyperthermia treatment of malignant and normal tissue *in vivo*", *Cancer Res.*, 39, pp. 3248-3253.

Parker, D.L., 1984, "Applications of NMR imaging in hyperthermia: an evaluation of the potential for localized tissue heating and noninvasive temperature monitoring", *IEEE Trans. Biomed. Eng.*, 31, pp. 161-167.

Parrish, J.A., Anderson, R.R., Harrist, T., Paul, B. and Murphy, G.P., 1983, "Selective thermal effects with pulsed irradiation from lasers: from organ to organelle", *J. Invest. Dermatol.*, 80, pp. 75s-80s.

Paulsen, K.D. and Jiang, H., 1995, "Spatially varying optical property reconstruction using a finite element diffusion equation approximation", *Med. Phys.*, 22, pp. 691-701.

Pennes, H.H., 1948, "Analysis of tissue and arterial blood temperatures in the resting forearm," *J. Appl. Physiol.*, 1, pp. 93-122.

Pickering, J.W., Posthumus, P. and van Gemert, M.J.C., 1994, "Continuous measurement of the heat-induced changes in the optical properties (at 1064 nm) of rat liver", *Lasers Surg. Med.*, 15, pp. 200-205.

Poepping, T., 1996, private comm.

Pogue, B.W., Patterson, M.S., Jiang, H. and Paulsen, K.D., 1995, "Initial assessment of a simple system for frequency domain diffuse optical imaging", *Phys. Med. Biol.*, **40**, pp. 1709-1729.

Prapavat, V., Roggan, A., Walter, J., Beuthan, J., Klingbeil, U. and Muller, G., 1996, "In vitro studies and computer simulations to assess the use of a diode laser (850 nm) for laser-induced thermotherapy (LITT)," *Lasers Surg. Med.*, **18**, pp. 22-33.

Rastegar, S. Kim, B.M. and Jacques, S.L., 1992, "Role of temperature dependence of optical properties in laser irradiation of biological tissue", *SPIE Laser Tissue Interaction III*, **1646**, pp. 228-235.

Roux, F.X., Merienne, L., Leriche, B., Lucerna, S., Turak, B., Devaux, B. and Chodkiewicz, J.P., 1992, "Laser interstitial thermotherapy in stereotactical neurosurgery," *Lasers Med. Sci.*, **7**, pp. 121-126.

Samulski, T., Lyons, B. and Britt, R., 1985, "Temperature measurements in high thermal gradients: II. Analysis of conduction effects," *Int. J. Rad. Oncol. Biol. Phys.*, **11**, pp. 963-971.

Sapareto, S.A. and Dewey, W.C., 1984, "Thermal dose determination in cancer therapy", *Int. J. Rad. Oncol. Biol. Phys.*, **10**, pp. 787-800.

Song, J., Xu, L.W. and Lemons, D.E., 1995,"Experimental studies on the enhancement in the effective thermal conductivity due to blood perfusion," *ASME Advances in Heat and Mass Transfer in Biotechnology*, HTD **322**, pp. 93-97.

Spells, K.E., 1960, "The thermal conductivities of some biological fluids", *Medical Biology*, **5**, pp. 139-153.

Splinter, R., Svenson, R.H., Littmann, L., Tuntelder, J.R., Chuang, C.H., Tatsis, G.P. and Thompson, M., 1991, "Optical properties of normal, diseased and laser photocoagulated myocardium at the Nd:YAG wavelength", *Lasers Surg. Med.*, **11**, pp. 117-124.

Steger, A.C., Bown S.G. and Clark, C.G., 1988, " Interstitial laser hyperthermia-studies in normal liver", *Br. J. Surg.*, **75**, p. 598.

Steger, A.C., Lees, W.R., Walmsley, K. and Bown, S.G., 1989, "Interstitial laser hyperthermia: a new approach to local destruction of tumours", *Br. Med. J.*, **299**, pp. 362-365.

Steger, A.C., Lees, W.R.L., Shorvon P., Walmsley, K. and Bown, S.G., 1992, "Multiple-fibre low-power interstitial laser hyperthermia: studies in the normal liver", *Br. J. Surg.*, **79**, pp. 139-145.

Stroud, A.H. and Secrest, D.H., 1963, Gaussian Quadrature Formulae, Prentice-Hall, Englewood Cliffs, New Jersy.

Svaasand, L.O., Boerslid, T. and Oeveraasen, M., 1985, " Thermal and optical properties of living tissue: Application to laser-induced hyperthermia", *Lasers Surg. Med.*, **5**, pp. 589-602.

Svaasand, L.O., 1989, "Dosimetry for laser induced hyperthermia," *Lasers Med. Sci.*, **4**, pp. 309-315.

Thomsen, S., 1991, "Pathologic analysis of photothermal and photomechanical effects of laser-tissue interactions," *Photochem. and Photobiol.*, **53**, pp. 825-835.

Tikhonov, A.N., 1963, "Solution of incorrectly formulated problems and the regularization method", *Soviet Mathematics Doklady*, **4**, pp. 1035-1038.

Tracz, R.A., Wyman, D.R., Little, P.B., Towner, R.A., Stewart, W.A., Schatz, S.W., Pennock, P.W. and Wilson, B.C., 1992, "Magnetic resonance imaging of interstitial laser photocoagulation in brain," *Lasers Surg. Med.*, **12**, pp. 165-173.

van Hillegersberg, R., van Staveren, H.J., Kort, W.J., Zondervan, P.E. and Terpstra, O.T., 1994, "Interstitial Nd:YAG laser coagulation with a cylindrical diffusing fiber tip in experimental liver metastases", *Lasers Surg. Med.*, **14**, pp. 124-138.

Vyas, R. and Rustgi, M.L., 1992, "Green's function solution to the tissue bioheat transfer equation", *Med. Phys.*, **19**, pp. 1319-1324.

Wei, D., Saidel, G.M. and Jones, S.C, 1995," Estimation of cerebral blood flow from thermal measurement", *J. Biomech. Eng.*, **117**, pp. 74-85.

Weinbaum, S. and Jiji, L.M., 1985, "A new simplified bioheat equation for the effect of blood flow on local average tissue temperature", *J. Biomech. Eng.*, **107**, pp. 131-139.

Weinberg, A. and Wigner, E., 1958, The Physical Theory of Neutron Chain Reactors, Chicago: U. of Chicago Press.

Welch, A.J., 1984, "The thermal response of laser irradiated tissue", *IEEE J. Quantum Electron.*, **QE-20**, pp. 1471-1481.

Whelan, W.M., Wyman, D.R. and Wilson, B.C., 1995, "Investigations of large vessel cooling during interstitial laser heating", *Med. Phys.*, **22**, pp. 105-115.

Wilson, J., 1991, "Tissue optical properties in relation to photocoagulation", *Lasers Surg. Med. Suppl.*, **3**.

Wulff, W., 1974, "The energy conservation equation for living tissue", *IEEE Trans. Biomed. Eng.*, **21**, p. 494.

Wyman, D.R., Patterson, M.S. and Wilson, B.C., 1989, "Similarity relations for the interaction parameters in radiation transport", *Applied Optics*, **28**, pp. 5243-5249.

Wyman, D.R., Swift, C.L., Siwek, R.A. and Wilson, B.C., 1991, "A control method for a nonlinear multivariable system: Application to interstitial laser hyperthermia," *IEEE Trans. Biomed. Eng.* , **38**, pp. 891-898.

Wyman, D.R., Whelan, W.M. and Wilson, B.C., 1992, "Interstitial laser photocoagulation: Nd:YAG 1064 nm optical source compared to point heat source," *Lasers Surg. Med.*, **12**, pp. 659-664, 1992.

Wyman, D.R., 1993, "Selecting source locations in multifiber interstitial laser photocoagulation", *Lasers Surg. Med.*, **13**, pp. 656-663.

Wyman, D.R. and Whelan, W.M., 1994, "Basic optothermal diffusion theory for interstitial laser photocoagulation", *Med. Phys.*, **21**, pp. 1651-1656.

Wyman, D., Wilson, B. and Adams, K., 1994, "Dependence of laser photocoagulation on interstitial delivery parameters," *Lasers Surg. Med.*, **14**, pp. 59-64.

Xu, L.X., Chen, M.M., Holmes, K.R. and Arkin, H., 1991, "The evaluation of the Pennes, The Chen-Holmes, The Weinbaum-Jiji bioheat transfer models in pig kidney cortex", *ASME WAM*, **HTD 189**, pp. 15-21.

Yuan, D.Y., Valvano, J.W., Rudie, E.N. and Xu, L.X., 1995, "2-D finite difference modeling of microwave heating in the prostate," *ASME Advances in Heat and Mass Transfer in Biotechnology*, **HTD 322**, pp. 107-116.

Zienkiewicz, O.C. and Taylor, R.L., 1987, The Finite Element Method. 4_{th} ed. McGraw-Hill: London.

Zhu, L., Lemons, D.E. and Weinbaum, S., 1995, "A new approach for predicting the enhancement in the effective conductivity of perfused tissue due to hyperthermia," *Ann. Biomed. Eng.*, **23**, pp. 1-12.

Zhu, L. and Weinbaum, S., 1995, "A model for heat transfer from embedded blood vessels in two-dimensional tissue preparations", *J. Biomech. Eng.*, **117**, pp. 64-73.